POLITECNICO
MILANO 1863

SCUOLA DI INGEGNERIA INDUSTRIALE
E DELL'INFORMAZIONE

Analytical and numerical modeling of creep with damage in a solder alloy

Tesi di Laurea Magistrale in
Mechanical Engineering - Ingegneria Meccanica

Author: **Luca Renzi**

Student ID: 223673
Advisor: Prof. Mauro Filippini
Co-advisors: Prof. Wolfgang H. Müller, Dr. Aleksandr Morozov
Academic Year: 2023-24

Abstract

This work is dedicated to the investigation of the creep behavior of SAC305 solder balls under cyclic shear stress loading, with a focus on the evolution of the hysteresis loop and the damage parameter. An elastic-creep model is implemented, fitting experimental data regarding the secondary creep strain rate with several optimization algorithm, creep material parameters for the NORTON and hyperbolic-sine creep laws are identified by residual minimization. Statistical distribution of the optimized parameters is represented with use of boxplots, parameter's median is evaluated as possible choice to fit secondary creep strain rate data. The optimum parameter set is identified and evolution of creep relevant quantities numerically simulated over cycling; results from Python code and Abaqus with used-defined FORTRAN subroutines are compared. A nonlinear isotropic hardening model is implemented to capture the primary creep stage based on the experimentally obtained hysteresis curve. Creep law material parameters are identified to fit this model and results compared with ones obtained from secondary creep strain rate fit. A finite element model of a solder ball subjected to cyclic shear loading is created using a submodeling approach to accurately capture most stressed regions in the solder joints. The results identify the most stressed regions within the solder ball and track the evolution of damage and hysteresis loop over cycles, evidencing in which phases of the cycle the damage accumulates.

Keywords: creep, damage, SAC305, hysteresis, viscoplastic, numerical simulation

Abstract in lingua italiana

Questo lavoro ha come obbiettivo lo studio del comportamento a creep delle saldature in SAC305 tipiche dei circuiti stampati e sottoposte a carichi di taglio ciclici. Il primo modello di studio è uno di tipo elastico-creep. I parametri delle leggi del creep sono stati identificati a partire dai dati sperimentali relativi alla velocità di deformazione viscosa secondaria utilizzando diversi algoritmi di ottimizzazione. I parametri del materiale per le leggi di creep di Norton e della funzione iperbolica del seno sono stati identificati tramite minimizzazione dei residui. La distribuzione statistica dei parametri ottimizzati è rappresentata tramite boxplot. Le mediane dei parametri sono valutate come possibili scelte per predire i dati sperimentali relativi alla velocità di deformazione del creep secondario. L'insieme dei parametri ottimali è identificato e l'evoluzione di quantità rilevanti per il comportamento a creep è numericamente simulata nel corso dei cicli. I risultati così ottenuti sono confrontati con quelli ottenuti da simulazioni ad elementi finiti con Abaqus, utilizzando delle user-defined subroutines in FORTRAN. Un modello di incrudimento isotropo non lineare è implementato per catturare la fase di deformazione plastica basandosi sulla curva di isteresi ottenuta sperimentalmente. I parametri del materiale per le leggi di creep sono iindividuati per adattarsi a questo modello e i risultati sono confrontati con quelli ottenuti calibrando i parametri rispetto ai dati di velocità di deformazione del creep secondario. Un modello ad elementi finiti di un giunto di saldatura sottoposta a carichi di taglio ciclici è creato utilizzando l' approccio del submodeling per catturare le regioni più sollecitate nei giunti di saldatura. I risultati identificano le regioni più sollecitate all'interno della sfera di saldatura e tracciano l'evoluzione del danno e del ciclo di isteresi durante i cicli, evidenziando in quali fasi del ciclo si accumula il danno.

Parole chiave: creep, danno, SAC305, isteresi, viscoplastico, simulazione numerica

Contents

Abstract **i**

Abstract in lingua italiana **iii**

Contents **v**

Introduction **1**

1 The creep problem **5**
1.1 Introduction to creep . . . 5
1.2 Physical mechanisms in creep . . . 10
1.2.1 Time-temperature parameters for life estimate . . . 13
1.2.2 Creep cavitation for metals . . . 14
1.2.3 Cavity nucleation . . . 16
1.2.4 Cavity growth . . . 18
1.3 Creep modeling . . . 19
1.3.1 Constitutive models for creep . . . 21
1.4 Creep damage mechanics . . . 26
1.4.1 Historical perspective . . . 26
1.4.2 Scalar damage parameter . . . 27
1.4.3 Energy related formulation of the scalar damage parameter . . . 31
1.4.4 Damage vector . . . 32
1.4.5 Damage tensor . . . 32

2 Experimental data processing **35**
2.1 Experimental procedure . . . 35
2.2 SAC305 material properties . . . 39
2.3 Material parameters identification . . . 41
2.3.1 Available data . . . 41

2.3.2 Isothermal formulation of creep laws 41
2.3.3 Optimization procedure 44
2.3.4 Statistical dispersion of optimized data 54
2.4 Evolution of creep and damage under cycling loading 58
2.4.1 Numerical evolution of ODE without damage 59
2.4.2 Numerical evolution of a system of ODEs with damage 60
2.4.3 Selection of material creep parameters 64
2.5 Verification of numerical results using finite element software 71

3 Time-independent plasticity **75**
3.1 Flow and hardening laws for nonlinear plasticity 75
3.2 Plasticity model implementation in Python 76

4 Solder ball cyclic shear loading **81**
4.1 Ball grid array structure 81
4.2 Thermal modeling of temperature cycling effects on solder balls 83
4.3 Finite element simulation of temperature shock test 84
4.3.1 Global model 85
4.3.2 Submodeling 88
4.3.3 Solder ball cyclic behavior 90

5 Conclusion and discussion **97**

Bibliography **101**

Appendix A **111**

List of Figures **115**

List of Tables **119**

Listings **121**

List of Symbols **124**

Acknowledgements **125**

Introduction

Creep can be defined as the plastic time-dependent or viscoplastic behavior of a material, characterized by irreversible plastic deformation that occurs independently of the applied stress level. It is a thermally activated phenomenon, occurring only above a certain critical temperature and even below the material's yield point.

Creep-related phenomena must be considered in contexts where components experience significant temperature variations and sustained loading above their critical temperature. Common examples include applications in nuclear power plants [40, 60] and turbine engines [70, 77]. In these cases, the material deforms progressively until rupture occurs. Creep-induced failures can also be observed in everyday life, such as the breakage of light-bulb filaments, the failure of plastic pipes under slow deformation [18], tragic events like the collapse of the World Trade Center [10], or even in natural phenomena such as glacier sliding [20].

The objective of this work is to investigate the creep behavior of solder balls under cyclic shear loading. The studied material is SAC305, its chemical composition reads 96.5Sn–3.0Ag–0.5Cu. This type of solder is becoming in the last years more common in the industry as consequence of the ban applied on lead-containing solders. SAC305 is non-eutectic alloy with a lower melting temperature of 217°C and exhibits creep deformation even at room temperature. Solder balls are soldered deposits used in the microchip industry to create mechanical and electrical connections between the microchip frame and the printed circuit board. During their operative life solder joints are subjected to temperature fluctuations as consequence of electric current flowing through the circuits, where electrical resistance generates heat (Joule effect). Along with the solder joints, the microchip frame and printed circuit board (PCB) are also subject to temperature fluctuations, leading to thermal expansion and contraction. Variations in the elastic modulus and coefficients of thermal expansion among these materials generate interfacial stresses, particularly at the boundaries between the solder joints and the adjacent components, with the solder acting as the softer material among the three. The differences in the displacement fields induce a repeated stress state within the solder, leading to the nucleation and propagation of cracks through creep-fatigue interactions. Solder joints are required to

guarantee the correct functioning of all microelectronic components and as consequence, strong efforts are made in the direction of improving their reliability.

This issue is further amplified by industry-driven miniaturization efforts, which aim to produce increasingly smaller chips to enhance power density. However, this reduction in size also limits the chip's ability to dissipate heat, making it more vulnerable to temperature-related damage mechanisms such as creep or aging. The SAC305 alloy commonly fails due to in-service coarsening, a key degradation mechanism. According to [105], two primary coarsening processes occur: thermal coarsening and strain-enhanced coarsening. Notably, it is the Ag_3Sn particles that undergo coarsening. These particles form during the eutectic reaction and significantly enhance the solder's properties by providing precipitation strengthening, which improves both strength and creep resistance. An example of coarsening is illustrated in Figure 1.

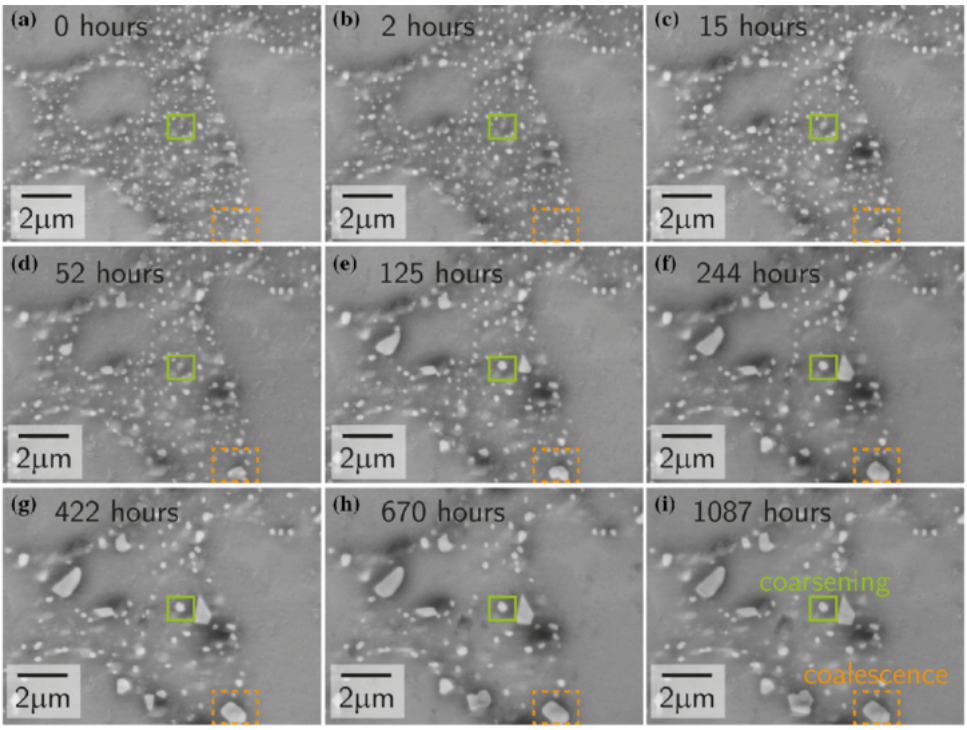

Figure 1: Time-lapse BSE images of a SAC305/Cu joint during aging at 125°C. (a) is the as-solidified microstructure. Aging times are indicated in (b–i). Boxes show particles undergoing coarsening (green) and coalescence (orange) [105]

The microstructural evolution of SAC305 under test conditions is well documented, with tests conducted at 125°C over a maximum duration of 1087 hours. Within the eutectic regions, the component Cu_6Sn_5 is identified. As exposure time increases, particles of Ag_3Sn coarsen and undergo coalescence, remaining within the original eutectic regions.

Green and orange boxes in the figure highlight coarsening and coalescence phenomena, respectively.

Ag_3Sn particles tend to coarsen over the cycles, leading to a reduction in precipitation hardening. These particles, along with intermetallic compounds (IMCs) like $(Cu,Ni)_6Sn_5$, promote crack initiation at the joint neck after only a few hundred cycles [88]. This coarsening effect, combined with the microstructural changes from recrystallization, contributes to the mechanical degradation of the solder joint under cyclic thermal loading.

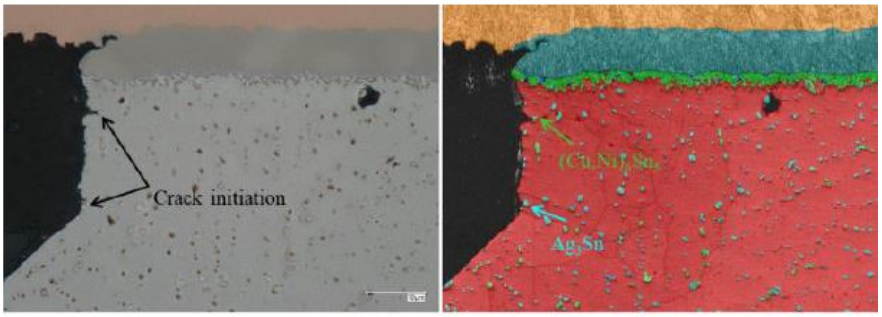

Figure 2: Crack initiation site at 360 cycles [88]

In Figure 2, the crack initiation process is illustrated at 360 cycles. The crack starts at the solder neck, specifically in regions where intermetallic compounds (IMCs) are more pronounced. These areas provide low resistance to dislocation movement, creating favorable sites for crack nucleation. The presence of larger IMCs weakens the microstructure, accelerating crack initiation under cyclic loading conditions. As shown above, the regions of the solder joints closer to the solder-microchip and solder-PCB are the ones where the stress concentration is stronger and the crack nucleate.

In this work, the material is modeled as isotropic, assuming that the solder joints are large enough and contain a sufficient number of grains for the component's overall properties to be considered isotropic and homogeneous. However, for smaller solder joints, this approach may no longer be valid, as a limited number of grains can cause the component to respond anisotropically to external stress. In such cases, crystal plasticity models are required, as demonstrated in [45].

The degradation of solder material as a result of thermomechanical cycling leads to a gradual decline in the mechanical properties like elastic modulus, yield strength, and ultimate tensile strength [42]. According to the model firstly introduce by Kachanov [48] and expanded by Rabotnov [85], the degradation of mechanical properties can be modeled with the introduction of the scalar damage parameter. Damage manifest itself in

the form of microcracks or voids, these can be observed in the area between sleep bands with the use of SEM (scanning electron microscopy) analysis. Further studies regarding the deterioration of mechanical properties as consequence of the mechanical cycling are [42] and [38].

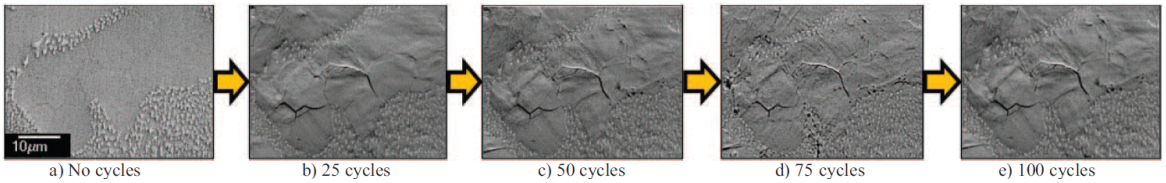

Figure 3: Evolution of SAC305 Microstructure with mechanical cycling at T = 25 °C [42]

The pristine microstructure on the left of Figure 3 is formed by β-Sn dendrites (white dots) and eutectic regions. After 25 cycles the effects of plastic strain are visible, as microcracks form at sub-grain boundaries and tend to elongate over the cycles.

Several empirical model, that describe the dependence of the creep strain rate on temperature and stress, are available; in this work, building on data acquired in [62], material parameters for the NORTON and hyperbolic-sine creep laws are fitted to the secondary creep strain rate within an elastic-creep model. More complex models like the ANAND one can be fitted but normally require a large dataset for different levels of temperature and stress [68]. Approaches like COFFIN-MANSON relationship or the MORROW equations are commonly used to predict the fatigue life, however fail to account for the change in the mechanical properties [16]. In this work, a model based on total dissipated energy energy is proposed.

Fitting creep constitutive laws to secondary creep strain rate experimental data reveals the high nonlinearity of the problem. Moreover, material microstructure and test conditions have a large impact on the experimental results and consequently on the results of the optimization technique. In this work the material properties are identified starting from results on 1D specimens, however properties of the bulk material is solder are usually quite different [26] in the obtained data. Obtained results are valid only if considering relatively large solder joints. The feasibility of using a nonlinear isotropic hardening law to fit primary creep datapoints with an elastic-plastic-creep model is also explored. Following an approach similar to [26], a finite element (FE) model of a solder ball is reproduced and tested under cyclic shear stress conditions. However, in this work, a submodeling approach is used to more accurately simulate real displacement fields within the entire assembly.

1 | The creep problem

In this first chapter, microscopic phenomena related to creep as well as basic concepts of creep modeling equations are presented.

1.1. Introduction to creep

Creep can be defined as a progressive, time-dependent inelastic deformation of a material that occurs under constant load. When a constant displacement is imposed, the material undergoes stress relaxation, a condition characterized by a decrease in stress while maintaining fixed strain. Under creep conditions, the material exhibits viscoplastic behavior, meaning that despite being solid, it flows and deforms over time, contrasting with the predictions of elastic-plastic theory. In this work, the term "inelastic" is used as a general term to describe creep-related and plastic time-independent deformations, while time-independent deformations are addressed with the word "plastic". Like plastic deformations, creep deformations are irreversible and are not recovered upon load removal. However, creep-related deformations can occur within the elastic range of the material and do not depend on its yield point.

The complexity of creep behavior, as discussed in [18], is further amplified by the potential influence of environmental factors (such as oxidation) and the interaction between cyclic loading and time-dependent deformation. This interaction results in a creep-fatigue mechanism that fosters the fatigue process, thereby reducing the residual life of the material. However, as noted in [96], the frequency of stress variation has a minimal impact on creep behavior under high-frequency cyclic loading. Creep is a thermally activated mechanism, occurring only within specific temperature ranges. According to [63], various types of creep can be distinguished for metals, depending on the temperature conditions.

1. **Logarithmic creep**: $0 < T < 0.3T_{\text{melting}}$,
   the strains stabilize after the initial elastic response, no time-dependent behavior.

2. **Main creep range**: $0.3T_{\text{melting}} < T < 0.9T_{\text{melting}}$,
   thermal energy can initiate difficult dislocation processes, here the deformation de-

pends on the application time.

3. **Diffusion creep**: $0.9T_{\text{melting}} < T < T_{\text{melting}}$,
   here diffusion mechanisms are prevalent, recalling the liquid flow.

Of the three types of creep, the second is the most relevant and will henceforth be referred to simply as "creep". The temperature ranges associated with creep are typically expressed in terms of the homologous temperature, T_{hom} , as defined in [89] and shown in Equation 1.1,

$$T_{\text{hom}} = \frac{T[K]}{T_m[K]}, \tag{1.1}$$

where, T is the operating temperature in Kelvin and T_m is the melting temperature of the material in Kelvin.

The considered range is usually $0.3 < T_{\text{hom}} < 0.7$, however the range varies depending on the material. In the case of tin solder balls values up to 0.85 T_{hom} can be reached [61]. The creep problem is upper bounded with respect to the temperature for a number of reasons:

1. Over a certain temperature the material in unable to keep its structural integrity, progressive deformation is no longer possible.
2. Beyond a certain temperature the creep rate increases too quickly going directly to the tertiary stage.
3. Damage also occurs more rapidly at very high temperatures, rendering the material unstable and difficult to test.

The most common type of test for a mono-dimensional specimen is the *dead load test* represented in Figure 1.1.

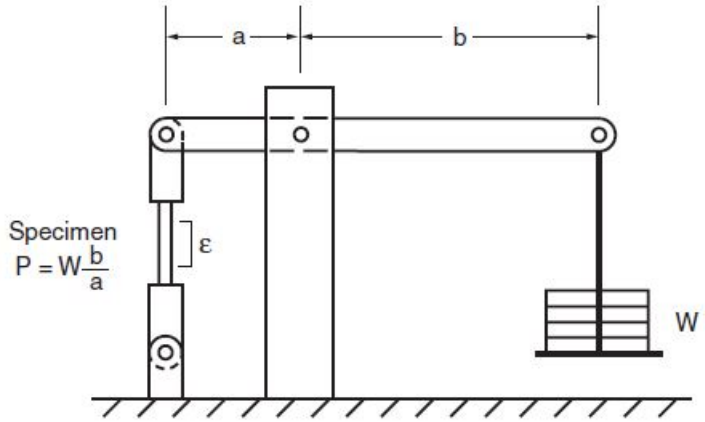

Figure 1.1: Schematic representation of a creep testing machine [18]

Observing Figure 1.1, weights are applied on the right side, and through a leverage system, the load is transferred to the specimen on the left. The test continues until the material breaks.

This type of test is used for identifying material parameters and is conducted at fixed temperature and load. Since it is a destructive test, one specimen is required for each unique combination of load and temperature. For non-isotropic materials, additional tests are necessary, as the number and orientation of loading directions depend on the material's symmetries.

The result of this kind of test is shown in Figure 1.2.

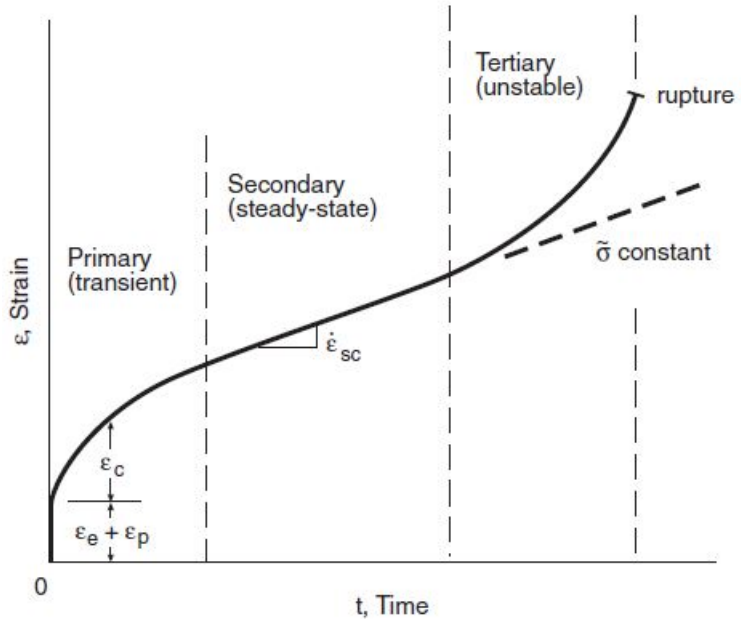

Figure 1.2: Strain versus time behavior during creep under constant load and the three stages of creep [18]

Starting from the left side the initial and nearly instantaneous elastic (ε_e) and eventually plastic strain (ε_p) can be identified. After the initial transitory response the creep or inelastic strain (ε_c) becomes predominant. Being creep a time-dependent phenomena the graph can be divided in three parts. The tangent line to the graph represents the strain rate $\dot{\varepsilon} = d\varepsilon/dt$, which represents the rapidity of change of the strain over time. The $\widetilde{\sigma}$ represents the true or effective stress in the specimen associated with the lowest value of the creep strain rate. The symbol $\dot{\varepsilon_{sc}}$ represents the steady-state creep rate.

According to [4], the time-dependent creep response can be divided into three parts:

- Primary (transient) creep: The creep rate decreases over time until it reaches its minimum value.
- Secondary (steady-state) creep: Area of approximately constant and minimum value of the creep rate.
- Tertiary (unstable) creep: The strain rate rapidly increases, deformation becomes evident and localized, necking takes place and voids are generated in the material.

The third and final stage of creep progresses until the specimen ruptures. It is important to note that Figure 1.2 is not in scale; in reality, the secondary creep phase is significantly larger than the other stages, making it the most critical phase for engineering applications. Consequently, much of the analysis should focus on developing a robust model to

accurately predict the duration of this phase, as it is crucial for estimating the material's overall lifespan. By the end of the secondary creep stage, the deformation caused by creep is expected to exceed that from both the material's elastic and plastic responses.

The length of the creep stages and the shape of the curve depends on temperature and stress [72]. As the temperature or the stress increase, the life of the material shortens as illustrated in Figure 1.3.

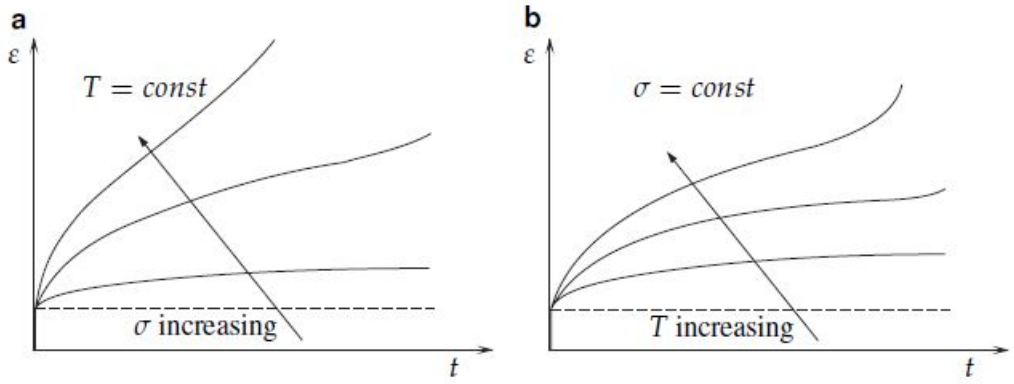

Figure 1.3: Influence of stress and temperature on the creep behavior. **a** Stress dependence, **b** temperature dependence [72]

The increase of temperature and stress has a similar effect, the creep curve is moved to the upper-left corner, the effect of temperature in general stronger. These modifications are correlate to an increase in the of the secondary creep strain rate. Two others type of dependencies of the creep behavior can be highlighted [72]. At constant temperature the dependence on the strain rate is evident in Figure 1.4.

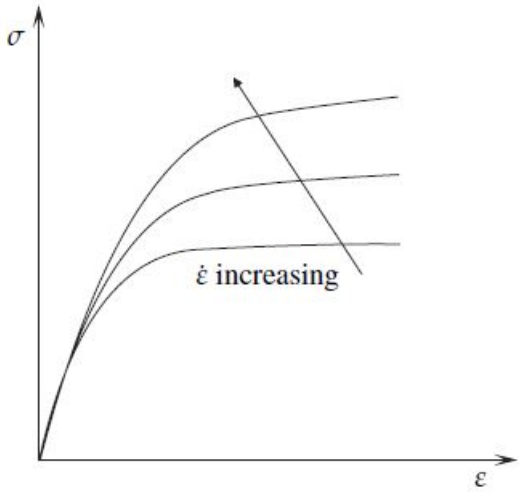

Figure 1.4: Strain rate dependence of the stress-strain behavior [72]

As the deformation gets faster, the ability of the material to withstand higher stresses increases. The results are clearly visible in a stress-strain diagram.

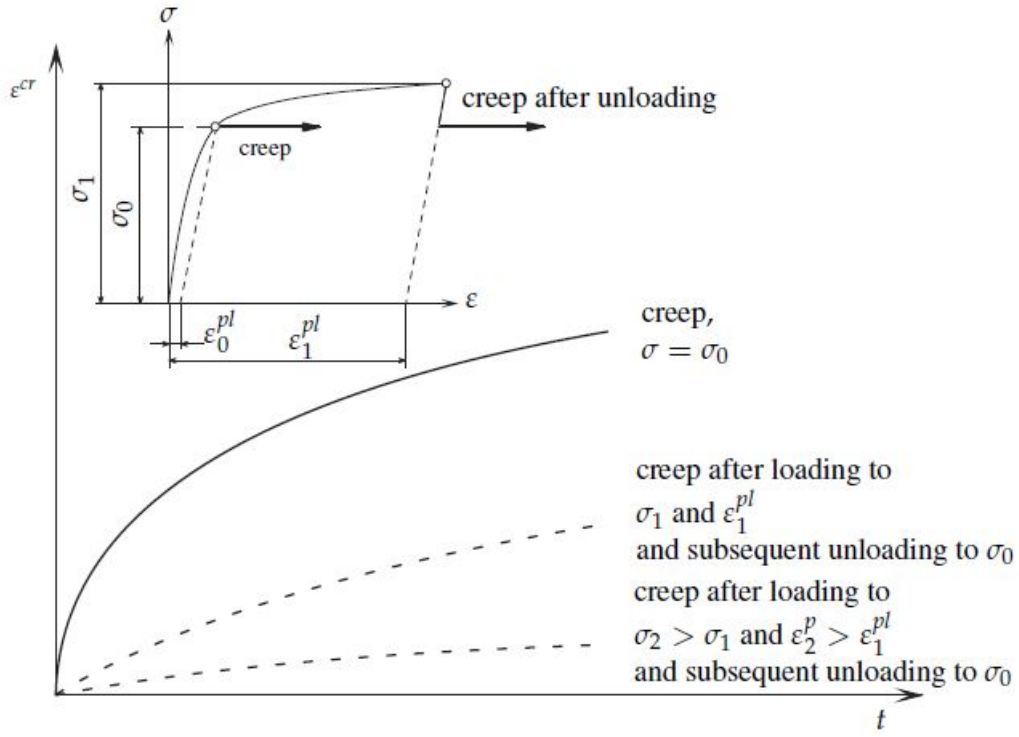

Figure 1.5: Effect of initial plastic strain on creep behavior [72], for details [54]

In Figure 1.3, the dependence of the creep phenomenon to material processing is illustrated. The solid line shows the primary creep curve and the beginning of the secondary creep under constant stress, σ_0. The two dashed lines represent the creep behavior following loading at stresses σ_1 and σ_2, which induce respective plastic strains, followed by immediate unloading back to the stress σ_0. After this plastic deformation, the creep rate decreases significantly compared to the pristine material, with a stronger reduction as the plastic strain becomes more substantial. This phenomenon is commonly referred to as "plasticity-creep" or "creep-plasticity" interaction [72].

1.2. Physical mechanisms in creep

Diffusion is a physical mechanism that takes place during creep deformation at high temperatures, it is usually associated with motion of atoms, dislocations, vacancies or molecules inside a solid material and with a time-dependent behavior [18]. Under creep conditions, especially at high temperatures, metals behave like liquids with a very high viscosity, this formula from fluid mechanics can be applied:

$$\eta_\tau = \frac{\tau}{\dot{\gamma}} \tag{1.2}$$

where, η_τ is the shear viscosity, τ the applied shear stress and $\dot{\gamma}$ the shear strain rate.

In the same way the tensile viscosity η can be defined as:

$$\eta = \frac{\sigma}{\dot{\varepsilon}}. \tag{1.3}$$

Where σ represents the normal stress and $\dot{\varepsilon}$ the normal strain rate.

The diffusion related mechanisms are related to the temperature, the increase in temperature leads to an increase of the kinetic energy of atoms in the lattice and then to larger oscillations around the equilibrium position [18]. The conclusion is that thermal activation is necessary for creep time-dependent deformation, the strain rate of a thermally activated process is regulated by an equation such as Equation 1.28.

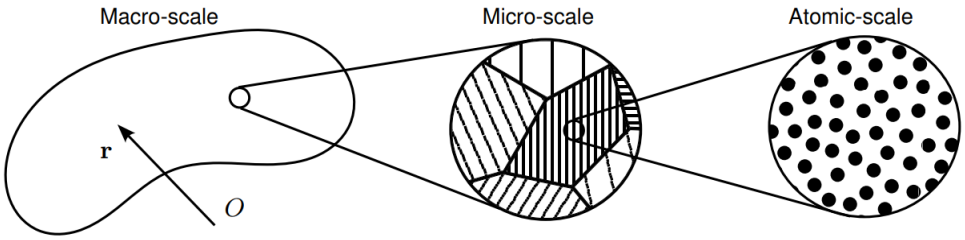

Figure 1.6: Three different levels of observation of the material [67]

In Figure 1.6 three possible levels of material observation are represented; at the atomic-scale diffusion of single atoms or vacancies take place, in the micro-scale interactions between grains are dominant and in the macro-scale material is considered as a continuous and homogeneous body.

At temperatures $0.5 < T_{\text{hom}} < 0.7$ and relatively high stresses, dislocation creep also known as power-law creep is dominant. Transport processes like motion of dislocations (line defects) or diffusion of vacancies (point defect) take place. Dislocation climb is particularly relevant in this phase due to the high stresses, representation is given in Figure 1.7. In this figure the crystal structure is represented, normally dislocations move alongside plane (horizontal lines) until an obstacle is encountered (round object).

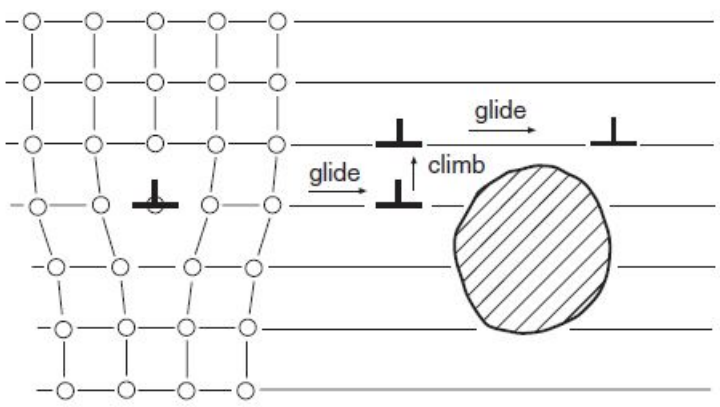

Figure 1.7: Climb of an edge dislocation, allowing continued glide past an obstacle and enabling deformation process [18]

The edge dislocation (overturned T shape) glides in the crystal lattice with a step-wise motion named "glide". Once an obstacle is encountered, a "climb" takes place and the edge dislocation moves vertically to another lattice plane by rearranging the atoms surrounding the defect. The "glide" is possible, due to the high stress and relatively high temperatures.

If temperatures are more elevated ($T_{\text{hom}} > 0.7$) and stress is low, diffusional creep is the dominant mechanism. Diffusion of vacancies takes place as consequence of their spontaneous formation close to grain boundaries oriented normally to the applied stress. As consequence of the non-homogeneous distribution of such defects, these will migrate (diffuse) from regions of higher concentration to regions of lower concentration, deforming the crystal lattice.

Diffusion throughout the matrix (bulk diffusion) is called Nabarro-Herring creep, however if vacancies move along the the grain boundaries as consequence of the action of the deviatoric stress tensor on the chemical potential at the grain boundaries it is named grain boundary diffusion or Coble creep [72].

Another relevant mechanism is the so called grain boundary sliding (GBS), it plays a relevant role in the crack growing process [24]. Cavities will expand predominately in the direction alongside the boundary [51], where grains slide one over each other. This phenomenon is typical for conditions of high temperature and low strain rate, in Figure 1.8 a representation is given. The diagonal line represents the boundary between two grains and the elliptical-shape defect is a newly formed vacancy, as the grains slide one on the other the vacancy is enlarged.

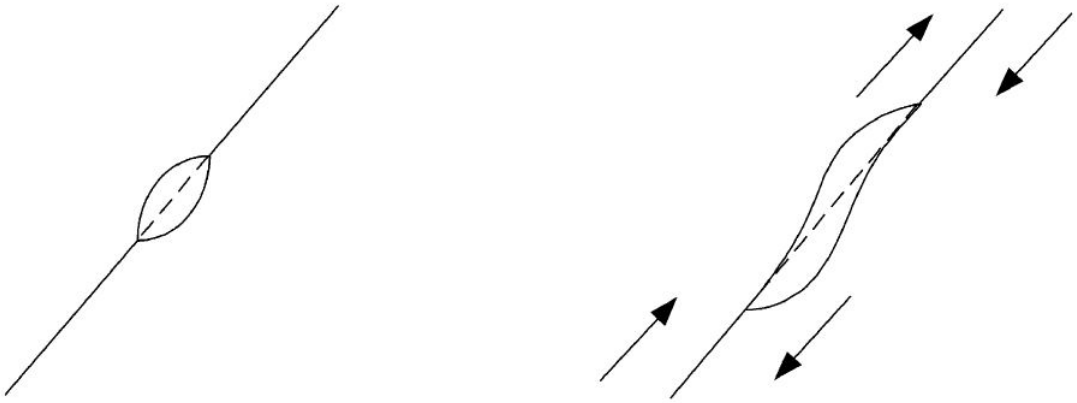

Figure 1.8: Cavity growth as effect of sliding boundaries [14]

1.2.1. Time-temperature parameters for life estimate

The phenomenon of creep is constant across all three stages in the form of cavity nucleation [106], however its effects are not uniform across the three stages represented in Figure 1.2. If nucleation and diffusion are present also in the first two stages, the effects of damage, like the the formation of voids or microcracks, take place only in the last creep stage. This means that in tertiary creep, damage accumulates over time in the form of cracking, crazing and other mechanisms until damage becomes micro- and macroscopically visible and the materials breaks. In the case of crystalline materials like metals, voids tend to form at the grain boundaries or around hard precipitate particles as consequence of localized stress concentration; this process is called creep cavitation. An example is given in Figure 1.9.

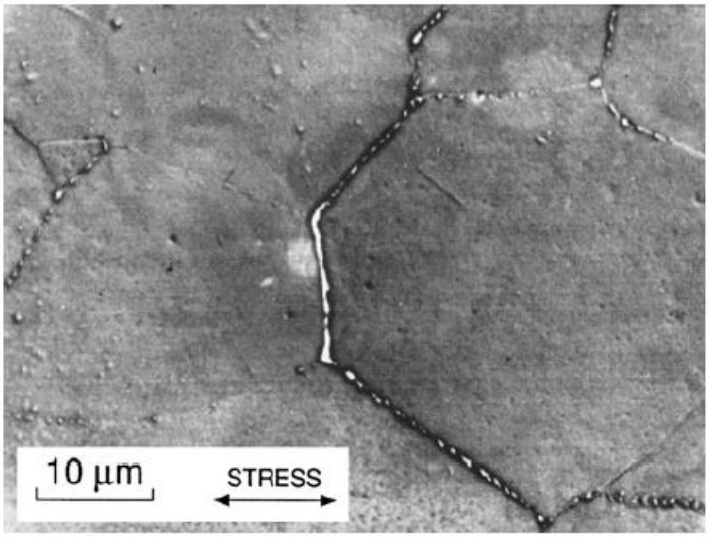

Figure 1.9: Grain boundary cavitation and cracking as consequence of creep in a tantalum alloy (T-111),test carried out in creep–fatigue interaction with temperature variation between 200 and 1150°C, [18]

In Figure 1.9 the edges of the different grains are visible, voids are represented as white dots along the edges. From the illustration above, it is clear how the junction of voids at grain boundaries results in the formation of cracks along the edge; these will expand under cyclic loading until the critical length is reached and creep rupture takes place.

In order to guarantee the correct functioning of an engineering component both excessive deformation and rupture must be avoided over the whole service life. Problems may arise in the testing phase, especially in the case of low strain rates and long times, as it is not feasible to test a component for two decades. One solution could be to extrapolate data from a σ versus $\dot{\varepsilon}$ trend looking for the values of interest at a low strain rate; however this solution does not generates good results.

The best alternative is to use data from tests with a short duration but elevated temperatures. Time-temperature parameters like the Sherby-Dorn parameter or the Larson-Miller parameter are introduced. For further references see [33] and [18].

1.2.2. Creep cavitation for metals

Metals traditionally exhibit little plasticity at ambient temperature for stresses lower than than the yield strength of the material. However at higher temperatures ($T_{\text{hom}} > 0.3$), creep plasticity becomes relevant and results in changes of the metal structure leading to the development of cracks. In [51] is suggested that creep fracture can occur by w-type

or wedge-type cracking at grain boundary triple points as illustrated in the Figure 1.10.

In the following figure the hexagons represent the different grains and the arrows the direction of the stresses at their interfaces. At the junction of three grains (triple point) w-type cracks may form as consequence of grain boundary sliding or accumulation of spherical cavities.

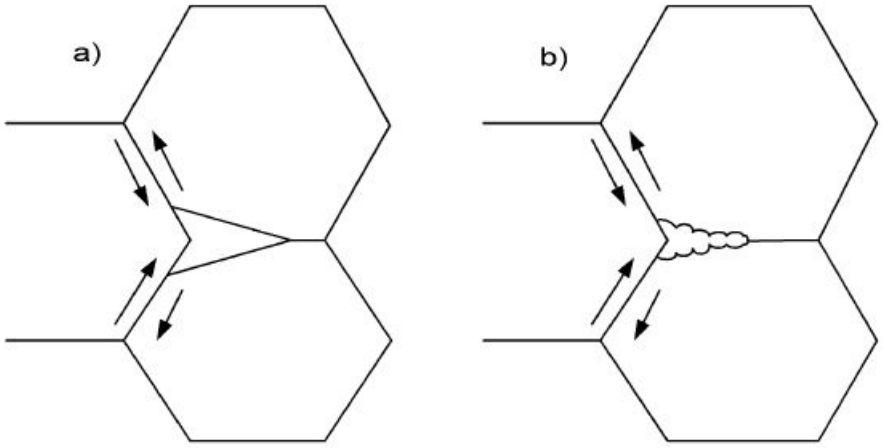

Figure 1.10: (a) Wedge (or w-type) crack formed at the triple junctions as consequence of grain boundary sliding; (b) illustrates a wedge crack as an accumulation of spherical cavities [51]

In [100] is suggested that this type of crack formation should be prevalent in the case of low temperatures and high stresses, when grain boundary sliding is rare to occur. Another type to crack is the r-type, usually associated with cavities or irregularities, a representation is given in Figure 1.11.

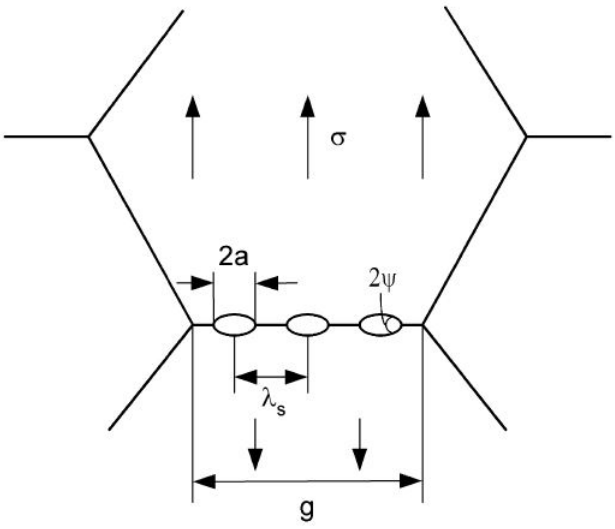

Figure 1.11: Cavitation (r-type) or voids at transverse grain boundary. The angle ψ is assumed around 70° [51]

In [66] the creep fracture for uni-axial tension under constant stress is introduced with the Monkman-Grant relationship according to which the fracture of a material that deforms under creep is controlled by steady state creep according to Equation 1.4,

$$\dot{\varepsilon_{sc}}^{m} t_r = k_1, \tag{1.4}$$

where, k_1 is the so called Monkman-Grant constant, m is a constant in the range between zero and one, $\dot{\varepsilon}_{sc}$ is the steady state creep strain rate and t_r is the time to rupture expressed in seconds.

1.2.3. Cavity nucleation

The mechanism responsible for the nucleation has not yet been determined with absolute certainly, however it is known that cavities tend to nucleate at grain boundaries and normal to the tensile load [15, 43]. As mentioned in subsection 1.2.1, cavities grow in the nearby of second phase particles and as consequence are more common in low purity metals. In [51] four main nucleation theories are presented: grain boundary sliding at the end of a boundary, vacancy condensation at high stress concentration points and cavity formation at the end of a dislocation pile-up like the Zener–Stroh mechanism [103], these mechanisms can involve particles as well. The different mechanisms are represented in Figure 1.12.

In Figure 1.12 the four mechanisms are shown; grains are depicted as hexagons and arrows represent the direction of stresses.

In [86], the theory is developed in which vacancies can coalesce into stable voids, leading to the formulation of a critical radius a^* and a corresponding free energy ΔG_T^* for critical-sized cavities and their nucleation rate. According to [25], a threshold of effective stress is necessary for the onset of nucleation, where a high applied stress accumulates vacancies and initiates nucleation. Consequently, areas with stress concentrations are more susceptible to cavity nucleation. This tendency also applies to the "decohesion" mechanism of cavity nucleation, which similarly depends on stress concentration. Grain boundaries, in particular, are regions where these processes are most likely to occur.

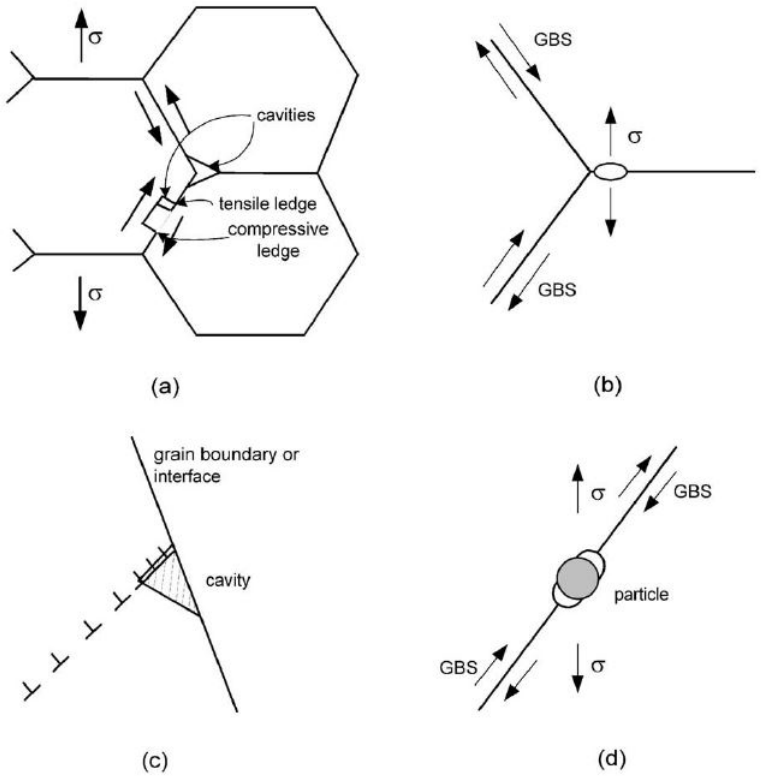

Figure 1.12: Cavity nucleation mechanism: (a) sliding leading to cavitation from ledges (and triple points); (b) cavity nucleation from vacancy condensation at a high stress region; (c) cavity nucleation from a Zener–Stroh mechanism; (d) the formation of a cavity from a particle-obstacle in conjunction with the mechanisms described in (a–c) [51]

The concept of grain boundary sliding (GBS) is introduced concerning the growth of cavities; however, it is also relevant for the nucleation of cavities. GBS tends to create stress concentrations at triple points (the junction of three grains) and around hard particles, resulting in tensile stresses that may lead to cavity nucleation. Additionally, sliding

mechanisms such as GBS promote cavitation along transverse boundaries. It remains uncertain whether sliding is a necessary condition for cavity nucleation [51]; however, [19] demonstrates that GBS significantly facilitates cavitation.

In [97], an alternative nucleation mechanism is analyzed, where vacancies accumulate on hard second-phase particles located at grain boundaries, leading to cavity formation. This phenomenon is known as dislocation pile-up. Furthermore, [21] demonstrates that the nucleation process is continuous throughout all creep stages, with growth and nucleation potentially occurring simultaneously. Given the observed correlation between cavitation rate and ductility, the nucleation process may also be linked to plasticity and plastic deformation, as suggested in [74, 102].

1.2.4. Cavity growth

Cavity growth at elevated temperatures along the grain boundaries is correlated with vacancies diffusion. Diffusion takes place by migration of the cavity surface and transportation along the grain boundaries [51]. At lower temperatures it is related to plasticity [52]. Due to the presence of an applied stress, a stress concentration is generated ahead of the cavity and an initial "negative" stress gradient is created. A depiction of the phenomenon is given in Figure 1.13.

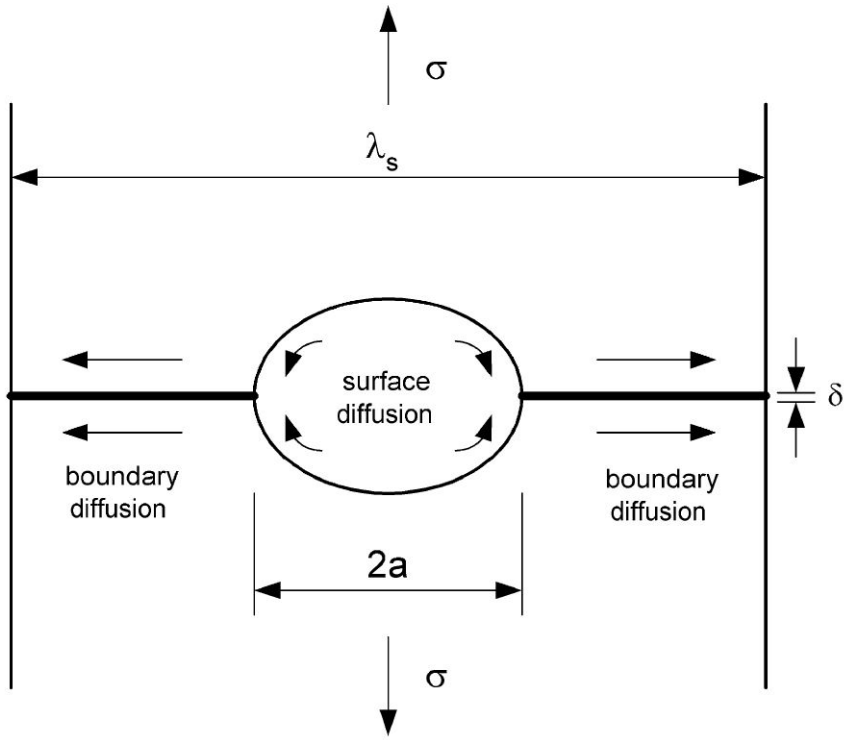

Figure 1.13: Cavity growth from diffusion across the cavity surface and through the grain boundaries as effect of the stress gradient [51]

The primary factor controlling cavity growth is diffusion, with plasticity and grain boundary sliding playing secondary roles. Specifically, surface diffusion, rather than grain-boundary diffusion, governs the cavity growth process [73]. Cavity growth can occur only under plastic conditions, as it results from the creep deformation of material surrounding the grain boundaries. This effect is especially significant under high-strain conditions, where the model proposed in [51] is applicable. As noted in [82], the growth rates of creep cavities are linked to plasticity-driven growth. However, constrained diffusional cavity growth may not always occur, even when associated with plasticity growth [51].

1.3. Creep modeling

When studying the phenomenon of creep, various approaches are available, including material science-based models and micromechanical models. However, this work adopts the continuum mechanics approach, materials are modeled as continuous, rather than discrete, bodies.

The creep behavior is expressed through constitutive equations, without directly considering changes in the material's microstructure. However, processes associated with these

changes, such as damage, aging, or hardening, are represented using state variables and their corresponding evolution equations.

When applying the concepts of continuum mechanics to creep the following assumptions are made, as reported in [72]:

- strains are assumed to be infinitesimal,
- isothermal conditions are assumed, thermal and mechanical problems become independent one from the other, moreover the the heat transfer problem is not considered.

In order to solve the initial-boundary value problem (BVP) the constitutive and balance equations must be considered.

Balance of linear momentum:

$$\rho \frac{\partial \underline{v}}{\partial t} = \boldsymbol{\sigma} \cdot \nabla + \rho \underline{b}, \tag{1.5}$$

where ρ represents the density, $\underline{v}$ the velocity vector, $\boldsymbol{\sigma}$ the CAUCHY stress tensor and $\underline{\mathrm{b}}$ the vector of volume forces. Starting from the left, the first term indicates the inertial momentum, which is usually neglected in quasi-static problems, the second the divergence of the stress tensor and the last one the impact of volume forces.

Kinematic relation (absolute notation):

$$\boldsymbol{\varepsilon} = \frac{1}{2} \left(\nabla \otimes \underline{u} + \underline{u} \otimes \nabla \right), \tag{1.6}$$

where $\underline{u}$ represents the displacement vector and $\boldsymbol{\varepsilon}$ the infinitesimal strain tensor.

Linear strain decomposition:

$$\boldsymbol{\varepsilon} = \boldsymbol{\varepsilon}_{\mathrm{el}} + \boldsymbol{\varepsilon}_{\mathrm{pl}} + \boldsymbol{\varepsilon}_{\mathrm{cr}} + \boldsymbol{\varepsilon}_{\mathrm{th}}, \tag{1.7}$$

where $\boldsymbol{\varepsilon}_{\mathrm{el}}, \boldsymbol{\varepsilon}_{\mathrm{pl}}, \boldsymbol{\varepsilon}_{\mathrm{cr}}$ and $\boldsymbol{\varepsilon}_{\mathrm{th}}$ indicate respectively the elastic, plastic, creep and thermal strain tensors.

The stress tensor is linked to the elastic strain tensor by the constitutive equation:

$$\boldsymbol{\sigma} = \boldsymbol{C} \cdot \cdot \boldsymbol{\varepsilon}_{\mathrm{el}}, \tag{1.8}$$

in which $\boldsymbol{C}$ is a fourth-order tensor representing the stiffness tensor of the material. For an isotropic material, symmetries in stress tensor, strain tensor, and elastic energy accumulation reduce the characterization of its properties to just two material parameters.

The HOOK's law for isotropic materials reads:

$$\boldsymbol{\sigma} = \lambda \operatorname{tr}(\boldsymbol{\varepsilon}_{\mathrm{el}})\,\mathbf{I} + 2\mu\,\boldsymbol{\varepsilon}_{\mathrm{el}}, \tag{1.9}$$

where λ and μ are LAMÈ coefficients and $\mathbf{I}$ is the identity matrix.

In the isotropic case, the thermal expansion of the material can be addressed:

$$\boldsymbol{\varepsilon}_{\mathrm{th}} = \alpha(T - T_{\mathrm{ref}})\mathbf{I}, \tag{1.10}$$

being α the coefficient of thermal expansion (CTE) and T_{ref} the reference temperature at which the strains are zero. Possible constitutive equations for $\boldsymbol{\varepsilon}_{\mathrm{cr}}$ are available in subsection 1.3.1 while a formulation for the plastic strain $\boldsymbol{\varepsilon}_{\mathrm{pl}}$ is presented in section 3.1.

1.3.1. Constitutive models for creep

Constitutive equations for creep are based on the concept of creep potential, it is a scalar valued function addressed as W. No flow rule is required for creep deformations models since the onset of creep deformations does not depend on the yielding stress of the material. In order for creep to take place the material need to operate at an higher temperature then 0.3 T_{hom}. The flow potential $\phi(\boldsymbol{\sigma})$ is a function of the stress tensor, it describes the direction and magnitude of inelastic deformation under applied stresses. The inelastic strain rate tensor (for both creep and plastic deformations) reads:

$$\dot{\boldsymbol{\varepsilon}}_{\mathrm{in}} = \dot{\eta}\frac{\partial \Phi}{\partial \boldsymbol{\sigma}}, \tag{1.11}$$

where $\dot{\eta}$ is a scalar factor. In creep mechanics, being creep a thermally activate process, the flow potential is used without the concepts of yield condition or yield stress. Several forms to express the creep strain rate are available, according to the steady state theory by ODQVIST [79] it is:

$$\dot{\boldsymbol{\varepsilon}}_{\mathrm{cr}} = \frac{\partial W}{\partial \boldsymbol{\sigma}}, \tag{1.12}$$

here, $W(\boldsymbol{\sigma})$ is a scalar function named creep potential.

Under the assumptions of isotropic creep and dependence of the potential on the second invariant of the stress deviator, the potential transforms into the VON MISES potential [65]:

$$W = W(J_{2D}), \tag{1.13}$$

where J_{2D} is the second invariant of the stress deviator. To compare the creep behavior of the material under different state of stress the concept of equivalent stress according to the VON MISES formulation reads:

$$\sigma_{vM} = \sqrt{\frac{3}{2}\mathbf{S}\cdot\cdot\mathbf{S}} = \sqrt{-3J_{2D}}, \tag{1.14}$$

where $\mathbf{S}$ represents the deviatoric part of the stress tensor. With the use of Equation 1.14 the expression of the flow rule from Equation 1.12 can be obtained.

$$\sigma_{vM} = \frac{\partial W(\sigma_{vM})}{\partial \sigma_{vM}} \frac{3}{2} \frac{\mathbf{S}}{\sigma_{vM}}. \tag{1.15}$$

According to the "normality rule" the infinitesimal strain must be perpendicular to the strain surface, the creep strain tensor can be expressed as:

$$\dot{\boldsymbol{\varepsilon}}_{\mathrm{cr}} = \dot{\varepsilon}_{\mathrm{cr}}^{\mathrm{eq}} \frac{\frac{3}{2}\mathbf{S}}{\sqrt{\frac{3}{2}\mathbf{S}\cdot\cdot\mathbf{S}}} = \sqrt{\frac{3}{2}}\dot{\boldsymbol{\varepsilon}}_{\mathrm{cr,eq}}\mathbf{N}, \tag{1.16}$$

where $\mathbf{N}$ is the deviatoric tensor coaxial to stress deviator providing the direction of creep strain rate in the deviatoric stress space:

$$\mathbf{N} = \frac{\mathbf{S}}{\sqrt{\mathbf{S}\cdot\cdot\mathbf{S}}} \tag{1.17}$$

The equivalent creep strain rate can be expressed similarly:

$$\dot{\varepsilon}_{\mathrm{cr}}^{\mathrm{eq}} = \sqrt{\frac{2}{3}\dot{\boldsymbol{\varepsilon}}_{\mathrm{cr}}\cdot\cdot\dot{\boldsymbol{\varepsilon}}_{\mathrm{cr}}} = \frac{\partial W(\sigma_{vM})}{\partial \sigma_{vM}}. \tag{1.18}$$

As stated in Equation 1.16, the creep strain tensor exclusively depends on the deviatoric

part of the stress tensor and confirms how the hydrostatic part does not contribute to inelastic material deformations. Only in the secondary creep stage the Poisson's coefficient can be assumed for many metals to be equal to 0.5, as the material does not behave as an incompressible one throughout all the creep stages.

In [72] the equivalent creep rate is expressed as function of temperature and equivalent stress but also as the derivative of the ODQVIST potential (W) over the equivalent stress (σ_{eq}) as in Equation 1.19:

$$\dot{\varepsilon}_{\text{cr}}^{\text{eq}} = \frac{\partial W}{\partial \sigma_{\text{eq}}} = f(\sigma_{\text{eq}}, T). \tag{1.19}$$

The letter f indicates a general constitutive function for the creep strain rate according to [55]. Many options are available in literature for empirical functions of stress and temperature used to fit the experimental data [80], [83] and [95]. Assuming that the creep rate can be represented as function of two separate and independent on each other variables:

$$\dot{\varepsilon}_{\text{cr}}^{\text{eq}} = f_\sigma(\sigma_{\text{eq}}) f_T(T). \tag{1.20}$$

In the following some of the most common constitutive models are reported. Considering the great importance of the secondary creep compared to the other two creep stages the vast majority of constitutive equation are fitted only for this one.

The NORTON law is regulated by three parameters:

$$\dot{\varepsilon}_{\text{cr}}^{\text{eq}}(\sigma_{vM}, T) = A(T)\sigma_{vM}^{n} \exp\left(-\frac{Q}{RT}\right), \tag{1.21}$$

the hyperbolic-sine law by four parameters,

$$\dot{\varepsilon}_{\text{cr}}^{\text{eq}}(\sigma_{vM}, T) = C_1 \left(\sinh(C_2\sigma_{vM})\right)^{C_3} \exp\left(-\frac{C_4}{T}\right), \tag{1.22}$$

the double power law by six parameters,

$$\dot{\varepsilon}_{\text{eq}}^{\text{cr}}(\sigma_{vM}, T) = C_1 \left(\frac{\sigma_{vM}}{\sigma_{\text{ref}}}\right)^{C_2} \exp\left(-\frac{C_3}{T}\right) + C_4 \left(\frac{\sigma_{vM}}{\sigma_{\text{ref}}}\right)^{C_5} \exp\left(-\frac{C_6}{T}\right), \tag{1.23}$$

the ANAND model by nine parameters,

$$\dot{\varepsilon}^{\mathrm{cr}}_{\mathrm{eq}}(\sigma_{vM}, T, s) = C_1 \left(\sinh\left(C_2 \frac{\sigma_{vM}}{s}\right)\right)^{1/C_3} \exp\left(-\frac{C_4}{T}\right), \tag{1.24}$$

where:

$$s(t=0) = C_9. \tag{1.25}$$

Moreover, the following equations are required:

$$\dot{s}(\sigma_{vM}, T, s) = C_5 \left|1 - \frac{s}{s^*}\right| \operatorname{sign}\left(1 - \frac{s}{s_*}\right) \dot{\varepsilon}^{\mathrm{cr}}_{\mathrm{eq}}, \tag{1.26}$$

$$s_* = C_7 \left(\frac{\dot{\varepsilon}^{\mathrm{cr}}_{\mathrm{eq}}}{C_1} \exp\left(\frac{C_4}{T}\right)\right)^{C_8}. \tag{1.27}$$

Different creep constitutive laws are available with variable level of complexity for their implementation, the material parameters C_n are usually identified with a curve fit procedure.
As suggested by some of the creep laws reported above, the dependence on temperature can be expressed with the following expression:

$$f_T(T) = \exp\left(-\frac{Q}{RT}\right), \tag{1.28}$$

where, Q represents a physical constant named activation energy, T is the absolute temperature in kelvins (K) and R the universal gas constant. The activation energy measures the amount of energy required to allow molecular motion to take place. The universal gas constant must be expressed using units in accordance with the ones used for the activation energy. Many formulations of this equations are present in literature, depending on the type of test and material the best one is selected to reflect the highest possible accordance with the experimental data.

The Equation 1.28 also addresses the time dependence of the creep strain rate, it is called the Arrhenius equation or term.

Depending on the levels of stress and temperature, different mechanism of physical deformation may take place, this allows the introduction of the deformation mechanisms maps, firstly introduced by [30]. A possible representation for a deformation mechanism map is given in Figure 1.14, where the x- and y-axes are replaced by the homologous

temperature (T_{m} indicates the melting temperature) and the normalized equivalent stress (G represents the shear modulus). Deeper reviews are available at [29], [28] and [53]. The map can be used to indicate the dominant creep mechanism and strain rate for a given combination of stress and temperature.

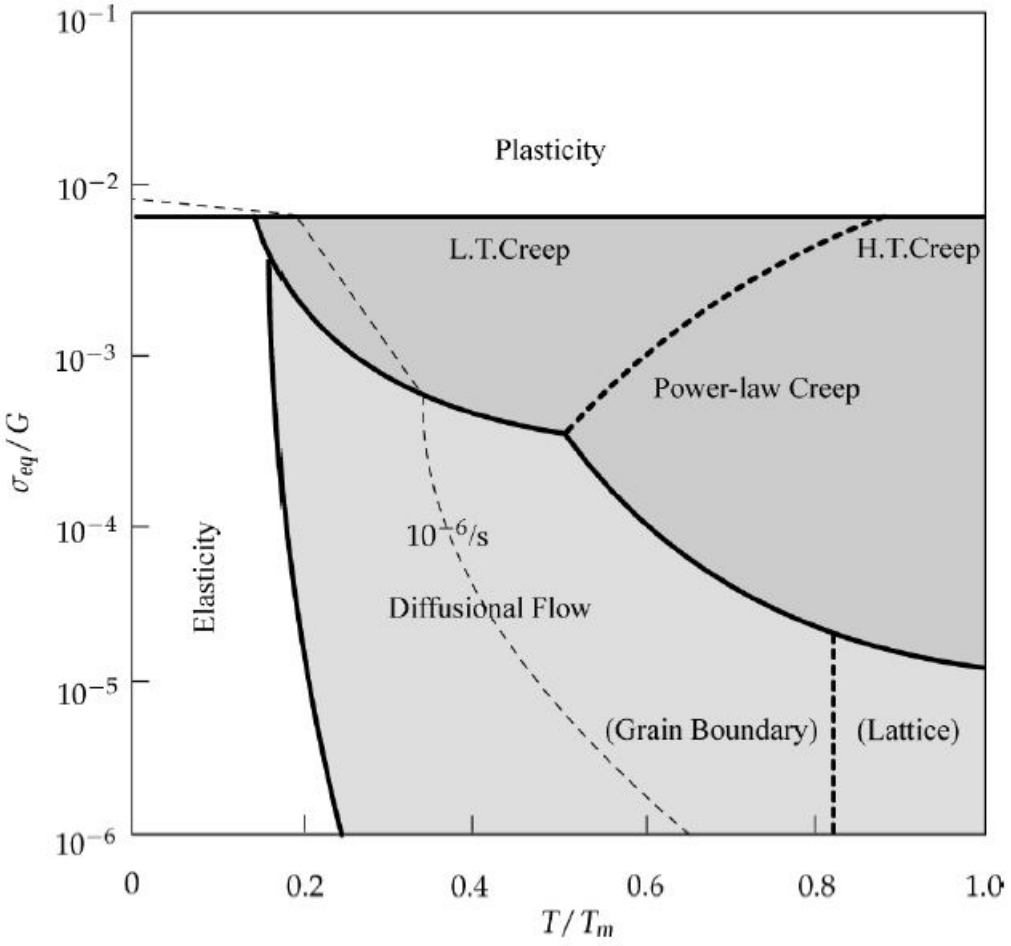

Figure 1.14: Deformation-mechanism map for creep (L.T.Creep - low temperature creep, H.T. Creep - high temperature creep) [72]

Different physical mechanisms can occur, but they can be categorized into two classes: *diffusional creep* and *dislocation creep* [18]. For $0.5 < T_{\mathrm{hom}} < 0.7$, reciprocal dislocation interactions and vacancy diffusion are the predominant mechanisms, while at higher temperatures, diffusion dominates, requiring much lower stresses.

1.4. Creep damage mechanics

In this section the methodologies to evaluate the damage level in the material for high homologous temperature and low stresses are analyzed, both from an historical point of view and for different complexity levels of the models.

Metallic materials undergoing low stresses and high temperatures tend to become brittle and be subjected to brittle fracture; this phenomenon is called thermal brittleness problem of metals [91]. In the case of creep of metals two main types of fracture are possible: viscous and brittle fracture. The first one is associated with large deformations before rupture while brittle fracture is related to the development of micropores and microcracks that merge together generating intergranular porosity and turning the material into a brittle one. In the case of thermal brittleness in metals, porosity accumulates along grain boundaries through vacancy diffusion and grain boundary slip, weakening the material's integrity and making it susceptible to brittle fracture at elevated temperatures.

It is thus valuable to monitor the evolution of damage throughout the creep process, which requires defining an appropriate damage parameter. Depending on the study's objectives and available data, the damage parameter may be scalar, vectorial, or tensorial.

1.4.1. Historical perspective

In the case of high temperature creep for metals, irreversible plastic creep deformations are accumulated over time together with defects (pores, cavities, microcracks) causing the material to rupture. The observation of creep phenomena occurred in the 1826 by Claude Louis Marie Henri Navier, the first scientific publications on the topic were made by Edward Neville Da Costa Andrade in [4] and [5].

Constitutive equations describe the evolution of the creep strain rate over time under certain boundary conditions. As mentioned in section 1.1, secondary creep is investigated, as it is the predominant one under the time duration point of view. The first suggestion in this direction is called Norton-Bailey power law in the case of one-dimensional creep [75] and [8]. The equation is presented in Equation 1.21 together with other alternatives.

The same concept was then developed for multiaxial loading by Odqvist [78] [79] and Bailey [8], these results were achieved with the use of the invariants of the stress tensor and of the creep strain rate tensor.

The concept of damage parameter was then introduced by Miner in [64] regarding the cyclic loading of materials and the consequent fatigue processes that are initiated. The

linearity of the damage phenomena was assumed. The MINER's rule states:

$$D = \sum_{i=1}^{n} \frac{n_i}{N_i} \tag{1.29}$$

where, n_i is the number of cycles at a given stress level i, N_i is the number of cycles to failure at that stress level i, n is the total number of different stress levels. Failure is predicted to occur when D reaches one.

To monitor the progression of damage within materials, continuum mechanics has expanded into a specialized branch known as Continuum Damage Mechanics (CDM). This field was pioneered by two Soviet scientists, L. KACHANOV [48] and Y. RABOTNOV [85], who introduced new concepts specifically for uniaxial tension: material damage (KACHANOV) and material effective stress (RABOTNOV). Over time, these theories have evolved to include vectorial and tensorial approaches to damage representation. In CDM, material rupture is understood as the result of gradual damage accumulation and degradation.

1.4.2. Scalar damage parameter

The simplest approach to modeling damage is the scalar representation. NOVOZHILOV [76] was the first to propose using relative pore size or the irreversible change in volume as a measure to express the damage parameter. Alternatively, two separate scalar parameters, the pore density and the average volume, have been used to characterize damage, as demonstrated in [98].

The scalar damage parameter is addressed as D and represents the material's instantaneous damage level. Alternatively, a scalar objective strength parameter was introduced in [90]. Creep-fatigue interactions have also been investigated using a scalar damage parameter for cumulative damage, notably in the work of LEMAITRE, who applied a thermodynamic approach to damage modeling [56, 57].

LEMAITRE's thermodynamic approach to damage mechanics provides a framework that connects damage evolution to the material's thermodynamic potential, effectively linking the macroscopic damage parameter D to internal energy dissipation mechanisms. In this formulation, damage is treated as an irreversible thermodynamic process, where the accumulation of damage correlates with the material's dissipation of energy under loading conditions. By using state variables that describe internal processes, LEMAITRE's approach enables the prediction of damage under complex conditions such as creep and

fatigue, integrating damage mechanics with thermodynamics to capture the material's response over time.

Being creep regulated by the formation and development of cracks, Dyson and Taplin suggested [23] to use the crack length as measure of the of the damage and the time required to grow a crack of the length of a grain as the time to fracture. In a later analysis [22] regarding cylindrical samples with recesses, it was observed that at low stresses cracks form in the regions around local necking phenomena and propagate towards the center of the specimen, while for higher stresses they propagate in the opposite direction.

A general consensus [7, 59] is build around the concept of using the material density as the most relevant parameter to represent porosity and damage. The degradation of the material is not fully irreversible [87]; the application of an hydrostatic stress is able to heal the pore formation reducing the creep rate and increasing the time to fracture. The damage is mainly related to the irreversible change of density (loosening) as well as the behavior of the material in creep. As damage accumulates, mechanical properties degrades leading to a reduction of elastic modulus, yield stress and ultima tensile stress.

Damage in materials is often characterized by the development of porosity, which can be quantified by measuring changes in material density due to loosening. A single law governing the accumulation of loosening is commonly applied, as described in [7]. Conditions that favor this accumulation include stresses approaching the yield strength, where grain boundary sliding and vacancy diffusion exert significant influence on the material's structure [91].

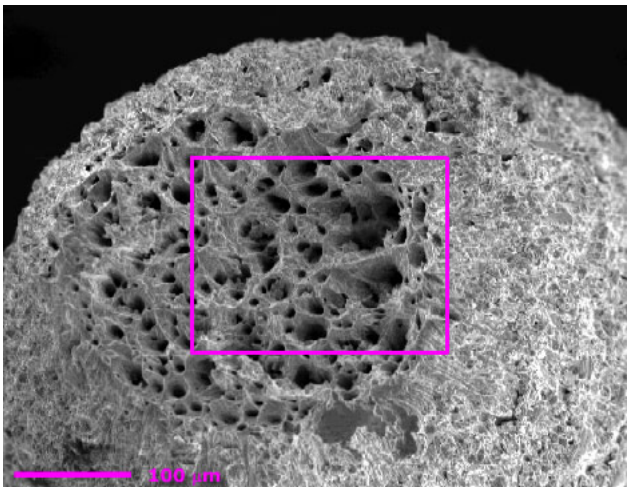

Figure 1.15: Cavity formation in the rupture section [99]

In Figure 1.15 the surface of rupture for a solder metallic wire is shown, it exhibits ductile

fracture as consequence of the cavity formation. The image is acquired with the use of a scanning electron microscope (SEM). It is to remark that, even if crack nucleation is at all creep stages present, the damage process takes place only in the last part of the creep curve.

A decrease of density is usually associated with local fracture at stress concentration points like inclusions or at grain junctions [6, 12, 13], density measures are usually carried out with the use of hydrostatic weighing methods.

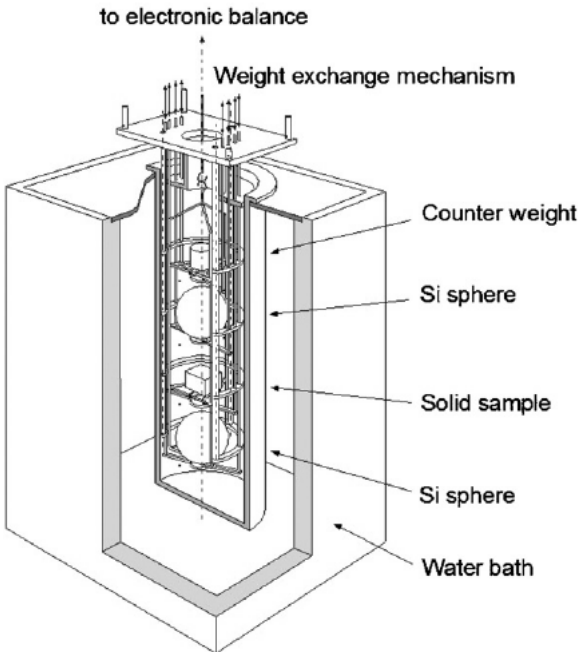

Figure 1.16: Apparatus for hydrostatic weighting developed at NMIJ [101], [11]

In Figure 1.16 an hydrostatic weighing system is represented. The density of the samples is compared to the one of the silicium spheres through the measuring of the buoyancy forces acting on them in the liquid.

In the development of the present work the Kachanov-Rabotnov damage model is implemented; fundamentals about the model are given in the following. The creep as well as the damage accumulation are treated subsequently as isotropic; however from microstructural observations it is clear that the creep damage has a directional effect. As consequence of that, the right mathematical tool to describe it would be a tensor.

The continuity parameter is defined as:

$$\psi = \frac{A_0 - A_D}{A_0}, \tag{1.30}$$

where A_0 represents the initial cross section area of the specimen and A_D the area occupied by voids, micro-cracks or cavities. The effective area is the area that carries the load and is defined as:

$$A_{\text{eff}} = A_0 - A_D. \tag{1.31}$$

The continuity parameter in Equation 1.30 assumes values equal to one in the case of the pristine material and zero when the specimen fractures.

The scalar damage parameter was introduced for the first time by KACHANOV [48]. D represents the damage parameter and can assume values in the range $0 < D < 1$. Damage is generated as a consequence of the increase of the stress in the material since the creation of voids and cavities reduces the resistance section of the material, the effective stress can be defined as [49]:

$$\sigma_{\text{eff}} = \frac{F}{A_{\text{eff}}} = \frac{\sigma}{1-D}, \tag{1.32}$$

where, F is the applied load, A_{eff} is the effective resistant section, σ is the stress applied to the nominal section.

The damage impacts the evolution of the creep rate; the constitutive equation, assuming the power law, is defined as:

$$\dot{\varepsilon}_{\text{cr}} = \dot{\varepsilon}_{\text{cr}}(\sigma, D) = \frac{a\sigma^n}{(1-D)^m}, \tag{1.33}$$

where a,n and m are material constants. At the same time the damage evolves according to:

$$\dot{D} = \frac{b\sigma^k}{(1-D)^l}, \tag{1.34}$$

where b,k and l are material dependent constants. Assuming $k = l$ and integrating Equation 1.34, it is possible to approximately compute the rupture time t_{cr}, defined as the instant where $D = 1$. The critical time to rupture is expressed as:

$$t_{\text{cr}} = \frac{1}{(l+1)b\sigma^l}. \tag{1.35}$$

In a real scenario the breakage of the specimen takes place earlier due to the increase of stress concentration effects.

1.4.3. Energy related formulation of the scalar damage parameter

An alternative damage formulation can be proposed based on the energy dissipated by the material when subjected to mechanical cycling. The cumulated energy dissipated by the material during cycling is taken as an indicator of the residual mechanical properties, independently from the damage level induced at each cycle. A novel formulation of the damage parameter (D) is introduced, it is assumed that the damage at a certain instant can be expressed as:

$$D = \frac{\Delta W_{\text{tot}}}{C_5} = \frac{\sum \Delta W}{C_5}. \tag{1.36}$$

Here, ΔW represents the energy density dissipated at each cycle due to plastic work, typically expressed in [MJ/m^3] or more practically in [MPa]. The term $\sum \Delta W$ denotes the cumulative energy density dissipated over the total number of cycles, while C_5 is a material constant representing the total energy density the material can dissipate before failure. Material damage is defined as the ratio of the dissipated energy to the total dissipative capacity of the material.

The damage evolution equation can be assumed as:

$$\dot{D} = \frac{1}{C_5}\Delta \dot{W}_{\text{tot}} = \frac{1}{C_5}\boldsymbol{\sigma} \cdot\cdot\, \dot{\boldsymbol{\varepsilon}}_{\text{cr}} = \frac{1}{C_5}\boldsymbol{\sigma}_{\text{eq}}\dot{\boldsymbol{\varepsilon}}^{\text{eq}}_{\text{cr}}. \tag{1.37}$$

The equivalent creep strain and the dissipate energy density are integral quantities and can be expressed as:

$$\varepsilon^{\text{eq}}_{\text{cr}} = \int_0^t \dot{\varepsilon}^{\text{eq}}_{\text{cr}}(\sigma_{\text{eq}}(\tau), T(\tau))\, d\tau, \tag{1.38}$$

$$\Delta W_{\text{tot}} = \int_0^t \boldsymbol{\sigma} \cdot\cdot\, \dot{\boldsymbol{\varepsilon}}_{\text{cr}}\, d\tau. \tag{1.39}$$

The intent is to replicate the are of the hysteresis loop in the while of its evolution.

1.4.4. Damage vector

Defects such as cavities, micropores, or microcracks emerge in the material's microstructure due to applied loads, leading to damage accumulation. Investigating the direction of the applied load can be useful to identify directions in which defects are more likely to develop. For instance, microcracks tend to form perpendicular to the direction of maximum principal stress. In such cases, a vectorial or tensorial approach is required to accurately model the directional nature of damage accumulation.

L. Kachanov approached this problem introducing not only the damage parameter D but also its direction [50]. As a consequence, the damage does not accumulate uniformly in all planes but proportionally to the normal stress acting perpendicular to that plane; local fracture will take place only when the critical value of damage is reached in one plane. In order to generate complete fracture, the fracture front needs to go through the considered volume.

Namestnikova and Shesterikov suggested in [71] a new approach to the damage parameter value:

$$D = \sqrt{D_1^2 + D_2^2 + D_3^2}, \tag{1.40}$$

where, D_i are the accumulation of the damage vector along the principal stress direction $i = 1, 2, 3$, $D(0) = 0$ is the initial value for damage and $D(t^*) = 1$ is the final valued for damage reached at the critical time t^*.

This approach also enables the study of an anisotropic damage [58]. Anisotropic damage is not uniformly accumulated in all direction but mainly along one or two directions generating an anisotropic structure if the material is originally isotropic. The same methodology can be used for studying creep in materials that already present a material anisotropy [72].

1.4.5. Damage tensor

The damage tensor approach is used to investigate the dependencies of the fracture time on the anisotropic characteristics of a material, whether these are inherent or arise due to induced stresses [18]. Tensors of different orders can be employed to capture varying levels of damage complexity [91]. The concept of a damage tensor was first introduced by Rabotnov in [84]. Around the same time, Johnson presented foundational research on the behavior of metals under complex stress states during creep [46]. In Johnson's

formulation, the hypothesis of proportionality between stress deviators and creep strain rate deviators was proposed, with the proportionality factor being a function of both the stress and the creep strain rate tensors. This theoretical framework laid the groundwork for understanding creep in metals subject to multi-axial stress conditions and for accurately modeling material behavior under high-stress applications.

In [3], ALTENBACH suggested the principal types of damage parameters, analyzing the differences in compressive and tensile properties as well as the anisotropic nature of damage accumulation. In [69], MURAKAMI adopted a mixed methodology combining continuum mechanics and materials science to investigate the anisotropic behavior of the damage tensor parameter, modeling it as a second-rank tensor to describe the density of pores in three principal planes. It was determined that, for low pore densities, a scalar damage parameter is adequate for describing long-term damage.

In [98] and [17], it was concluded that, under complex loading conditions, both isotropic and kinematic hardening must be considered for accurate material modeling. A collection of established variants for constitutive relations in creep theory for isotropic materials, which also account for damage during deformation, is presented in [1].

2 | Experimental data processing

In this chapter, available data from [62], is analyzed. Specifically, material parameters for the hyperbolic-sine and NORTON creep models are identified through fitting experimental results related to the secondary creep strain rate, using various algorithms. The statistical distribution of these identified parameters is explored. Additionally, the evolution of creep strain, damage, and the hysteresis loop over strain controlled cycling is represented. A numerical model is developed using Python, and the outcomes are compared with results from Abaqus simulations that include the use of user-defined FORTRAN subroutines.

2.1. Experimental procedure

Detailed overview over the data acquisition procedure is present in [62]. Cylindrical cross section uniaxial specimens of SAC305 have been tested, these lead-free solders are prepared in glass tubes as describes in [38]. The microstructure of such specimens is regulated with the use of a reflow profile as common practice in BGA assemblies. The mechanical apparatus used to conduct both the initial precondition damage and the subsequent creep tests is represented in Figure 2.1.

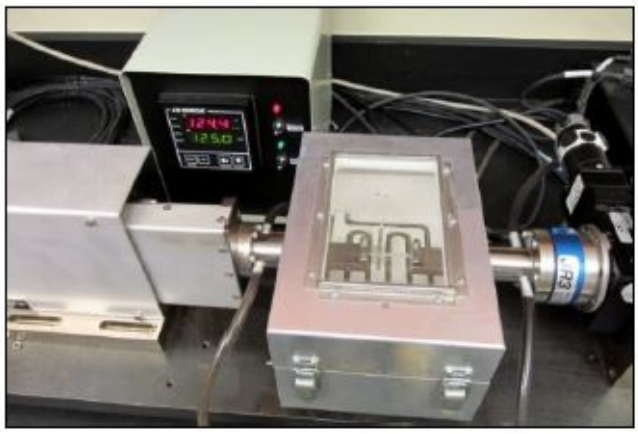

Figure 2.1: Micro-tester equipped with thermal chamber [62]

In the precedent figure, the thermal chamber is well visible in the center; its function is

to maintain a constant temperature at the required level. A short gauge length is used to limit the probability of specimen buckling. Diameter and gauge length are respectively 1.2 mm and 5 mm. Strain controlled mechanical cycling tests are conducted applying every time the required level of damage. The imposed damage level at each cycle is assessed by analyzing at the area in the stress-strain plain of the hysteresis loop. In Figure 2.2 an hysteresis cycle is depicted.

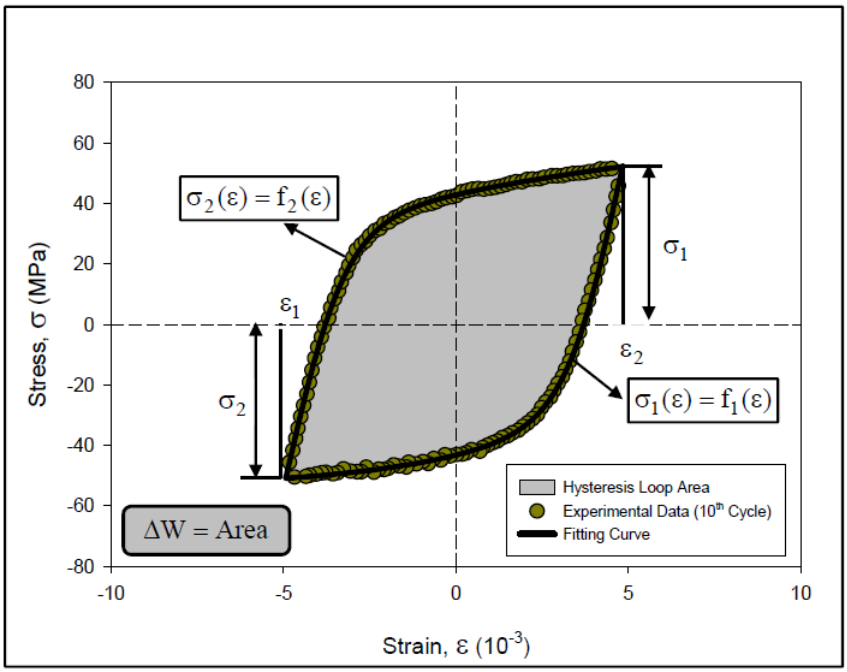

Figure 2.2: Typical hysteresis loop and area calculation [32]

By applying a couple of hyperbolic tangent models and computing the difference integral, it was possible to compute the dissipated energy at each cycle, a graphic example is given in Figure 2.2, [32].

Four initial energy dissipation levels, or initial damage levels per cycle, are considered: ΔW = 0.25, 0.50, 0.75, and 1 MJ/m^3 at room temperature (25°C). Each damage level involves a different number of cycles, resulting in different rates of damage accumulation. These initial energy dissipation levels are chosen based on findings from previous FEM simulations [38]. As the material is cycled and damage increases the mechanical performances degrade. The 20th cycle for each of the applied strain ranges is represented in Figure 2.3.

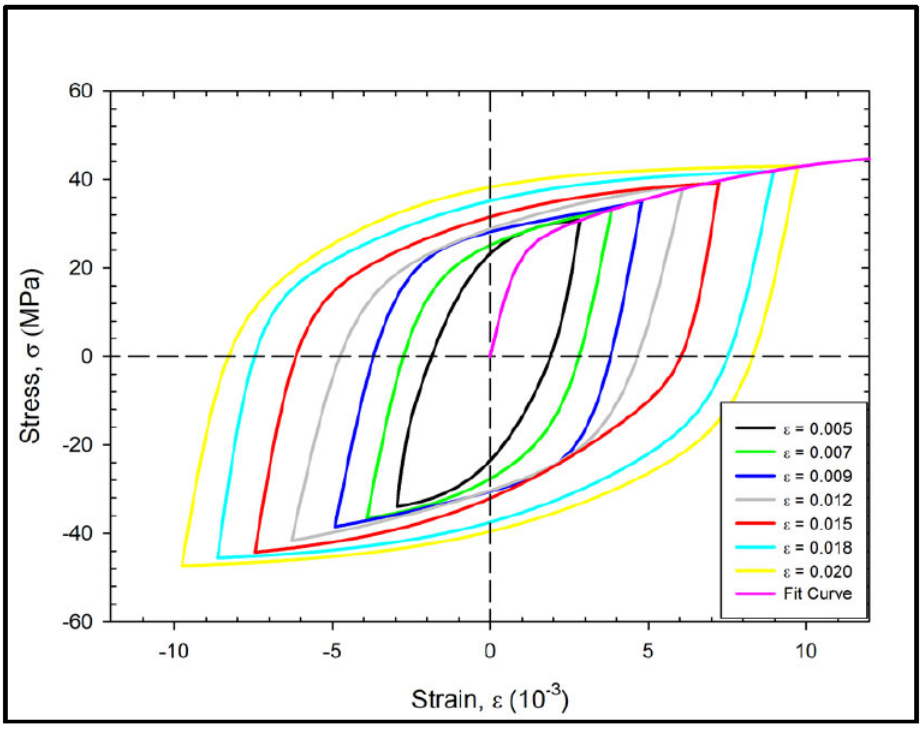

Figure 2.3: 20th hysteresis loops for SAC305 subjected to mechanical cycling with different strain ranges [38]

SAC305 samples are tested at different total strain range amplitudes: 0.005, 0.007, 0.009, 0.012, 0.015, 0.018, and 0.020. The hysteresis loop describes the initial damage level in the first cycles. With the use of an empirical polynomial model it was possible to fit the data regarding the initial loop area vs. strain range, resulting curve is reported in Figure 2.4.

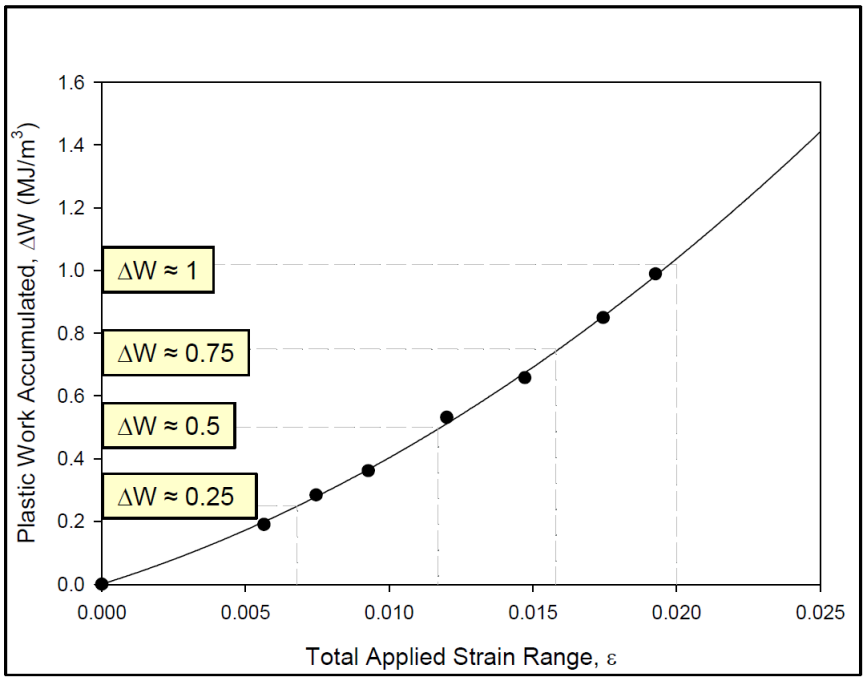

Figure 2.4: Initial plastic work vs. total strain range (SAC305, cycling at 25 °C) [62]

All tests are conducted with a constant strain rate of $\dot{\varepsilon} = 0.002\ \mathrm{s}^{-1}$. This method generates what can be called a "test matrix" with various preconditioned specimens. Subsequently to the mechanical cycling, creep tests have been performed both on differently damaged specimens and on non-damaged specimens. The tests have been conducted at 25°C room temperature with stresses equal to: 7.5, 10, 12, 15 and 18 MPa. Only the steady state secondary creep is taken in analysis for each one of the obtained test curves. Results of the evolution of the secondary creep strain rate for the different stress levels are shown in Figure 2.5.

In [42] the evolution of mechanical properties over the mechanical cycling is reported in detail.

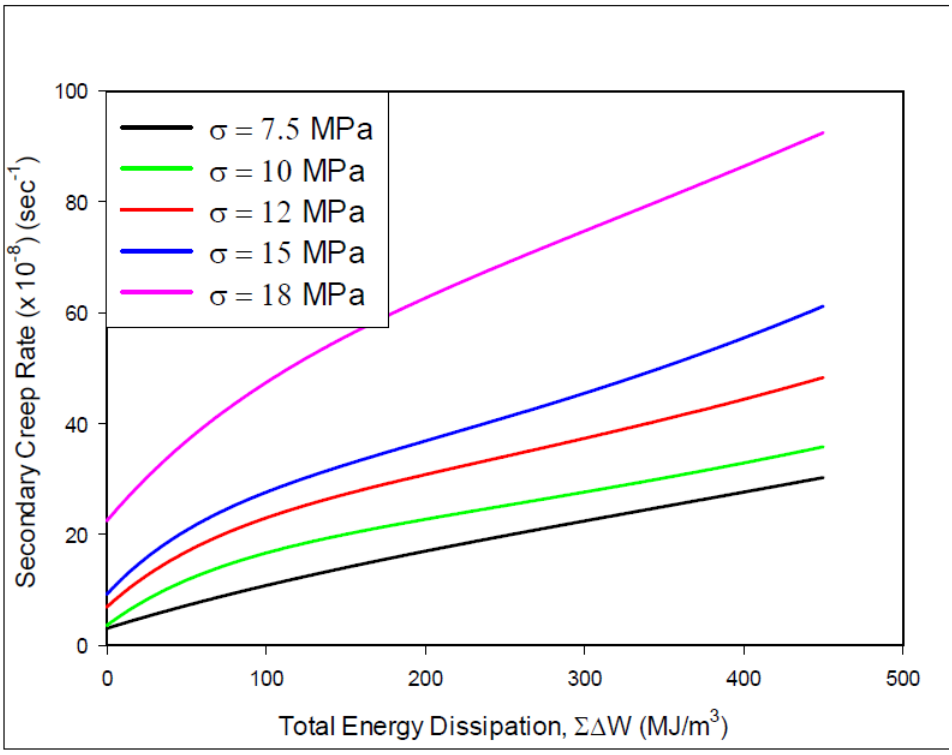

Figure 2.5: Evolution of the steady state secondary creep rate ($\dot{\varepsilon}$) with the total energy dissipated in the material for various applied stress levels [62]

2.2. SAC305 material properties

Due to their good thermal fatigue properties SAC alloys are usually selected as solder materials in BGA assemblies, the abbreviation SAC represents the three main components, silver, gold and copper. In particular SAC 305 corresponds to 96.5Sn–3.0Ag–0.5Cu. These alloys must undergo elevated temperatures for prolonged time; the aging process is then inevitable. As a consequence, intermetallic particles tend increase in size resulting in a coarser structure [31]. Naturally the mechanical properties of the material will be strongly affected by such changes, leading to a weaker material. The dependence of the mechanical properties on the aging process is explored in [9].

When investigating solders, the first distinction can be made between lead and lead free-solder. The first category is characterized by alloys that combine tin (Sn) with lead (Pb). Their melting temperature is lower (183°C for Sn60Pb40), have a large deformation reserve and form strong joints; however, lead is toxic and therefore its use in electronics is restricted and limited to high reliability applications like aerospace and military. Lead-free solders display higher melting temperature, are easier to handle and recycle being non-toxic. The most used solder is the SAC305 with the following composition

96.5Sn–3.0Ag–0.5Cu. This alloy is not eutectic meaning that the melting point is a range starting at 217°C and ending at 220°C [27]. Today, SAC305 is widely used in the industry, even if it does not have an eutectic composition. This mainly depends on its good thermal cycling properties, good mechanical characteristics and compatibility with many industrial processes making it compatible with many common processes or equipments. Moreover, it exhibits excellent properties for what concerns tensile strength, creep resistance, and fatigue life under various loading and thermal cycling conditions.

Lead-free solder are characterized by the number of different elements used in the alloy, they can be binary (only two elements), tertiary and so forth. A typical example for a binary lead-free solder is SnAg3.5 with a melting temperature in the range 217-221°C, being a non-eutectic alloy. SAC305 is an example for a tertiary lead-free solder since it is constituted by three elements. Considering the SAC305 with its melting temperature and assuming a working condition of 25°C as for the data available for this work, the corresponding homologous temperature is computed in Equation 2.1:

$$T_{\text{hom}} = \frac{T}{T_m} = \frac{25 + 273.15}{217 + 271.15} = 0.61. \tag{2.1}$$

Here, T_m represents the melting temperature which is equal to 217 °C. Since the melting point spans a range, the lower value is used, as the material begins to lose integrity at the start of the melting range. Together with considerations made in section 1.1 it is clear how the creep behavior of the SAC305 at this temperature cannot be neglected, as it is the most prominent phenomenon.

Following the trend of miniaturization in the microchip sector, solder joints are becoming increasingly smaller. In this context, individual solder points can reach dimensions where the solder can no longer be assumed to be homogeneous and isotropic. Under these conditions, each solder joint is said to exhibit an oligocrystalline microstructure (comprised of a few, relatively large grains), giving rise to unique thermomechanical properties [45].

One approach to address this scenario is by introducing nucleants during solidification, which enables the grains to align in a preferred orientation. Alternatively, a directional characterization can be imparted to the material through directional solidification (DS), as demonstrated in [2]. Ideally, the optimal solution would be to achieve a single-crystal structure.

When discussing SAC305, it is important to note that more than 90% of its structure consists of the β-Sn phase, which typically forms an oligocrystalline microstructure. The body-centered tetragonal (BCT) crystal structure of β-Sn introduces intrinsic anisotropy,

promoting the development of a heterogeneous microstructure during solidification [45].

In this work, SAC305 is assumed to be homogeneous and isotropic, given the relatively large dimensions of the test specimen (with a diameter of 1.2 mm and a gauge length of 5 mm). This assumption treats the material as a composite of many randomly oriented grains, leading to no preferential loading direction for the specimen.

2.3. Material parameters identification

2.3.1. Available data

From what described in section 2.1, an extensive dataset was collected and analyzed. For the purposes of this work, only a subset of the data was made available. This dataset comprises eighty-five entries, each representing a tested specimen. The dataset is organized into five blocks, each containing seventeen tests. Each entry is split into two main sections: one detailing the pre-cycling conditions and the other describing the subsequent dead-load test results. The five blocks share identical pre-cycling conditions but differ in the engineering stress applied during the dead-load test, specifically set at 7.5, 10, 12, 15, and 18 MPa.

Within each block, the seventeen tests are structured as follows: one specimen remains uncycled (pristine), while the remaining sixteen are cycled for 50, 100, 300, and 600 cycles across four initial damage levels (0.25, 0.50, 0.75, and 1 MJ/m^3), totaling sixteen tests. For each entry, the dataset includes information on the number of cycles, temperature, applied strain range, and total dissipated energy.

In the creep test section of the dataset, the applied engineering stress, the temperature and the steady state creep strain rate are reported.

2.3.2. Isothermal formulation of creep laws

Given a creep strain rate model based on the hyperbolic-sine law, as expressed in Equation 1.22, a simplification is possible due to the constant temperature of 25°C maintained across all tests:

$$\tilde{C}_1 = C_1 \exp\left(\frac{C_4}{T}\right). \tag{2.2}$$

Analogous simplifications can be made regarding other creep strain rate laws like the Norton law. The hyperbolic-sine law can be rewritten as:

$$\dot{\varepsilon}_{\mathrm{cr,eq}} = \tilde{C_1} \sinh\left(C_2 \frac{\sigma_{\mathrm{eq}}}{1-D}\right)^{C_3}. \tag{2.3}$$

The NORTON law becomes:

$$\dot{\varepsilon}_{\mathrm{cr,eq}} = \tilde{B_1} \left(\frac{\sigma_{\mathrm{eq}}}{1-D}\right)^{B_3}. \tag{2.4}$$

The damage D for the hyperbolic-sine law at the end of the pre-damage phase is expressed with Equation 1.36. When working with the NORTON the C_5 parameter must be substituted with B_5.

The total energy dissipated in the pre-damage phase is expressed as:

$$\Delta W_{\mathrm{tot}} = \sum_{j=1}^{m} \Delta W. \tag{2.5}$$

Where m represents the number of cycles applied to the specimen in the pre-damage phase; for each value of the strain range the following cycles are applied: 50, 100, 300 and 600.

The parameter C_5 indicates the total energy dissipated before the breaking of the specimen:

$$C_5 = \sum_{i=1}^{n} \Delta W. \tag{2.6}$$

Here n indicates the number of cycles to failure and ΔW the energy dispersed at each cycle before breaking, in the case of a strain controlled fatigue test.

The parameter identification problem consists in the quantification of the parameters $\tilde{C_1}, C_2, C_3, C_5$ (or $\tilde{B_1}, B_3, B_5$) such that the error, the difference between experimental and numerical values of the creep strain rate, reaches a minimum point, the error is computed according to Equation 2.7:

$$\mathrm{r} = \mathrm{NRMSE} = \frac{1}{\frac{1}{N}\sum_{i=1}^{N} \dot{\varepsilon}^{\mathrm{cr}}_{i,\mathrm{exp}}} \sqrt{\frac{1}{N}\sum_{i=1}^{N} \left(\dot{\varepsilon}^{\mathrm{cr}}_{i,\mathrm{exp}} - \dot{\varepsilon}^{\mathrm{cr}}_{i}\left(\tilde{C_1}, C_2, C_3, C_5\right)\right)^2}. \tag{2.7}$$

The NRMSE, or Normalized Root Mean Square Error, is a commonly used metric for evaluating the accuracy of numerical models against experimental results. This index is particularly useful as it penalizes large errors, making discrepancies more apparent. Additionally, the NRMSE is expressed in the same units as the measured variable, which enhances its intuitive application. In the following sections, it will be referred to simply as r.

In Equation 2.7, N indicates the number of experimental data collected, $\dot{\varepsilon}^{\mathrm{cr}}_{i,\mathrm{exp}}$ is the i-th experimental creep strain rate from experiments, while $\dot{\varepsilon}^{\mathrm{cr}}_{i}$ is the i-th creep strain rate from the used creep law, in this case the hyperbolic-sine law or NORTON law.

Two different steps are carried out in the following; first the identification of material parameters with the "energy" approach, subsequently a strain profile is applied and creep properties evolution is studied with the "integration" approach. The aim is to fit the material parameter to secondary creep strain rate values and then develop a numerical model able to reproduce the evolution of creep quantities during cycling.

Before the dead load test, the specimens are pre-damaged in a fully reversed triangle wave strain-controlled test with strain ranges of 0.0068, 0.0117, 0.0158, and 0.02 at a constant strain rate of $\dot{\varepsilon} = 0.002\ \mathrm{s}^{-1}$. Since the strain rate is held constant while the strain range varies, each strain profile has a different periodicity. These profiles are represented in Figure 2.6.

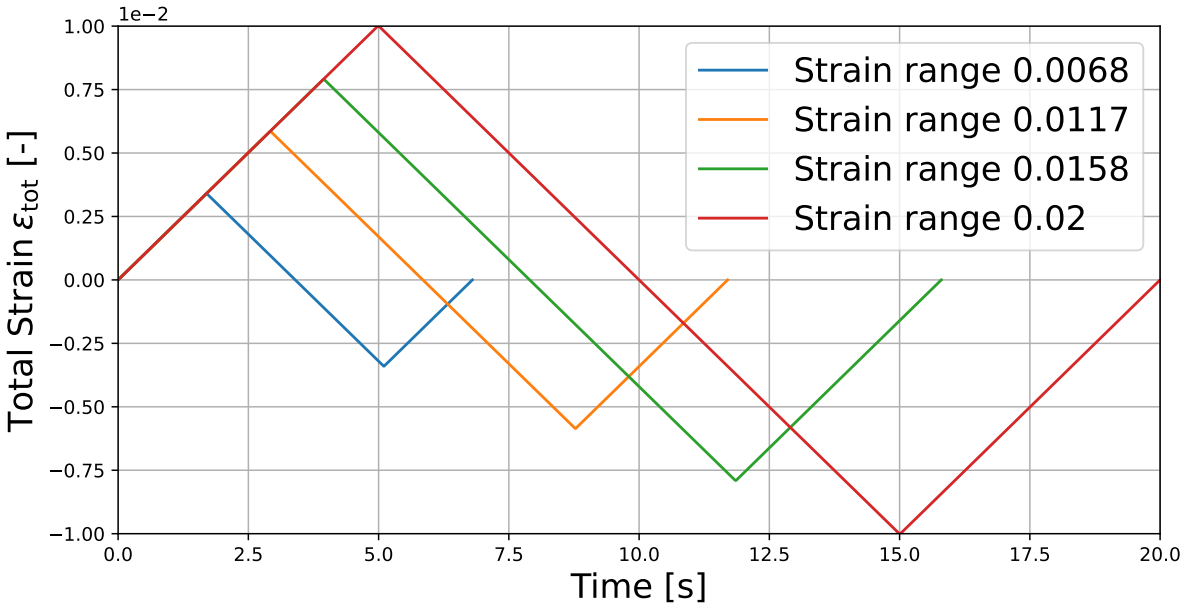

Figure 2.6: Fully reversed triangle wave strain profile applied on the specimens, strain rate equal to $0.002\,\mathrm{s}^{-1}$

Among the other possible presented approaches in [36], the Monte Carlo method is implemented. In particular 500 000 combination guesses for the constants $\tilde{C_1}, C_2, C_3, C_5$ are simulated, the set of parameters that minimizes r is selected. The minimum computed value is r = 0.165. The minimization of the residuals (r) is a complex task; the function is characterized not simply by a nonlinear structure but also by a large number of local minima [37].

Merging Equation 2.3, Equation 2.4 with Equation 1.36, the creep laws are reformulated as:

$$\dot{\varepsilon}_{\mathrm{cr}}^{\mathrm{eq}} = \tilde{C_1} \left(\sinh \left(C_2 \frac{\sigma_{\mathrm{eq}}}{1 - \frac{\Delta W_{\mathrm{tot}}}{C_5}} \right) \right)^{C_3} \tag{2.8}$$

$$\dot{\varepsilon}_{\mathrm{cr}}^{\mathrm{eq}} = \tilde{B_1} \left(\frac{\sigma_{\mathrm{eq}}}{1 - \frac{\Delta W_{\mathrm{tot}}}{B_5}} \right)^{B_3} . \tag{2.9}$$

Equation 2.7 can then be rewritten substituting the numerically computed creep strain rate with Equation 2.8 or Equation 2.9.

2.3.3. Optimization procedure

Referring to Equation 2.7 the experimental creep strain rate, the stress and the dissipated energy are determined from the dataset, the material parameters C_n must be identified such that r is minimized.

The NRMSE represents the objective function which assumes normally values in the range from zero to one. The optimization procedure is executed with the use of the Python programming language and different libraries, like `scipy.optimize.minimize` [94] and `nlopt.opt` [47], are implemented. The procedure is independent from the use of a particular creep law. By implementing a different law, the expression of the objective function will change as well as the number of parameters to be identified, four for the hyperbolic-sine law and only three in the case of the NORTON law.

The optimization problem is highly nonlinear, making the procedure complex. Nonetheless, various approaches are evaluated, and the most effective one is selected. In the following, a comparison between different optimization procedures is presented, with data referring specifically to the hyperbolic-sine law.

Before introducing the specific optimization algorithms used, it is important to discuss the

bounds and initial guesses applied to solve the problem. The parameters to be identified technically only require a lower bound, as they must remain positive; however, an upper bound is also imposed to aid the optimization software. These bounds are detailed in Table 2.1.

Optimization procedure	$\tilde{C_1}[s^{-1}]$	$C_2[\text{MPa}^{-1}]$	C_3[-]	C_5[MPa]
free	$(10^{-9}, 10^{-3})$	$(10^{-3}, 1)$	$(1, 10)$	$(250, 10000)$
constrained	$(10^{-9}, 10^{-3})$	$(10^{-3}, 1)$	$(3, 10)$	$(250, 10000)$

Table 2.1: Bounds used for the optimization procedure of the parameters of the hyperbolic-sine creep law

The ranges reported above are derived from data available in the literature. The aim is not to precisely define the upper and lower bounds but rather to assist the solver by limiting the search space. Unless otherwise specified, the same bounds are applied across all optimization procedures.

As shown in Table 2.1, two sets of bounds are provided: one for "free" optimization and another for "constrained" optimization. The constrained approach imposes stricter lower bounds, particularly limiting the value of C_3 to prevent unrealistic outcomes. Further details on this approach are provided below.

For the NORTON law the bounds are reported in Table 2.2.

Optimization procedure	$\tilde{B_1}[s^{-1}]$	B_3[-]	B_5[MPa]
free	$(10^{-12}, 10^{-5})$	$(1, 10)$	$(250, 10000)$

Table 2.2: Bounds used for the optimization procedure of the parameters of the NORTON creep law

The initial guesses are also of crucial importance in the optimization procedure, values for the hyperbolic-sine law are reported in Table 2.3. These values are obtained from results of [36]. In the case of the NORTON results are presented in Table 2.4.

Initial guess	$\tilde{C_1}[s^{-1}]$	$C_2[\text{MPa}^{-1}]$	C_3[-]	C_5[MPa]
Hyperbolic-sine	1.1×10^{-6}	3.6×10^{-2}	3	535

Table 2.3: Values of the initial guesses for hyperbolic-sine creep law

Initial guess	$\tilde{B_1}[s^{-1}]$	B_3[-]	B_5[MPa]
NORTON	7.5×10^{-7}	3	946

Table 2.4: Values of the initial guesses for NORTON law

Initial guesses for the NORTON law are selected with a series of trials and errors.

The first library to be considered is the `scipy.optimize.minimize`, this library allows to minimize a scalar function (the objective function) of one or more variables. This method is limited by the fact that it only allows the search for a local minimum point, however different methods are available for both bounded and unbounded problems.

The methods "COBYLA", "L-BFGS-B" and "SLSQP" are implemented. The results are reported in Table 2.5 together with the results from other libraries. It is evident how the optimization result is strongly dependent on the bounds; in many cases the optimization process fails if the bounds are too wide.

Optimization library	$\tilde{C_1}[s^{-1}]$	C_2[MPa^{-1}]	C_3[-]	C_5[MPa]	r [-]
minimize-COBYLA	8.067×10^{-7}	1.166×10^{-2}	1.648	535	0.825
minimize-L-BFGS-B	3.072×10^{-6}	1.117×10^{-2}	1.429	804	0.221
minimize-Nelder-Mead	5.785×10^{-6}	1×10^{-2}	1.665	930	0.209
nlopt-free	1.361×10^{-6}	2.243×10^{-2}	1.588	945	0.209
CMA-ES	5.785×10^{-6}	1×10^{-2}	1.665	929	0.212
mystic-diffev2	5.784×10^{-6}	1×10^{-2}	1.665	930	0.209
nlopt-undamaged	2.169×10^{-7}	4.901×10^{-2}	2.766	–	0.178
nlopt-constrained	2.670×10^{-6}	2.781×10^{-2}	3	1590	0.360

Table 2.5: Results for the material constants for the hyperbolic-sine laws, data are computed with the use of Python and different libraries

Among the optimization libraries used, `nlopt.opt` is employed specifically for solving nonlinear optimization problems. Another algorithm applied is the Covariance Matrix Adaptation Evolution Strategy (CMA-ES) from the `cma` library. This algorithm allows a stochastic numerical optimization, designed for "complex" problems with a continuous search space. It is suitable for both constrained and unconstrained problems; however, the number of function evaluations required is typically around one hundred times the number of dimensions in the search space.

In addition, also the `diffev2` module from the `mystic` library is used for the optimization process. This module allows the application of a collection of optimization routines based on Storn and Price's differential evolution algorithm.

The results reported in Table 2.5 evidence a sufficient level of success of the applied optimization strategy due to the small value obtained for the residuals with different algorithms. Nevertheless, the outcomes cannot be judged as fully satisfactory since the

predicted values for C_3 are unrealistic. To gain a deeper understanding of the issue, a further optimization procedure is carried out considering only the rows from the dataset for undamaged specimens, with results reported in Table 2.5. Another optimization procedure is executed using three as the lower bound for the constant C_3. This term is positioned in the exponent of Equation 2.8, and as a consequence, a small variation in its value has a great impact on the shape of the hysteresis cycle and on the predicted creep strain rate. The optimization procedure is executed once more with the bounds reported in Table 2.1.

In the case of the NORTON law the process is more straightforward and only the `nlopt` library is used; the results are displayed in Table 2.6.

Creep law	$\tilde{B_1}[s^{-1}]$	B_3[-]	B_5[MPa]	r [-]
NORTON	7.104×10^{-9}	1.388	1379	0.33

Table 2.6: Results for the material constants for NORTON creep law, data computed with the use of `nlopt` library

In the following sections, additional optimization procedures are performed using the `nlopt` library. This library offers various algorithms, allowing the selection of methods best suited for different problems. Among available options, `nlopt` is particularly reliable and less prone to numerical errors.

Using the hyperbolic-sine law parameters from the fourth row of Table 2.5 and the parameters from Table 2.6 for the NORTON law as references, a mesh grid is created, and the experimental data is visualized in a 3D plot. Additionally, interpolated surfaces are generated based on the optimized parameter values. These results are displayed in Figure 2.7 for the hyperbolic-sine law and in Figure 2.8 for the NORTON law.

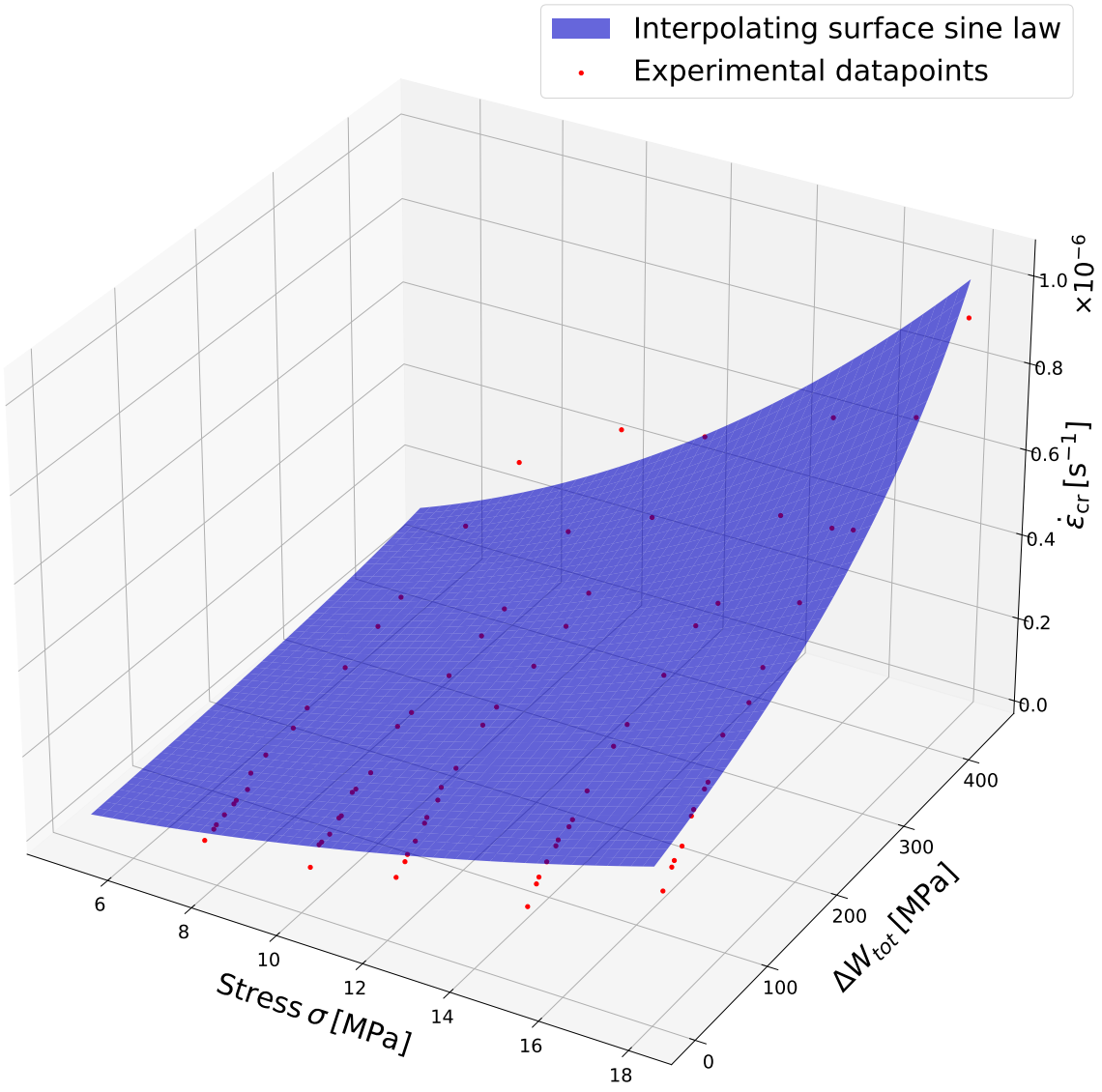

Figure 2.7: Comparison between experimental datapoints and interpolated surface using the hyperbolic-sine law with the free-nlopt parameter set

On the in-plane axes, the stress σ and the dissipated energy in pre-damage ΔW_{tot} are indicated; each experimental condition is represented by a combination of the two. The ΔW_{tot} represents the damage introduced in the pre-damage and σ the stress applied in the subsequent dead load test. The z-axis reports the constant secondary creep strain rate from experiments. It can be observed how higher values of pre-damage and applied stress generate higher values in the secondary creep strain rate.

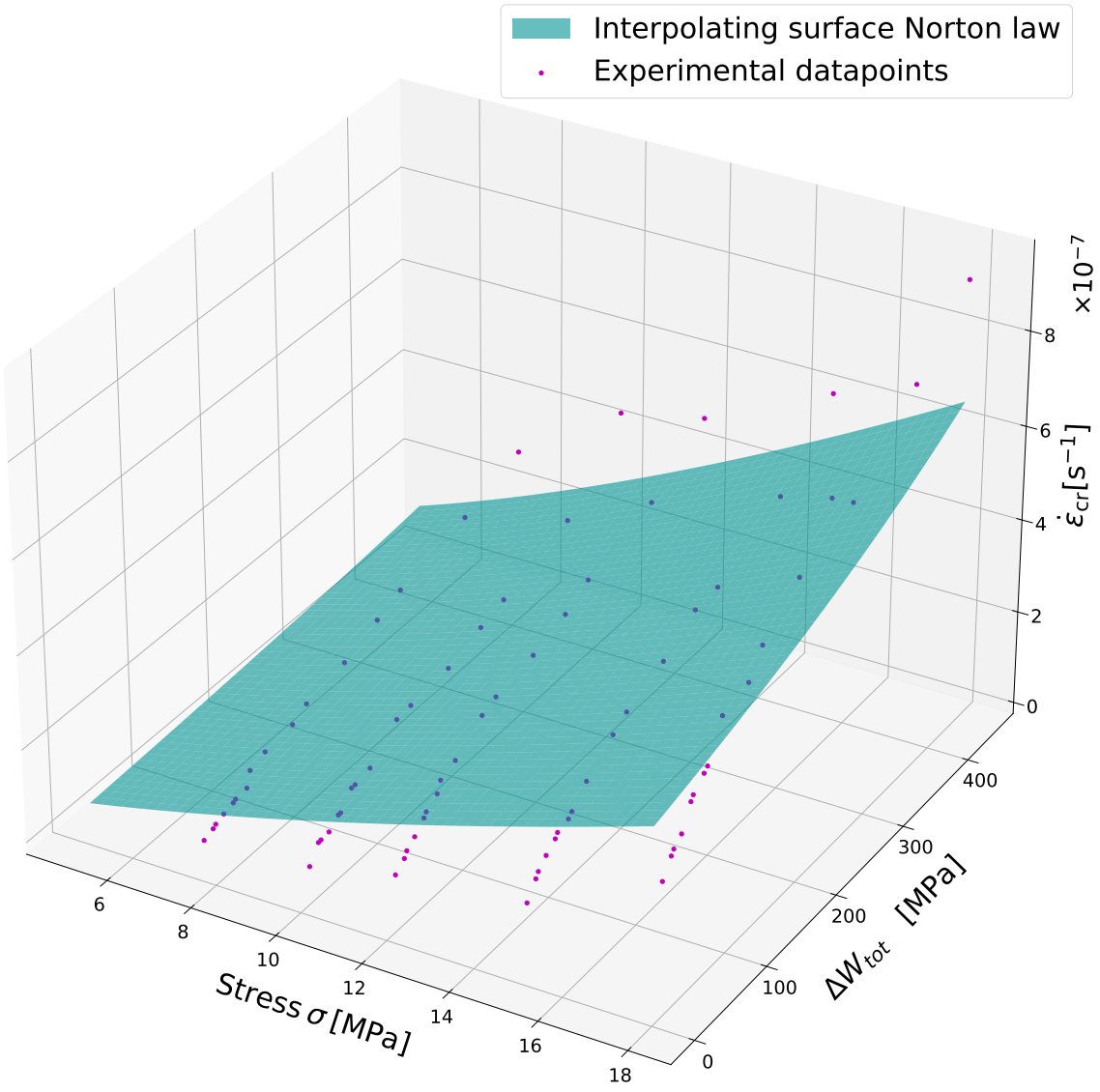

Figure 2.8: Comparison between experimental datapoints and interpolated surface using the NORTON law

The 3D plots provide a general comparison between the experimental points and the results from the optimization procedure. To better assess how closely the interpolated surface aligns with the experimental points, a 2D representation is created. This representation is shown in Figure 2.9 for the hyperbolic-sine law and in Figure 2.10 for the NORTON law. These plots are generated by "slicing" the 3D plots along planes of constant stress and projecting them onto a two-dimensional plane.

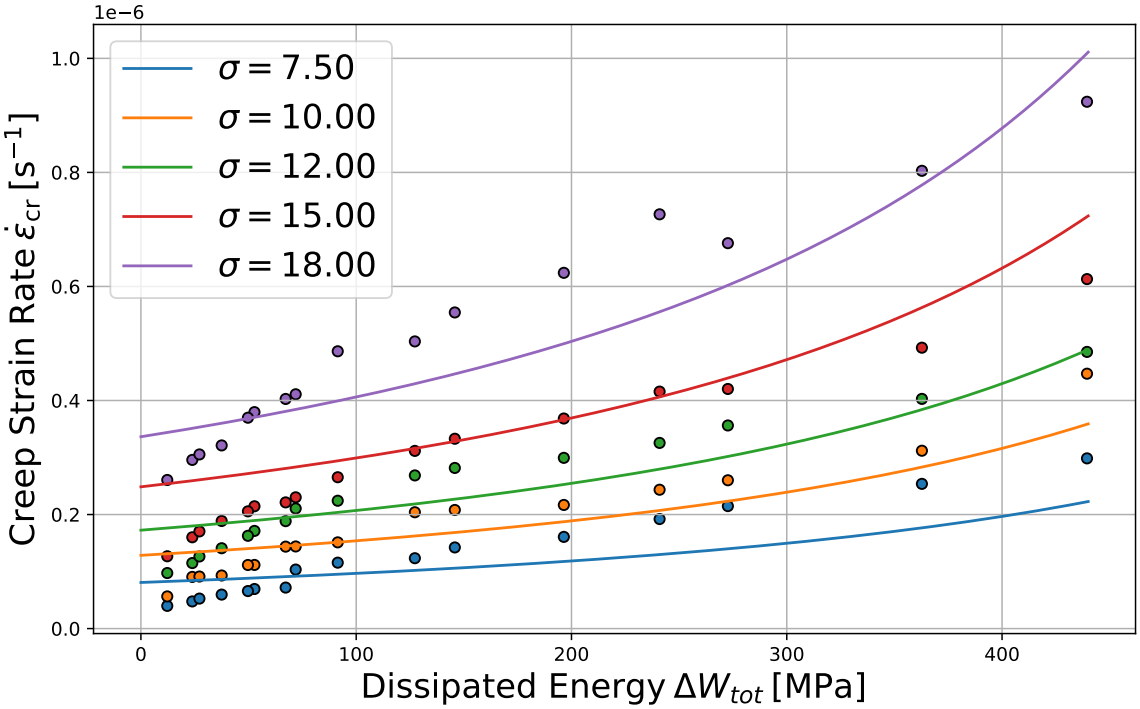

Figure 2.9: Comparison between experimental datapoints and interpolated lines using the hyperbolic-sine law with the free-nlopt parameter set

The hyperbolic-sine law proves to be significantly more effective in capturing the non-linear behavior of the phenomenon than the NORTON law. Nevertheless, for all values of stress σ and dissipated energy ΔW_{tot} below 100 MPa, the curve fit remains imprecise. The optimal outcome of this procedure would be represented by a graph similar to Figure 2.5, where the solid lines exhibit double convexity, initially curving in the direction of the x-axis and then reversing for higher values of dissipated energy. However, the fitting results reported here show only a single convexity.

In the case of the NORTON law, the results are even less satisfactory, as indicated by the higher NRMSE value. For this reason, only the hyperbolic-sine law will be considered in the following sections. Nevertheless, both creep laws prove inadequate for fully describing the high degree of nonlinearity in the problem.

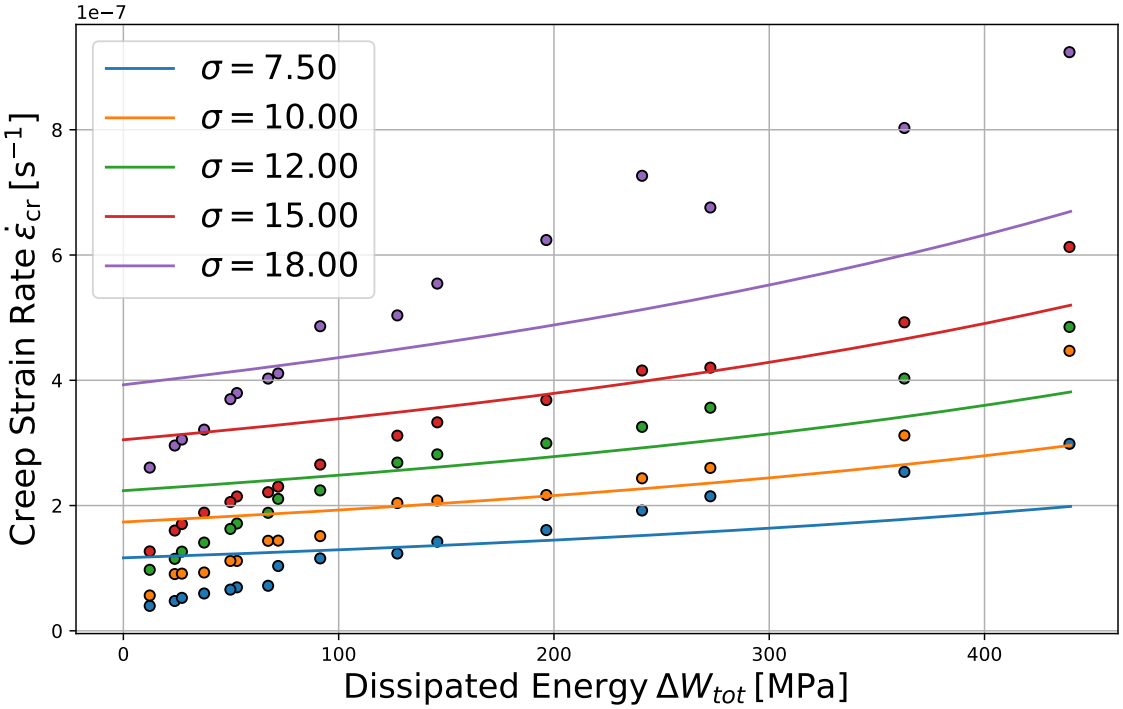

Figure 2.10: Comparison between experimental datapoints and interpolated lines using the NORTON law

Better results are however achieved in the case of the undamaged specimen, the creep strain rate constitutive equation is the hyperbolic-sine one, however no damage is present, it is reported in Equation 2.10,

$$\dot{\varepsilon}_{\mathrm{cr,eq}} = \tilde{C}_1 \left(\sinh\left(C_2 \sigma_{\mathrm{eq}}\right)\right)^{C_3} . \tag{2.10}$$

Results for the two-dimensional plot are represented in Figure 2.11. A low value for the residuals is obtained, r = 0.178. The results obtained on the undamaged specimen are better than the ones for pre-damaged specimens, the used model is adequate in describing simple dead load test but struggles to predict reliable results when mechanical cycling is introduced before the creep test.

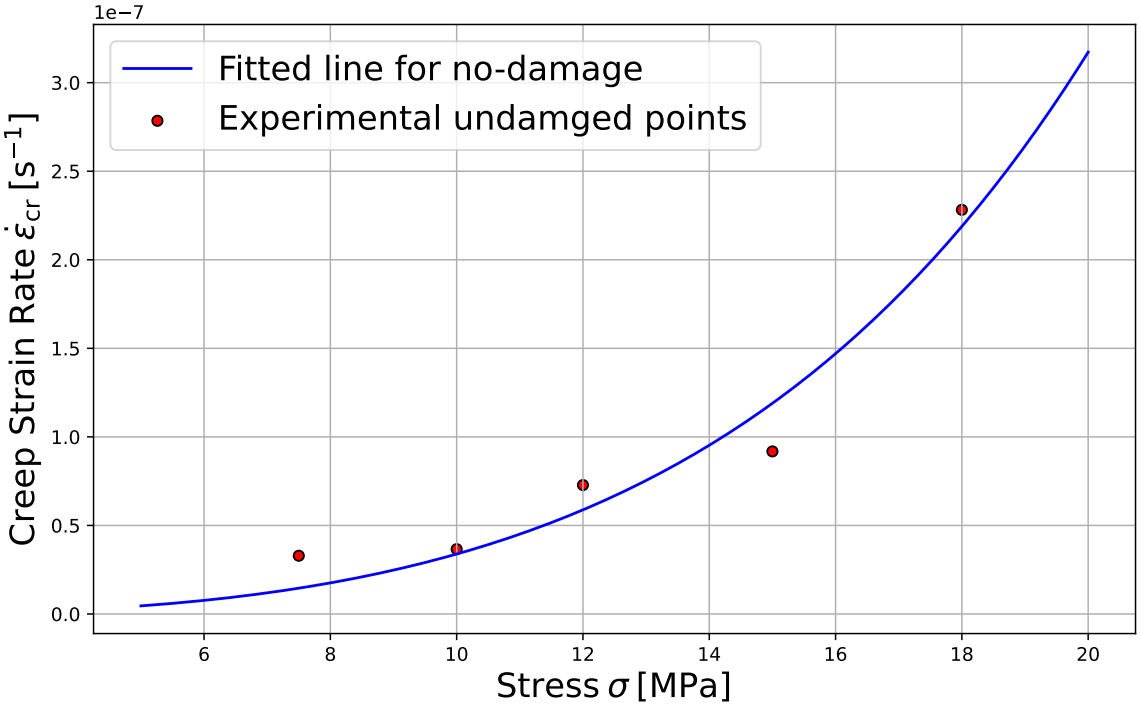

Figure 2.11: Comparison between experimental datapoints and interpolated curve using the hyperbolic-sine law for undamaged specimens

At this point a subsequent optimization is executed; values for $\tilde{C}_1, C_2$ and C_3 are taken as known from the undamaged data fitting. Only C_5 is optimized, results are shown in Table 2.7.

Creep law	$\tilde{C}_1[s^{-1}]$	$C_2[\text{MPa}^{-1}]$	C_3[-]	C_5[MPa]	r [-]
Hyperbolic-sine	2.169×10^{-7}	4.90×10^{-2}	2.77	1208	0.51

Table 2.7: Results for the material constants for hyperbolic-sine creep law, double optimization is executed starting from undamaged specimens

Material parameters are inherent properties of the material and, as such, should not depend on whether the specimen was previously pre-damaged. In this attempt, the favorable results from the undamaged specimen data fitting are considered as known, and only C_5 is optimized. Nevertheless, the results remain unsatisfactory due to the high residual values. When pre-damage is introduced, the hyperbolic-sine law is unable to converge on an adequately close solution, suggesting that more complex models should be considered.

2.3.4. Statistical dispersion of optimized data

In the previous subsection 2.3.3, the optimization is initially performed on the entire dataset, excluding data for undamaged specimens, separately on data from specimens without pre-damage. To better assess the accuracy of the results in relation to their statistical distribution, the optimization procedure is repeated for each experimental line of the pre-damaged specimens. The optimization is performed on each row of the dataset, with all four parameters recalculated each time, and their statistical distribution is analyzed. The hyperbolic-sine law is applied in this process.

Results are shown in the Figure 2.12 via a boxplot. Before plotting the datapoints they are normalized according to Equation 2.11,

$$\text{param}_{\text{normalized}} = \frac{\text{param} - \min_{\text{val}}}{\max_{\text{val}} - \min_{\text{val}}}. \tag{2.11}$$

This normalization formula preserves the statistical distribution of values, ensuring a clear and readable graphical representation. The initial guesses used for every row of the dataset are reported in Table 2.8.

Initial guess	$\tilde{C_1}[s^{-1}]$	$C_2[\text{MPa}^{-1}]$	C_3[-]	C_5[MPa]
Hyperbolic-sine	9.76×10^{-7}	3.2×10^{-2}	3	1200

Table 2.8: Values of the initial guesses for hyperbolic-sine creep law used in the line by line optimization for the boxplot

When working with the hyperbolic-sine law the additional difficulty of numerical overflow must be considered due to the particular shape of the function; the code must be structured in a solid manner to limit this kind of errors as shown in Appendix A.

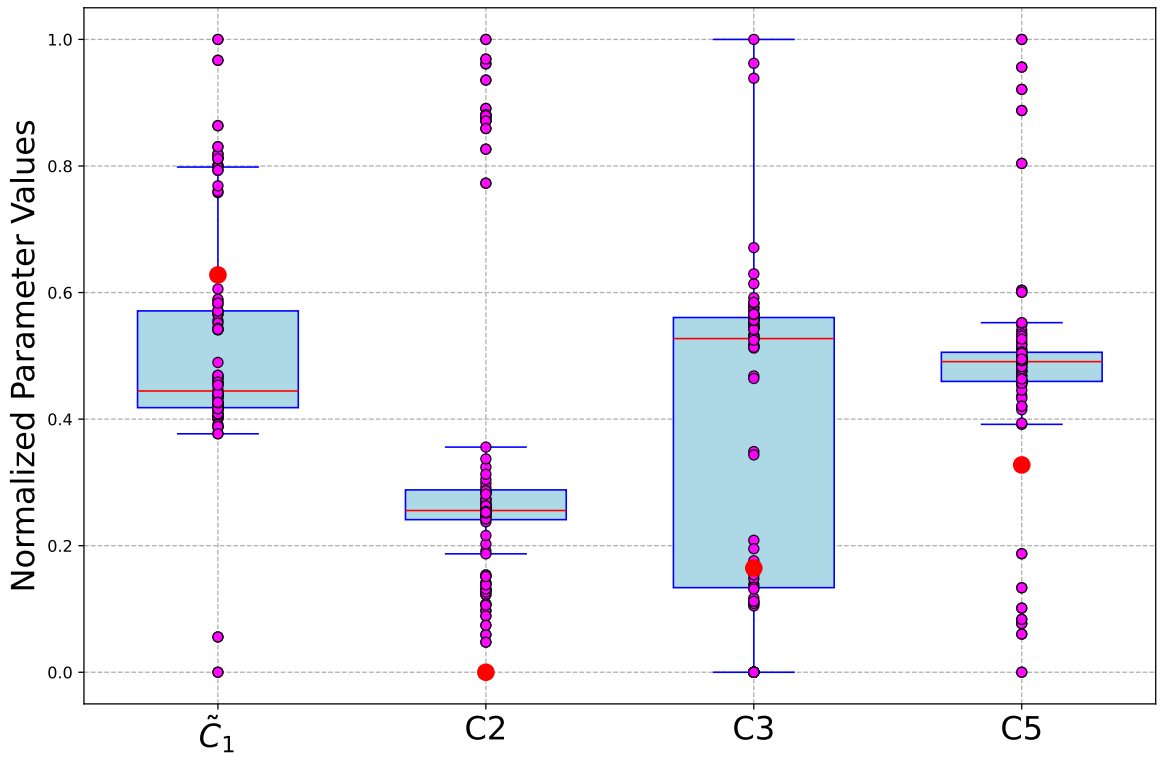

Figure 2.12: Boxplot reporting the results for the optimization problem of the entire set of specimen with pre-damage (red dots) and from the optimization of the single lines (purple dots)

In the picture above, the larger red dots represent the results obtained from the previous "free" optimization, specifically the values in the fourth row of Table 2.5. These values were derived by optimizing the entire set of pre-damaged samples. The smaller purple dots show the results of the optimization performed on each individual entry of the dataset, excluding experiments without pre-damage, resulting in 80 dots per column. The red horizontal line indicates the median values, while the blue boxes represent the interquartile range, limiting the lower 25% and the upper 75% of the data. A graphic visualization is provided in Figure 2.13.

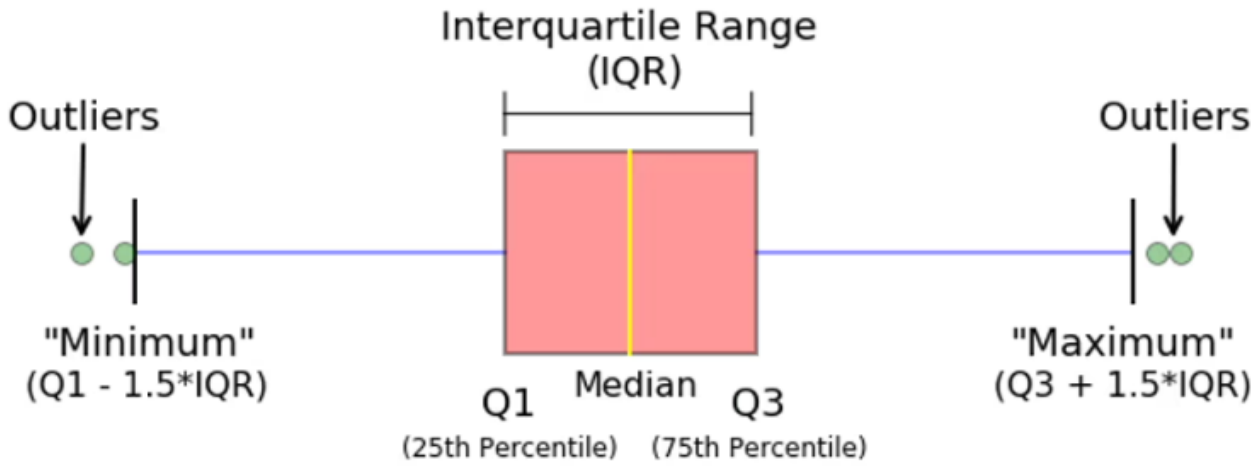

Figure 2.13: Scheme representing the structure of the used box plot [34]

The interquartile range (IQR) is defined as the difference between the third and the first quartile, as in Equation 2.12,

$$\mathrm{IQR} = Q_3 - Q_1 = q_n(0.75) - q_n(0.25), \tag{2.12}$$

here, $q_n(0.75)$ and $q_n(0.25)$ represent the medians of the upper and lower halves of the dataset, respectively. Extending from the boxes, two additional limits can be seen on the left and right in Figure 2.13; these are called whiskers. They are calculated by adding or subtracting 1.5 times the interquartile range from the extreme values of the box. Data points outside the whiskers are referred to as fliers or outliers.

In order to obtain a better result, datapoints outside of the whiskers in Figure 2.12 are removed; the result is recasted in Figure 2.14.

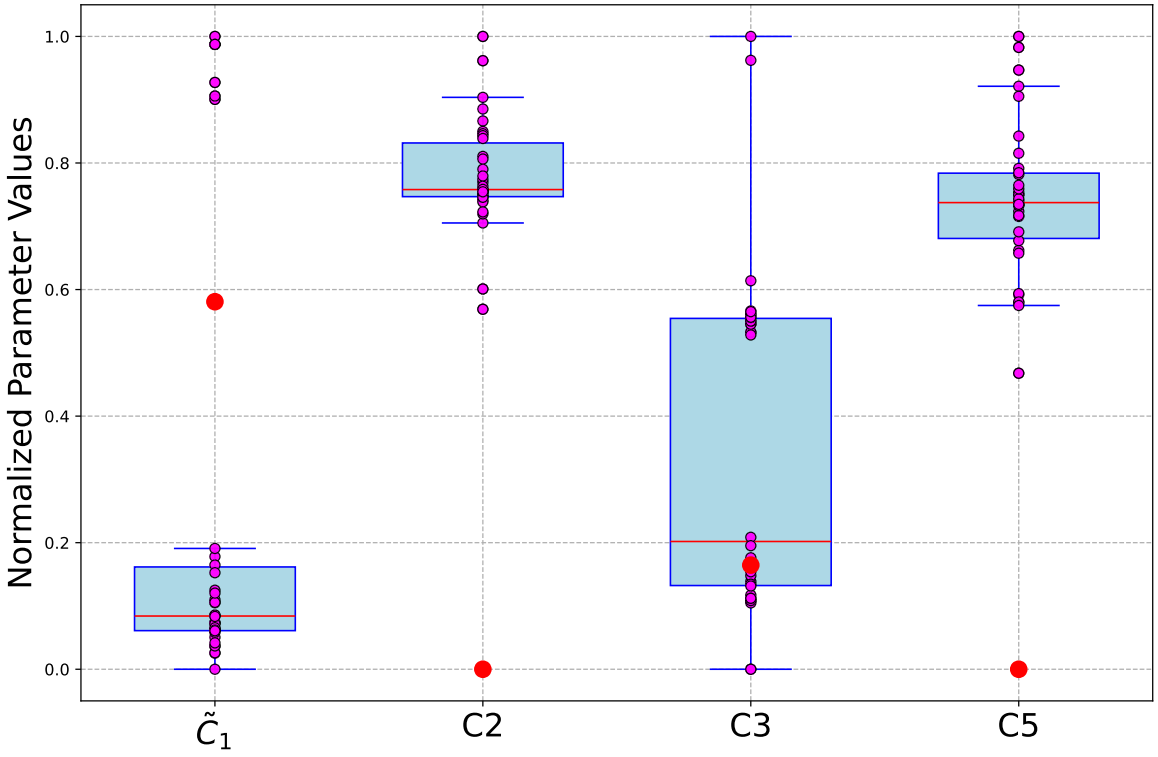

Figure 2.14: Boxplot representing the filtered and normalized set of data

Starting from the 80 values for each material parameter, only 37 survived the filtering procedure, as shown in Table 2.9, drastic changes in the median values take place.

Median taken from:	$\tilde{C}_1[s^{-1}]$	C_2[MPa^{-1}]	C_3[-]	C_5[MPa]	r [-]
original set	1.025×10^{-6}	0.0321	2.884	1196.55	0.450
filtered set	9.913×10^{-7}	0.0320	1.721	1200.43	0.271

Table 2.9: Results for the material constants for the hyperbolic-sine laws, comparison of results between the original median and the filtered median

It can be observed, that the filtering procedure reduces the residual values, resulting in notable changes in the median values of the parameters C_3 and $\tilde{C}_1$. Nevertheless, both in the generation of the boxplot and in the optimizations carried out in subsection 2.3.3, the results show a high dependence on initial guesses and bounds, likely due to the significant nonlinearity of the problem.

To investigate, whether material parameters tend to redistribute based on the pre-cycling undergone by each specimen, the following figure is generated. The data points shown in Figure 2.15 are the same as those in Figure 2.12; however, points extracted from specimens subjected to the same number of cycles are represented in the same color. Points of the same color do not regroup between themselves but are mixed in groups containing different colors, indicating that the number of cycles has little impact on the prediction of material parameters.

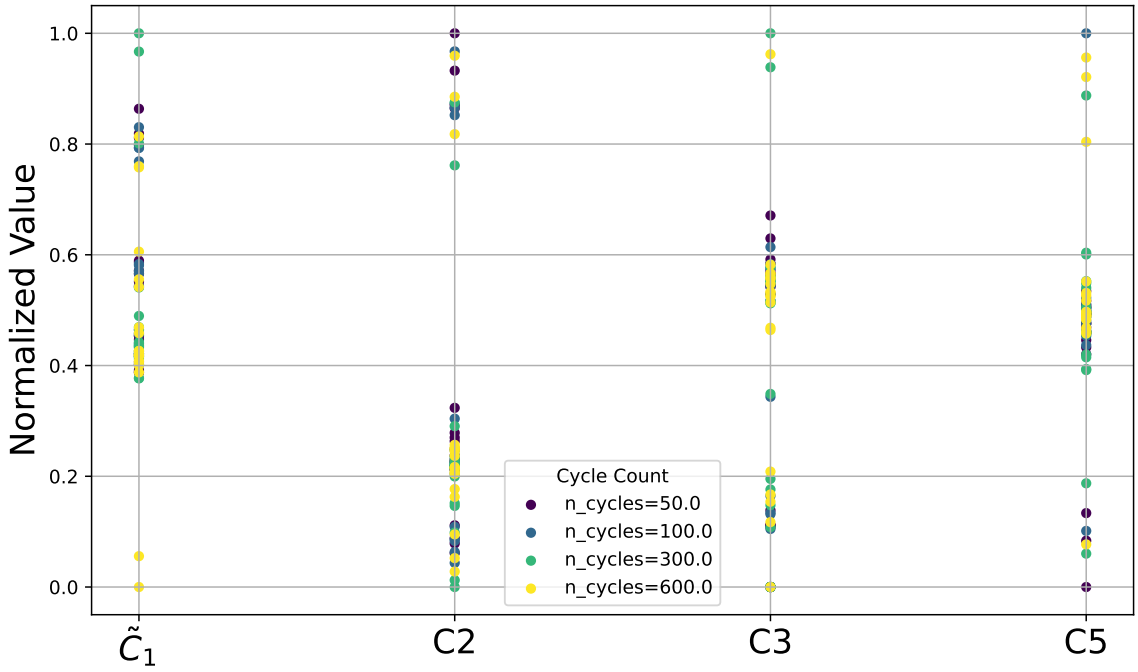

Figure 2.15: Distribution of material parameters based on the number of cycles the corresponding specimen underwent

2.4. Evolution of creep and damage under cycling loading

In the following, a numerical model is implemented using Python programming language to simulate the evolution of relevant quantities such as creep strain, damage, and the hysteresis profile over cycles. Modeling the evolution of these quantities requires solving an ODE or a systems of ODEs.

In this initial approach, a simple elastic-creep model is implemented, thereby neglecting time-independent plasticity phenomena. According to the strain decomposition, stress is computed as shown in Equation 2.13:

$$\varepsilon_{\text{tot}} = \varepsilon_{\text{el}} + \varepsilon_{\text{cr}} \text{ and } \sigma = E\varepsilon_{\text{el}} \Rightarrow \sigma = E(\varepsilon_{\text{tot}} - \varepsilon_{\text{cr}}), \tag{2.13}$$

where E represents the elastic modulus of the material. When simulating a few cycles the values of the elastic modulus can be assumed constant, its value is reported in Table 2.10.

Parameter	Value
Initial elastic modulus (E_0)	37.72 [GPa]

Table 2.10: Initial values of the elastic modulus [42]

2.4.1. Numerical evolution of ODE without damage

Initially, the problem is approached with a simplified assumption that damage does not accumulates ($D = 0$) throughout the entire cycling process, even though only a single cycle is simulated. As a result, substituting Equation 2.13 into Equation 2.10, Equation 2.14 is obtained:

$$\dot{\varepsilon}_{\text{cr}} = \tilde{C}_1 \sinh\left(C_2 E\left(\varepsilon_{\text{tot}}(t) - \varepsilon_{\text{cr}}(t)\right)\right)^{C_3}. \tag{2.14}$$

Starting from the previously obtained array for the total strain, which was used to generate Figure 2.6, the corresponding array is converted into a function using the `scipy.interpolate.interp1d` library from [92]. This function is then used to solve the differential equation in Equation 2.14. The solution of the differential equation is obtained with the `scipy.integrate.solve_ivp` library [93].

After solving the differential equation, the results depicting the evolution of $\varepsilon(t)$ and $\dot{\varepsilon}(t)$ over the course of one cycle are shown in Figure 2.16. Only the first cycle is simulated, material parameters for the hyperbolic-sine law are the ones obtained with the double optimization process and reported in Table 2.7.

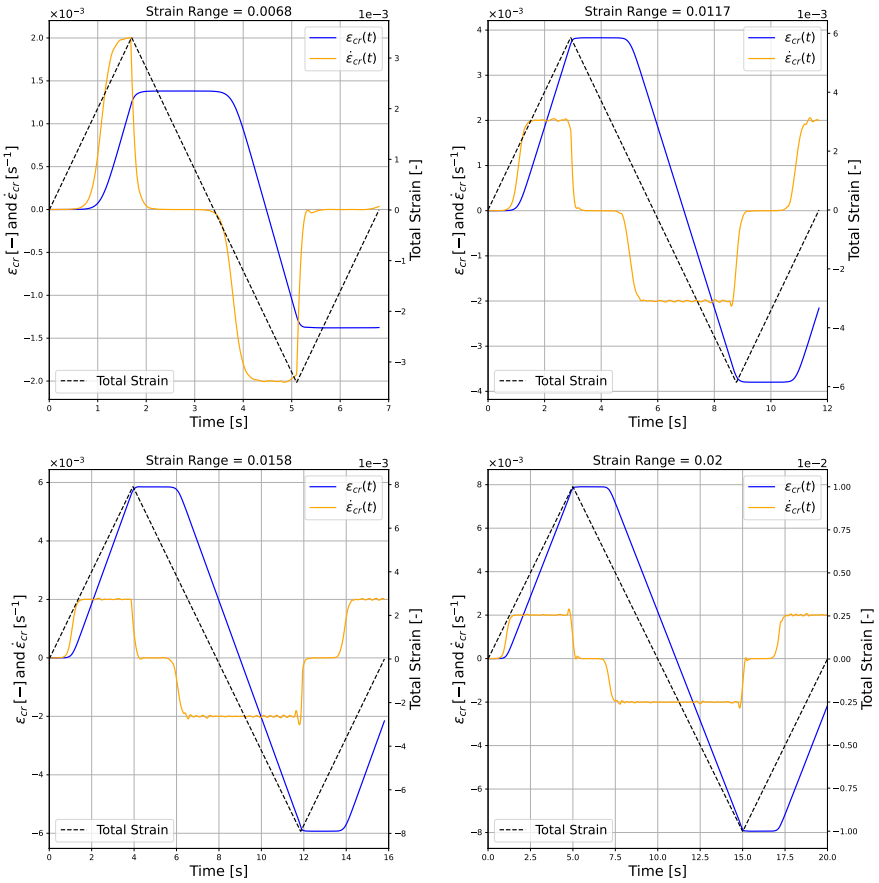

Figure 2.16: Evolution of creep strain and creep strain rate over one cycle for each one of the four types of cycled applied (black dashed lines), no damage is considered

Figure 2.16 demonstrates that, as strain range increases, the maximum creep strain achieved in each cycle also rises, while the maximum value of the creep strain rate is constant. The creep strain rate does not monotonically increase over time; instead, it shows an initial growth during the first upward ramp of the strain profile (see Figure 2.6), then stabilizes momentarily when the strain direction is reversed before dropping. For larger strain ranges, the creep strain cycle is less influenced by the elastic material response, resulting in a more distinct shape. The smaller strain range profile is different in its shape respect to the other three for the influence of the elastic response. The creep strain rate function, meanwhile, behaves as consequence, being of a different shape for the smaller strain range.

2.4.2. Numerical evolution of a system of ODEs with damage

Starting from Equation 2.3 and Equation 2.13, the creep strain rate equation based on the hyperbolic-sine law is reformulated as:

$$\dot{\varepsilon}_{\mathrm{cr}} = \tilde{C}_1 \sinh\left(C_2 \frac{E\left(\varepsilon_{\mathrm{tot}}(t) - \varepsilon_{\mathrm{cr}}(t)\right)}{1-D}\right)^{C_3}. \tag{2.15}$$

Here, the damage D is expressed according to Equation 2.16,

$$D = \int_0^t \frac{1}{C_5} \sigma(t) \dot{\varepsilon}_{\mathrm{cr}}(t)\, d\tau. \tag{2.16}$$

When accounting for damage, Equation 2.15 and Equation 1.37 can be rewritten as the following system of differential equations:

$$\begin{cases} \dot{\varepsilon}_{\mathrm{cr}} = \tilde{C}_1 \sinh\left(C_2 \dfrac{E\left(\varepsilon_{\mathrm{tot}}(t) - \varepsilon_{\mathrm{cr}}(t)\right)}{1-D}\right)^{C_3}, \\ \dot{D} = \dfrac{1}{C_5} E(\varepsilon_{\mathrm{tot}}(t) - \varepsilon_{\mathrm{cr}}(t)) \dot{\varepsilon}_{\mathrm{cr}}(t). \end{cases} \tag{2.17}$$

The system above is then solved and creep strain and creep strain rate are computed throughout the cycle evolution; results are shown in Figure 2.17. Also in this case parameters for the creep law are taken from Table 2.7.

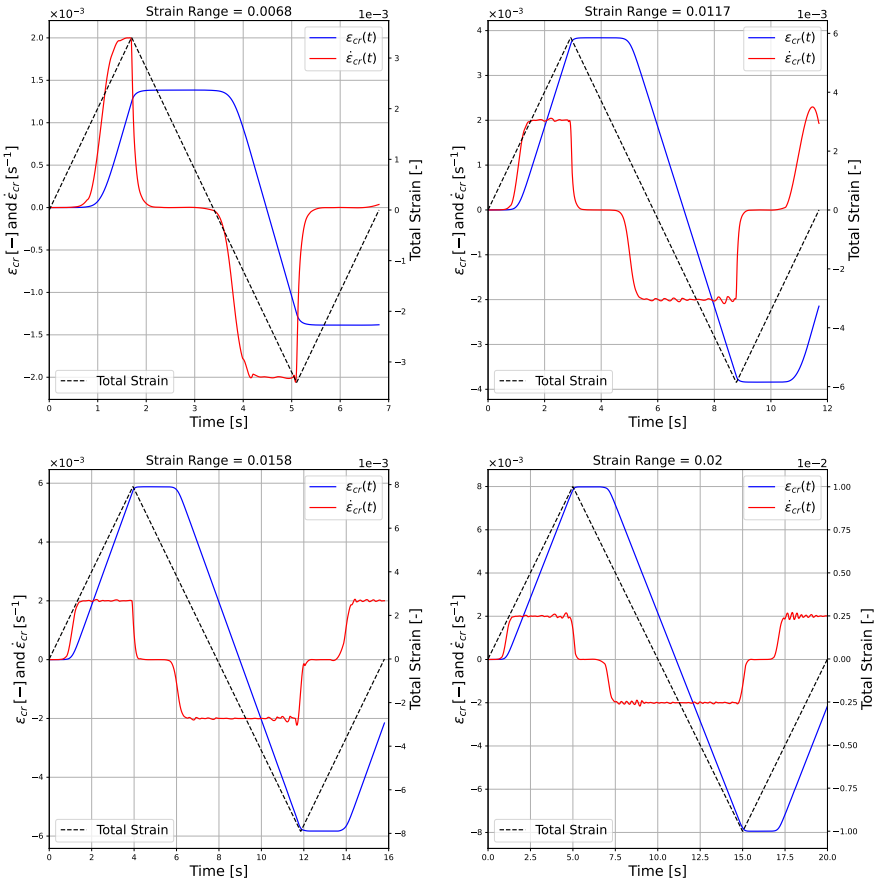

Figure 2.17: Evolution of creep strain and creep strain rate over the first cycle for each one of the four types of strain range (black dashed lines), damage is considered

The outcomes are similar to those previously obtained for the problem without damage. However, greater variability in the first derivative is observed, leading to more pronounced oscillations around the value of two or minus two. These oscillations can be attributed to the increased influence of numerical disturbances due to the interaction between the creep and damage evolution laws. Simulating only the first cycle, the damage evolution has minimal impact on the creep strain and strain rate behavior.

The damage evolution and the applied strain profile for the 0.002 strain range are compared and shown in Figure 2.18.

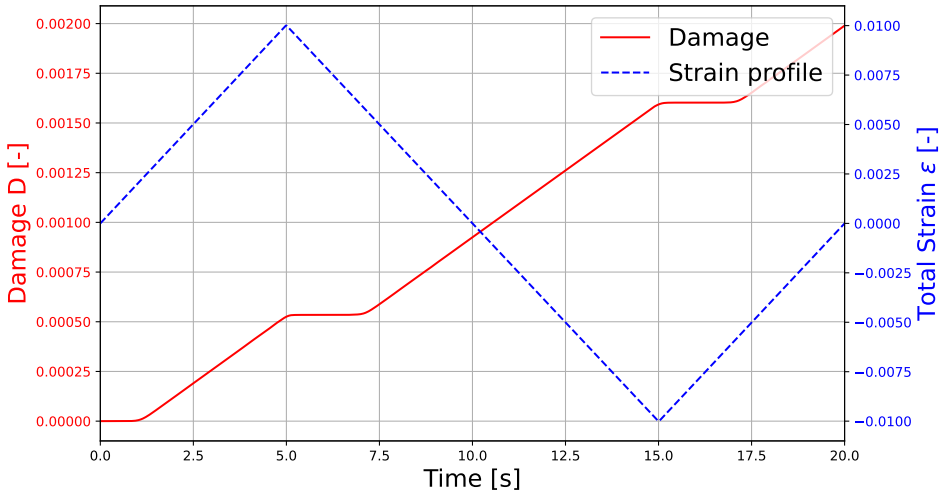

Figure 2.18: Comparison in the evolution of damage and applied strain profile over the first cycle for 0.02 strain range

In Figure 2.18, the strain profile for the 0.02 strain range is compared to the corresponding damage. The red curve represents damage, which steadily increases over time, while the blue dashed curve represents the cyclic strain profile. The damage does not increase immediately when the strain begins to rise; the initial strain is absorbed in the elastic response of the material, creating a delay in the onset of damage. Both the compression and tension phases of the strain cycle contribute to damage accumulation. The damage curve remains flat (indicating zero increase) only briefly after a change in strain direction, due to the material's elastic response. To be more precise, the damage increment is always slightly greater than zero, even in the nearly flat sections of the curve; however, it is extremely small due to the opposing elastic response of the material. Once this response is exhausted, damage continues to increase steadily.

The damage is now computed for all four strain ranges in the first cycle, result is shown in Figure 2.19.

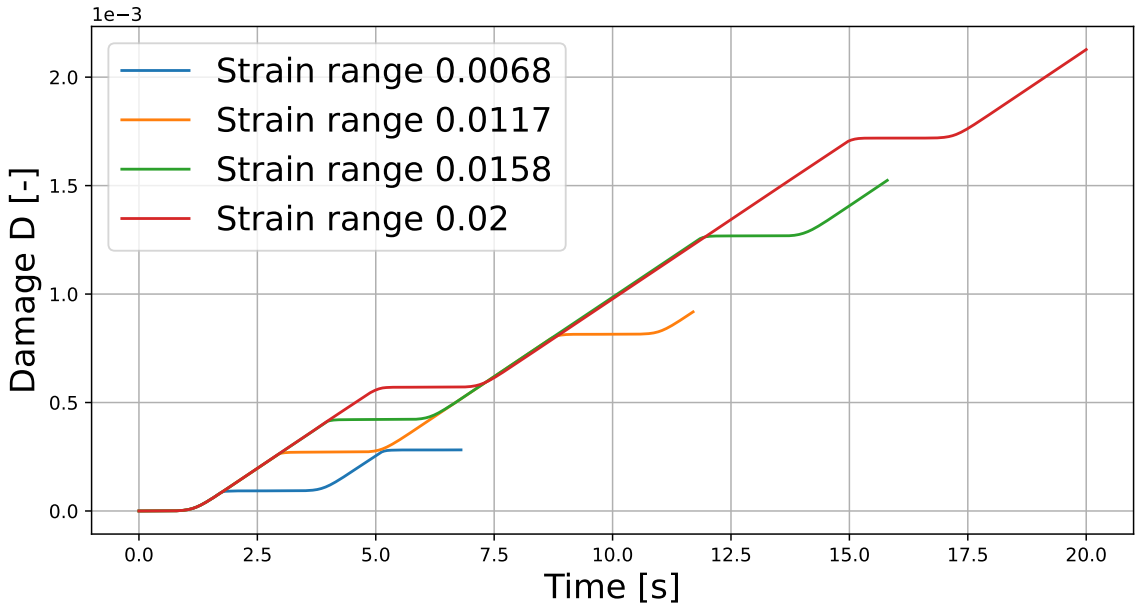

Figure 2.19: Evolution creep induced damage in the first cycle for the four different strain ranges applied

As expected, damage levels are higher for larger strain ranges, and for all four strain ranges, the damage increases in a stepwise manner. The same consideration done for Figure 2.18 are still valid.

2.4.3. Selection of material creep parameters

The damage model introduced in subsection 2.4.2 is further developed to simulate the evolution of typical creep quantities over multiple cycles. As discussed in subsection 2.3.4 and subsection 2.3.3, the optimization procedure does not allow for a decisive identification of a single best set of parameters. In Figure 2.20, the hysteresis loops for the various parameter sets are shown.

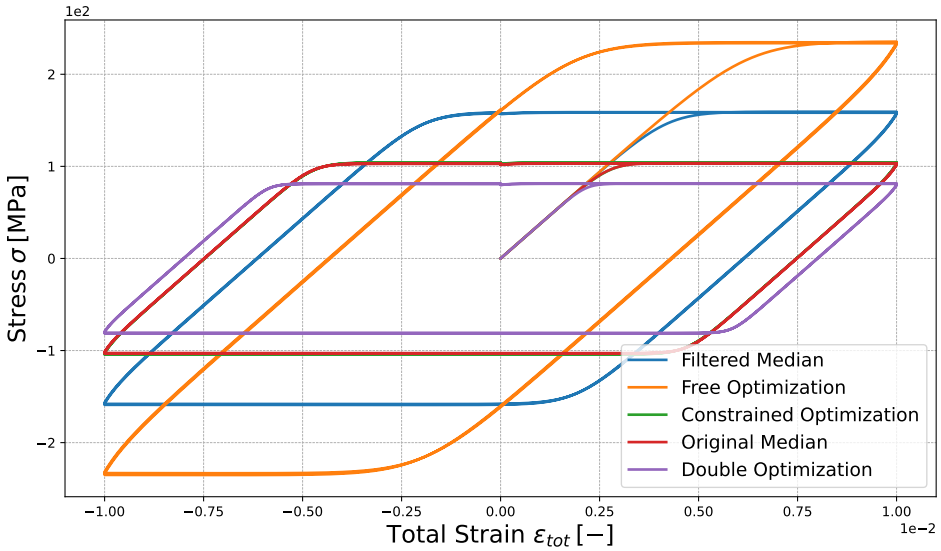

Figure 2.20: Comparison of the hysteresis loop for different sets of identified material parameters

In Figure 2.21 the same comparison is shown regarding the damage evolution.

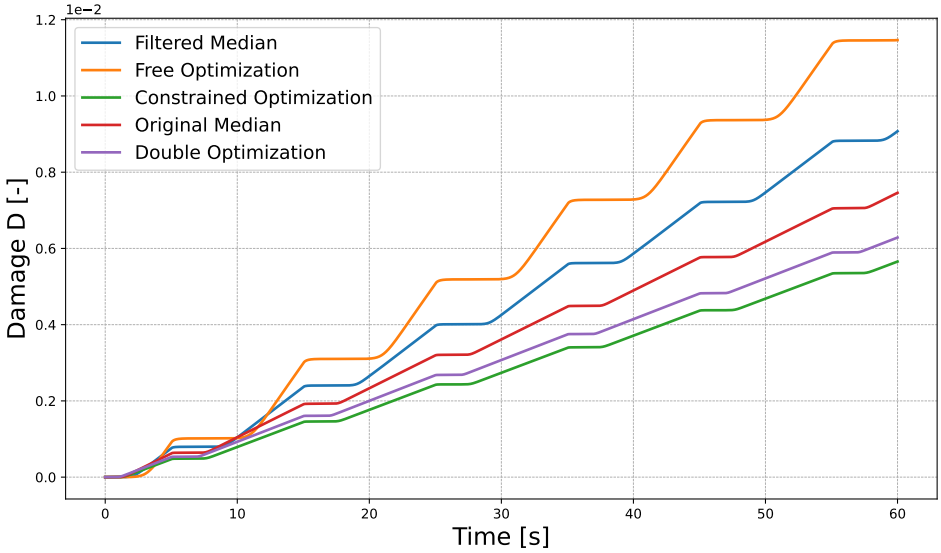

Figure 2.21: Comparison of the damage evolution for different sets of identified material parameters

The results above highlight, that the free optimization and filtered median parameter sets generate hysteresis loops with excessively high predicted stress values. The ultimate tensile strength (UTS) for this material should be around 48 MPa, as noted in [42]. The original median and constrained optimization sets are nearly identical, with the double

optimization set predicting the lowest stress. As the most realistic among the five, the following results are based on this set.

This demonstrates the challenges in predicting the cyclic behavior of the material based solely on a fitting procedure for secondary creep strain rate. The hysteresis loop reflects a portion of the primary creep, which is interrupted after the initial loading phase and then reversed. To improve accuracy, the parameters should be fitted using information from both the primary and secondary creep phases.

In the following, three cycles are simulated for each of the four tested strain ranges, with results shown for creep strain, equivalent creep strain, damage, and the hysteresis loop. Figure 2.22 displays the evolution of creep strain, highlighting the periodic behavior and the influence of strain range on creep strain. Considerations regarding the profile shape are identical to what discussed for Figure 2.16.

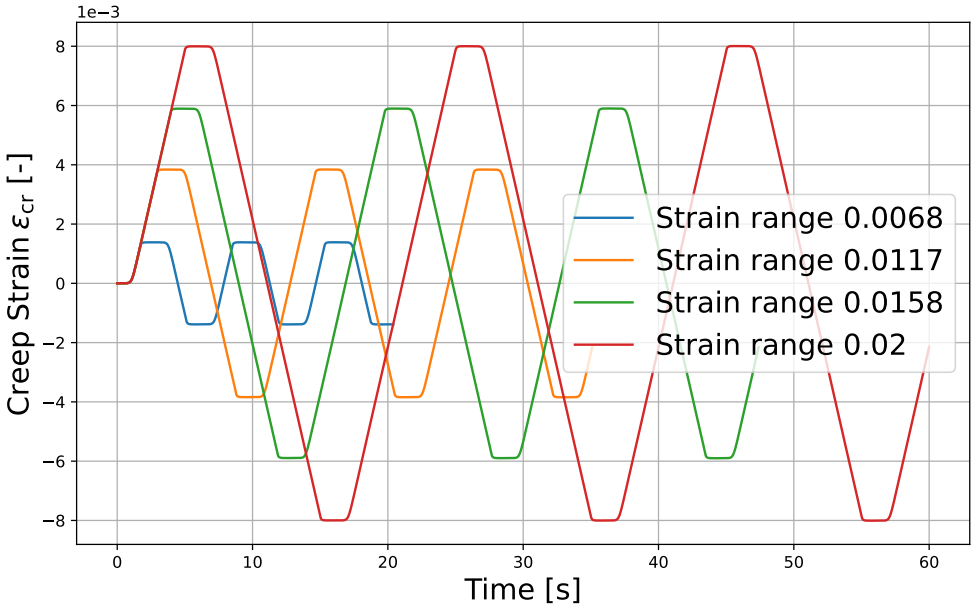

Figure 2.22: Evolution creep strain cycles for the four strain ranges considered and for three cycles

At this point the equivalent creep strain is also computed as in Equation 2.18:

$$\varepsilon_{cr}^{eq} = \sqrt{\frac{2}{3}\boldsymbol{\varepsilon}_{cr} \cdot \cdot \boldsymbol{\varepsilon}_{cr}}. \tag{2.18}$$

Which can be simplified to Equation 2.19 for a 1D test,

$$\varepsilon_{\mathrm{cr}}^{\mathrm{eq}} = \sqrt{\frac{2}{3}}\varepsilon_{\mathrm{cr}} \tag{2.19}$$

The outcome of the simulation is shown in Figure 2.23, as expected the equivalent creep strain is a monotonically increasing function. Also in this case the stepped increasing profile can be explained from considerations on the elastic response of the material and inversion of the strain direction.

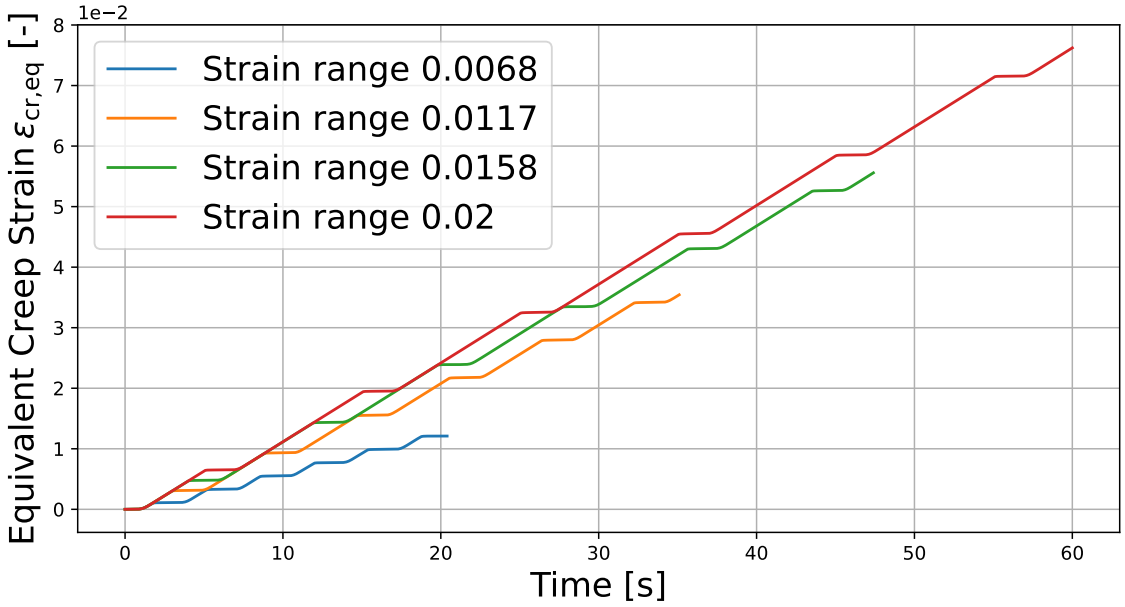

Figure 2.23: Evolution of the equivalent creep strain for the four strain ranges considered and for three cycles

In the following Figure 2.24 the hysteresis loop of the material for the four different strain ranges is represented:

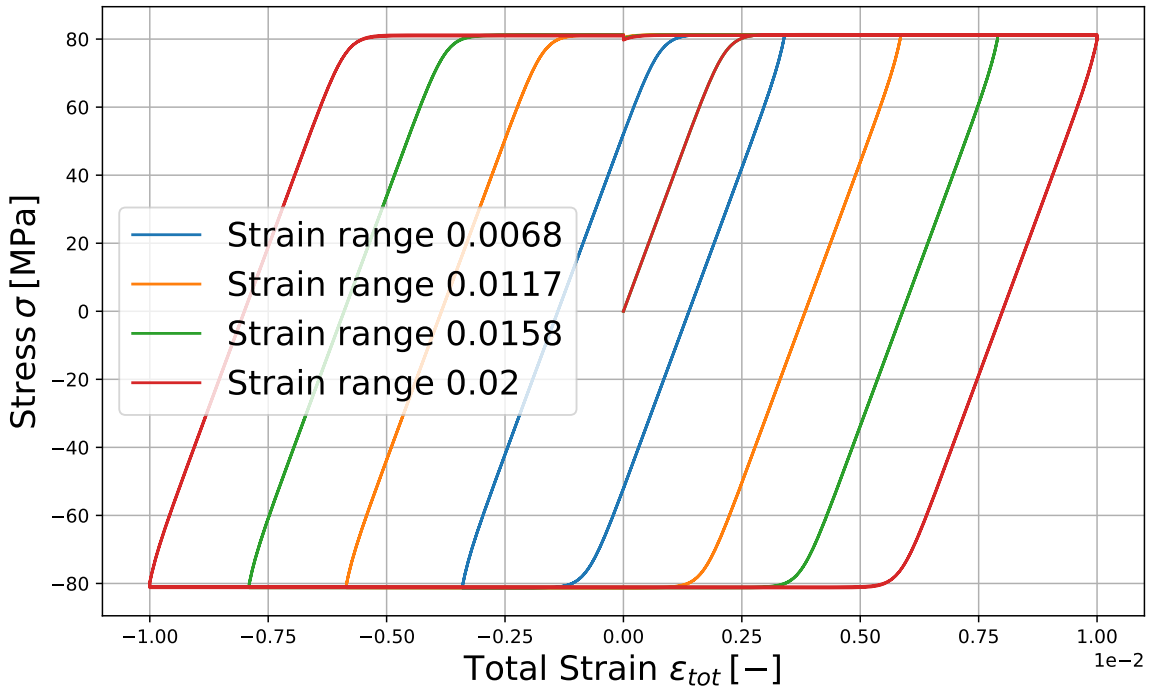

Figure 2.24: Hysteresis loop for the four strain ranges considered and for three cycles

Since now damage is incorporated in the model, more than three cycles can be simulated to verify the effect of the damage on the shape and dimension of the hysteresis loop. However, it must be considered how the mechanical properties degrade over the cycles, in particular the elastic modulus. In Table 2.11 values of the elastic modulus over the cycles are reported from [42].

Cycle n.	Elastic modulus [GPa]
1	37.72
50	30.35
100	23.89
300	21.89
600	19.06

Table 2.11: Values of the elastic modulus of SAC305 after a certain number of pre-damage cycles [42]

Values from the table above are interpolated using both a linear and a double exponential interpolation function [36]. The double exponential law for damage is given by:

$$D = 1 - \left(g_1 e^{-g_2 n_c} + g_3 e^{-g_4 n_c}\right). \tag{2.20}$$

Here, g_n represents constants to be quantified via a curve-fitting procedure, and n_c indicates the number of cycles. Consequently, the effective elastic modulus is determined by Equation 2.21.

$$E = E_0(1 - D). \tag{2.21}$$

Here E_0 stands for the elastic modulus in the first cycle. Results for the constants of Equation 2.20 are shown in Table 2.12.

Parameter	Value [-]
g_1	0.401253
g_3	0.0168212
g_3	0.611774
g_4	0.000298702

Table 2.12: Fitted parameter for the double exponential damage law

The graphical result is represented in Figure 2.25.

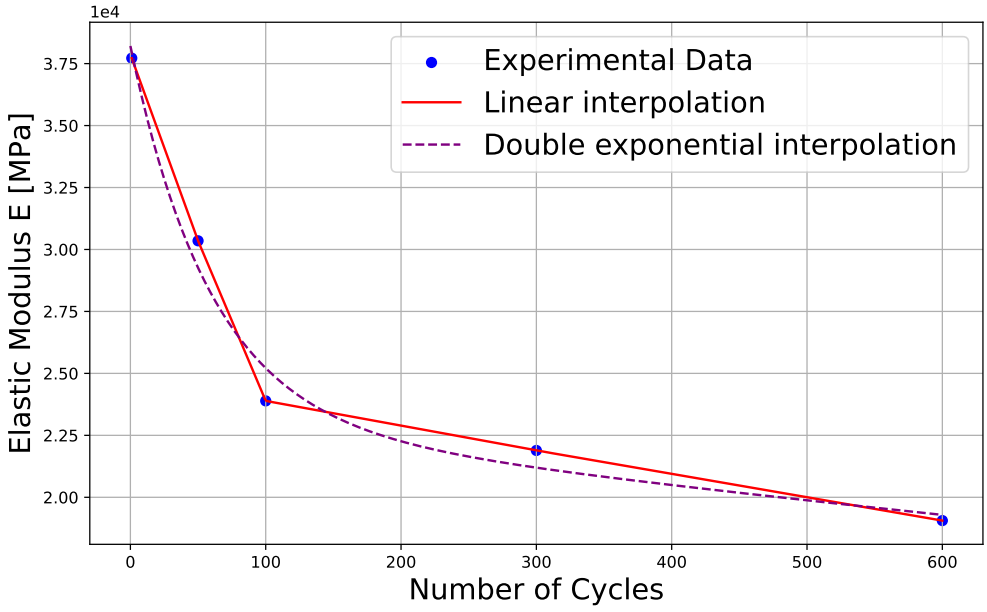

Figure 2.25: Evolution of the effective elastic modulus over the strain controlled cycles

The previous code, used to represent the hysteresis cycle, is then updated in order to determinate the correct value of the elastic modulus from the linear interpolating function. In the subsequent Figure 2.26, 300 cycles for 0.02 strain range are simulated and only one every twenty cycles is represented:

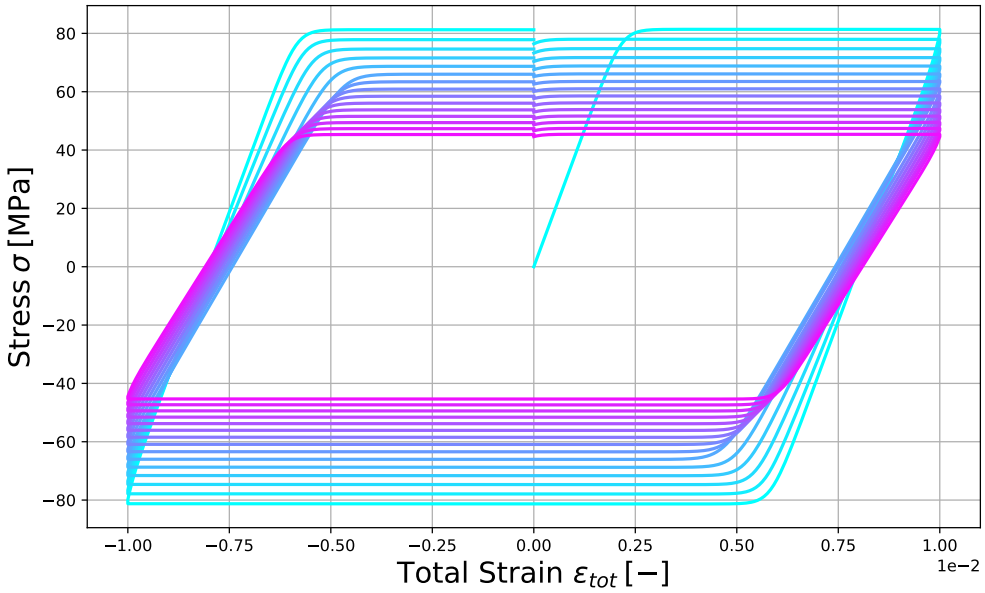

Figure 2.26: Hysteresis loop evolution due to damage, only one cycle every twenty is represented for a total of 300, strain range 0.02

At the same also the damage evolution over time can be plotted.

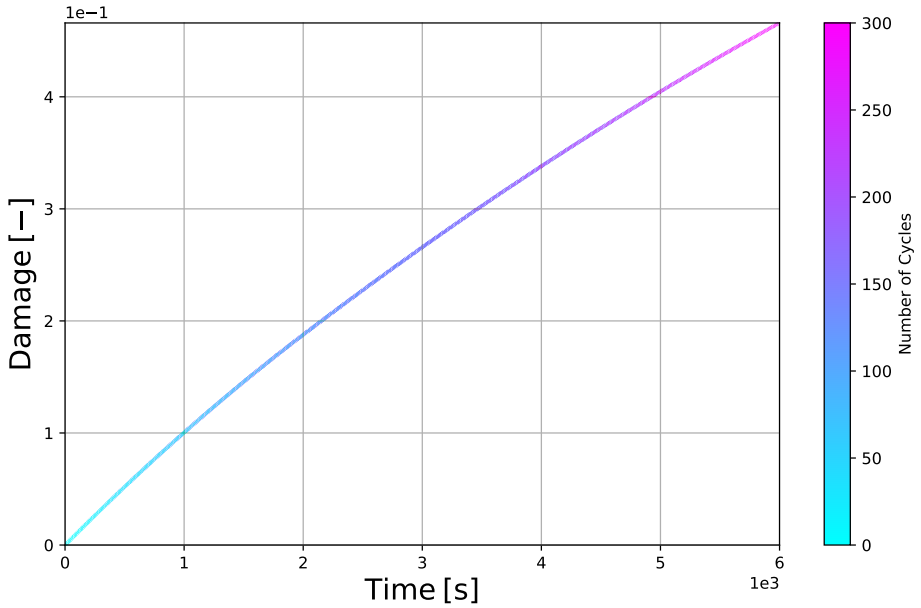

Figure 2.27: Evolution of damage over 300 cycles, strain range 0.02

In Figure 2.26, a gradual reduction in the maximum stress can be observed, indicating a decreased ability of the material to resist the applied deformation. This trend is also reflected in the decreasing slope of the lateral portions of the hysteresis loop. As cycles progress, the material's elastic modulus deteriorates, making it increasingly less stiff, this graphically represented by change in the slope of the horizontal segments. In Figure 2.27, the damage evolution over time is shown, where it is evident that the rate of damage accumulation decreases over time. After three hundred cycles almost half of the material life is consumed.

2.5. Verification of numerical results using finite element software

To verify and validate the results of the numerical Python model, a finite element simulation is conducted, and the outcomes are compared. Finite element simulations are performed in Abaqus using FORTRAN user-defined subroutines, specifically the CREEP and USDFLD subroutines. Information is transferred between these subroutines via two state variables, STATEV(). The subroutine code is provided in the Appendix A. In the CREEP subroutine, damage is assigned to the first state variable, STATEV(1), while the creep strain increment and creep strain rate are computed, with the latter stored in the second state variable, STATEV(2). These state variables are then passed to the USDFLD subroutine, where the stress value is retrieved, and the damage field variable is calculated. Finally, the updated damage value is passed back to the first state variable.

User-defined subroutines are used in this context to extend the built-in functionality of the software by writing custom code, in this case for the evolution of the creep strain and of the damage parameter. Subroutines allow the user to implement their own formulation for damage parameter, failure criteria or for a determined state or field variable.

In the input file, the element type (T2D2) is specified, node coordinates are assigned, and the element is generated. Material parameters are defined with a reference to the user subroutine and an indication of two state variables. Boundary conditions are imposed by applying an encastre at the left node and a displacement profile at the right node. The displacement profile is generated using Python code, saved into a .dat file, and replicates the strain profile for the required number of cycles.

A scheme representing the interaction between the various user-defined implemented subroutines and the Abaqus solver is shown in Figure 2.28

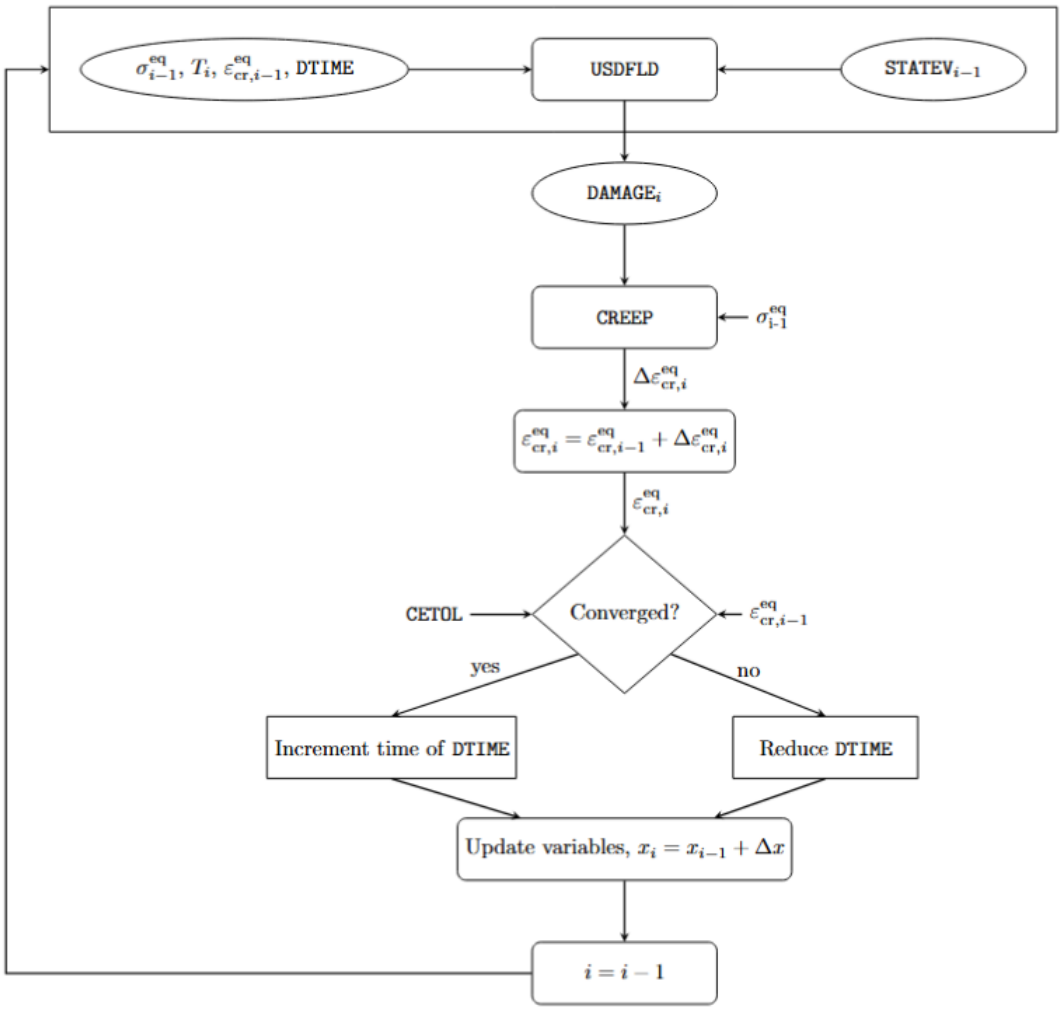

Figure 2.28: Logic flowchart displaying the interaction between CREEP and USDFLD used-defined subroutines and Abaqus solver

In the following Figure 2.29 the previously described numerical model is compared with the results from the FE software simulation.

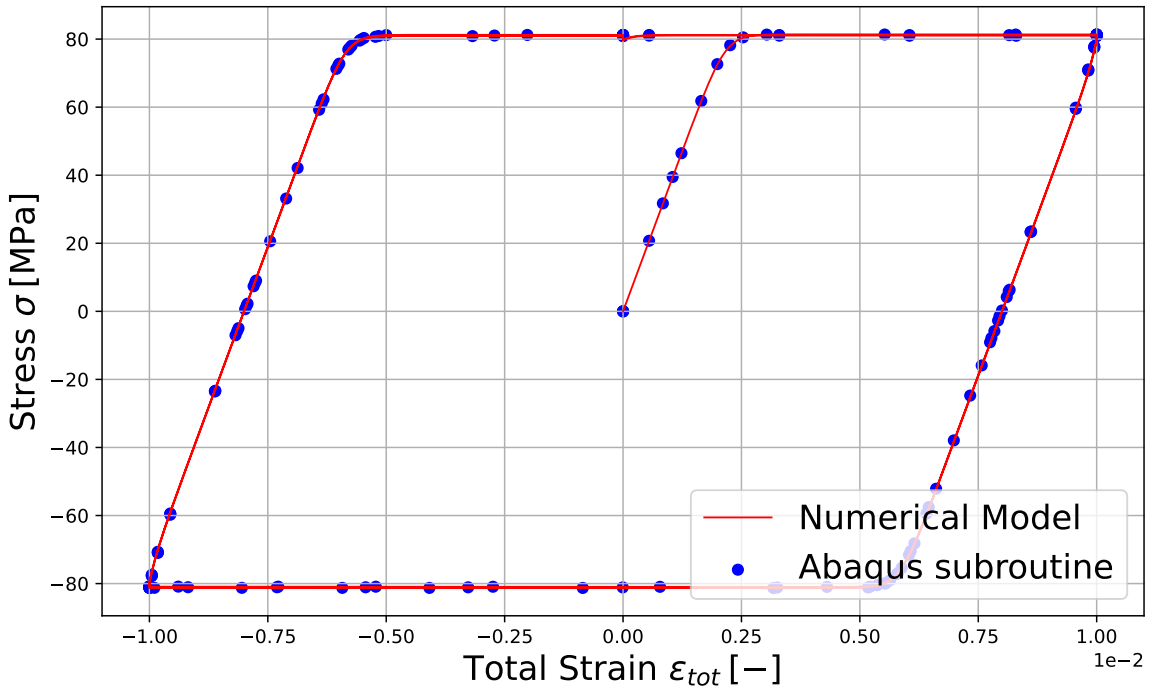

Figure 2.29: Comparison between Python numerical model and FE simulation with subroutines for the hysteresis loop

The same process is also execute for the damage, results shown in Figure 2.30. In both pictures the blue dots represents the results from the FE software while the red solid line the results from the previous Python code.

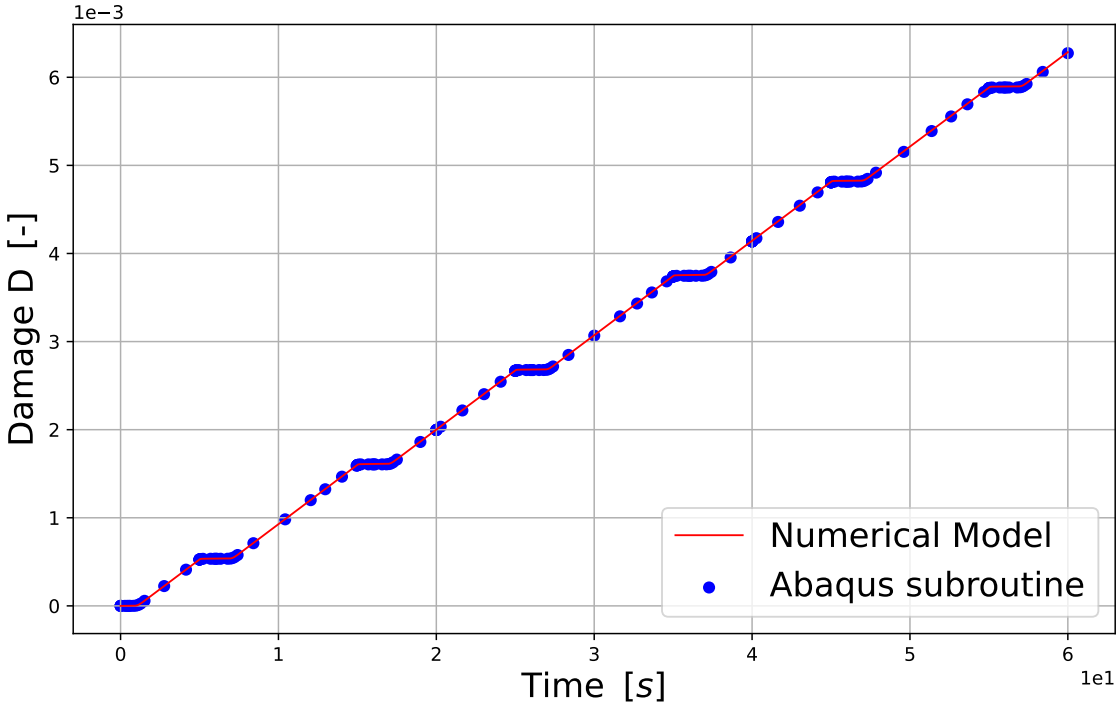

Figure 2.30: Comparison between Python numerical model and FE simulation with subroutines for the damage

3 | Time-independent plasticity

In the previous chapters, a simple elastic-creep model is used. Fitting of creep parameters with respect to the secondary creep strain rate did not allow to realistically reproduce the hysteresis loop. One way to improve the model is to consider an elastic-plastic-creep approach. This chapter explores this possibility.

3.1. Flow and hardening laws for nonlinear plasticity

In this case, a nonlinear isotropic hardening model is implemented. As in any plasticity theory, both yield function and hardening rules must be defined. The yield function $f(\sigma)$ defines the onset of yielding, as follows:

$$f(\sigma) = |\sigma| - \sigma_{\mathrm{y}} \leq 0. \tag{3.1}$$

The plastic strain begins to accumulate only when $f(\sigma) = 0$. The formulation for the plastic strain is given in Equation 3.2,

$$\varepsilon_{\mathrm{pl}} = \left(\frac{\sigma - \sigma_{\mathrm{y}}}{H} \right)^{(1/n)}. \tag{3.2}$$

In this formulation, H is referred to as the hardening modulus, and n as the strain hardening exponent, controlling the rate at which the yield stress increases as plastic strain accumulates. This approach is particularly suitable for capturing the hardening behavior of materials where the transition from elastic to plastic behavior is gradual and nonlinear.

On the other hand, the isotropic hardening rule describes the change in yield stress with the accumulation of plastic strain. A typical nonlinear isotropic hardening rule can be expressed as:

$$\sigma_{\mathrm{y}} = \sigma_{\mathrm{y0}} + H\varepsilon_{\mathrm{pl}}^{n}. \tag{3.3}$$

As plastic strain accumulates, the yield stress increases in a nonlinear manner, making it progressively more difficult for further plastic deformation to occur.

3.2. Plasticity model implementation in Python

In the following section, a Python code is developed to determine material parameters for the creep and plasticity laws, aiming to realistically reproduce the hysteresis loop. In the previous numerical model, material parameters were identified to fit experimental data from secondary creep. Here, the fitting process is adjusted to focus on matching the first ramp of the 20th cycle in the hysteresis loop.

Due to the lack of complete stress-strain data for all hysteresis cycles, data points are collected only for the first ramp of the 20th cycle using the Python library `PIL`. This library enables visualization of an image, and with appropriate calibration, data points on the graph can be selected by mouse click. The coordinates of these points are then printed in the Python console. The selected points are shown in Figure 3.1.

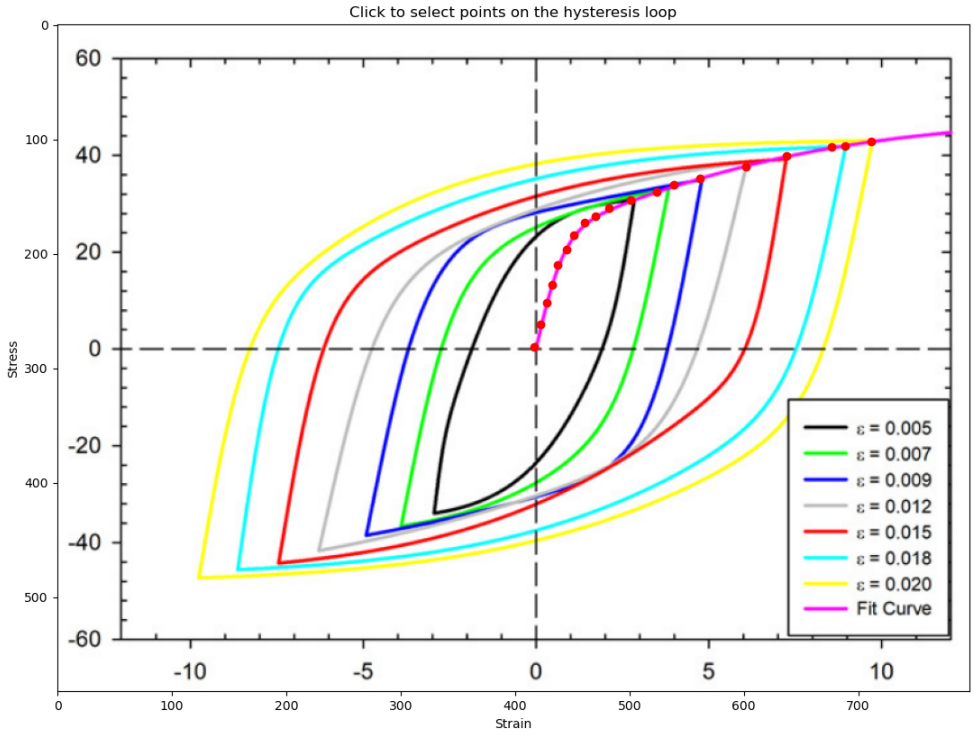

Figure 3.1: Manual selection of stress-strain points on the 20th hysteresis loop, points in red

A numerical model is then developed based on solving the following differential equation, derived by taking the first time derivative of the linear strain decomposition:

$$\dot{\varepsilon} = \dot{\varepsilon}_{\mathrm{el}} + \dot{\varepsilon}_{\mathrm{pl}} + \dot{\varepsilon}_{\mathrm{cr}}. \tag{3.4}$$

During a simple ramp loading, the effect of damage is considered negligible. A creep model based on the hyperbolic-sine formulation, without damage, is implemented alongside the equations for elastic and plastic strain:

$$\dot{\varepsilon}_{\mathrm{el}} = \frac{\dot{\sigma}}{E}, \tag{3.5}$$

$$\dot{\varepsilon}_{\mathrm{pl}} = \frac{1}{nH}\left(\frac{\sigma - \sigma_{\mathrm{y}}}{H}\right)^{\left(\frac{1}{n}-1\right)}, \tag{3.6}$$

$$\dot{\varepsilon}_{\mathrm{cr}} = \tilde{C_1}\sinh(C_2\sigma)^{C_3} \tag{3.7}$$

Equations above are substituted in Equation 3.4:

$$\dot{\varepsilon} = \frac{\dot{\sigma}}{E} + \frac{1}{nH}\left(\frac{\sigma - \sigma_{\mathrm{y}}}{H}\right)^{\frac{1}{n}-1}\dot{\sigma} + \tilde{C1}\sinh(C_2\sigma)^{C_3}. \tag{3.8}$$

The stress time derivative can be expressed as:

$$\dot{\sigma} = \frac{\dot{\varepsilon} - \tilde{C1}\sinh(C_2\sigma)^{C_3}}{\frac{1}{E} + \frac{1}{nH}\left(\frac{\sigma-\sigma_{\mathrm{y}}}{H}\right)^{\frac{1}{n}-1}}. \tag{3.9}$$

The elastic modulus (E) is assumed constant during ramp loading and is set to the value corresponding to the 20th cycle, as determined by the linear interpolation in Figure 2.25. Under the experimental conditions, the total strain rate is specified as 0.002 s^{-1}. It must however be mentioned that with a simple linear regression fit quinte different values for the elastic modulus and the yield stress have been identified, results in Table 3.1 and Figure 3.2. These results are different if compared with what found in [42]. When applying the data shown below a better fit can be achieved, nevertheless in the following results from [42] are used.

Elastic modulus [MPa]	Yield stress [MPa]
26000	17.2

Table 3.1: Identified values of elastic modulus and yield stress from linear fit

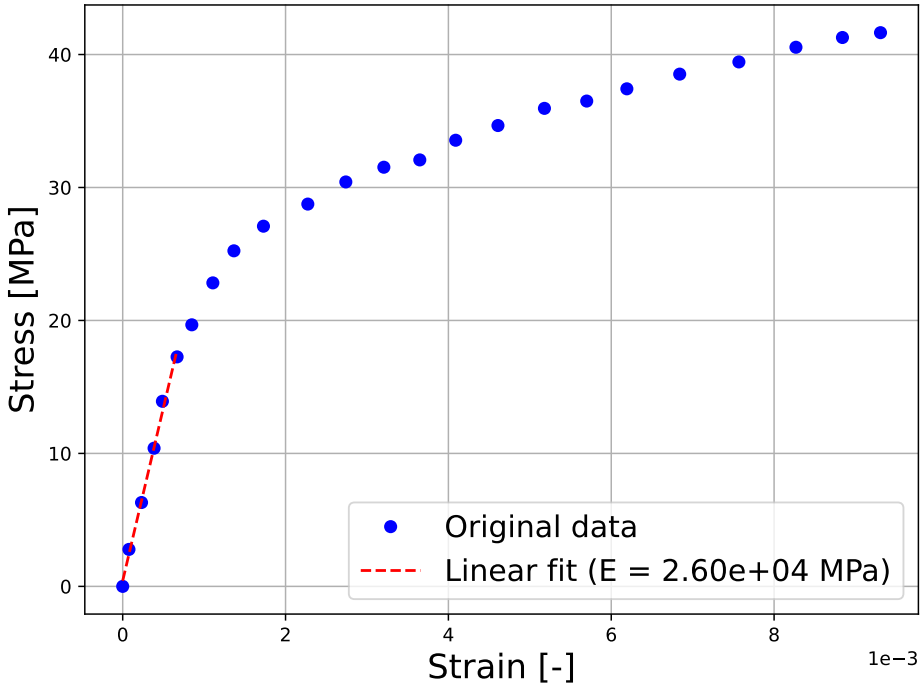

Figure 3.2: Linear fit for the identification of the elastic modulus

A total of six material parameters must be identified: $\tilde{C}_1, C_2$ and C_3 for the creep law, the yield stress σ_y and the plastic strain constants H and n. As before, an objective function is identified with respect to the error in the computed stress:

$$\mathrm{r} = \frac{1}{\frac{1}{N}\sum_{i=1}^{N}\sigma_{i,\mathrm{exp}}}\sqrt{\frac{1}{N}\sum_{i=1}^{N}\left(\sigma_{i,\mathrm{exp}}-\sigma_{i,\mathrm{num}}\right)^2}, \tag{3.10}$$

here, N represents the number of evaluated points, $\sigma_{i,\mathrm{exp}}$ the i-th stress value from graphical acquisition and $\sigma_{i,\mathrm{num}}$ the i-th value from integration of Equation 3.9.

A first optimization is carried out only for n, H and σ_y using values of the creep constants as the one found in the precedent analysis. The the creep parameters are identified using

the latest found values and finally n, H and σ_y are identified again using creep parameter from the step before. Results are shown in Table 3.2 and Figure 3.3.

$\tilde{C}_1[s^{-1}]$	$C_2[\text{MPa}^{-1}]$	C_3[-]	σ_y[MPa]	H [MPa]	n	r [-]
2.180×10^{-6}	4.07×10^{-2}	4.59	15.1	200.84	0.42	0.0425

Table 3.2: Results form the primary creep curve fit

In the figure below the green points represents datapoints acquired from the 20th hysteresis loop, the red solid line is the result of from the elastic-plastic-creep model and the blue one is the results obtained in the previous chapter for the elastic-creep model. The red line is much more capable of representing the real shape of the hysteresis loop by reaching a small number of the residuals computed respect to the stress, however the value of the residuals respect to the secondary creep strain rate is r = 2.877, which represents a significant difference if compared to the values found in precedence.

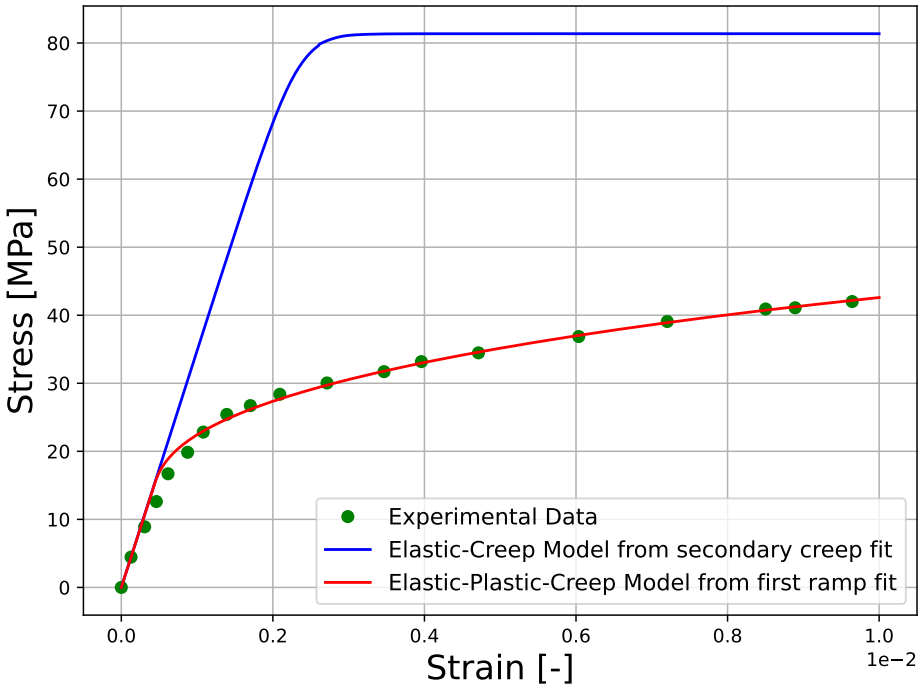

Figure 3.3: Comparison between acquired datapoints, elastic-creep model fitted respect to secondary creep strain rate and elastic-plastic-creep model fitted respect to datapoints

Results obtained with is procedure demonstrate their validity in predicting the first loading ramp of the material, however results for the secondary creep are not satisfactory.

To correctly reproduce cyclic loading both isotropic and kinematic should be considered, in this case only the stabilized 20th cycles is available. More complex viscoplastic models like the ANAND model [107] or the PERZYNA and CHABOCHE models [81] should be implemented, however more data are required.

4 | Solder ball cyclic shear loading

In this chapter, the creep behavior for solder balls in ball grid array (BGA) under shear cycling loading is investigated. An overview of the BGA structure and its key components is provided, followed by a discussion on temperature cycling-induced failure mechanisms. A finite element (FE) solder ball model is simulated, a small BGA structure is modeled using Abaqus, a submodel created to study the effects of cycling shear loading on an individual solder ball. The used creep material parameters are the ones identified in subsection 2.4.3.

4.1. Ball grid array structure

The ball grid array (BGA) is a widely used packaging type in surface mount technology (SMT), particularly valued for its high-density connections and effective thermal management. In a typical BGA assembly, three primary components are involved: the microchip (or integrated circuit) positioned on the top layer, the printed circuit board (PCB) as the bottom substrate, and the array of solder balls sandwiched in between. Each component plays a distinct role in the functionality and reliability of the package.

The solder balls act as both electrical and mechanical connectors, bridging the microchip and the PCB by providing conductive pathways for electrical signals and a physical bond that maintains the structural integrity of the assembly. This dual role places considerable importance on the reliability of the solder joints, as any failure in these connections can lead to operational malfunctions or a complete breakdown of the electronic device. Therefore, understanding and enhancing the durability of these solder joints, particularly under stress conditions such as temperature cycling, is essential.

A simplified structural representation of a BGA microchip on a substrate, detailing its critical elements, is illustrated in Figure 4.1. A flip-chip configuration is presented, essentially the microchip is mounted upside down on the circuit board.

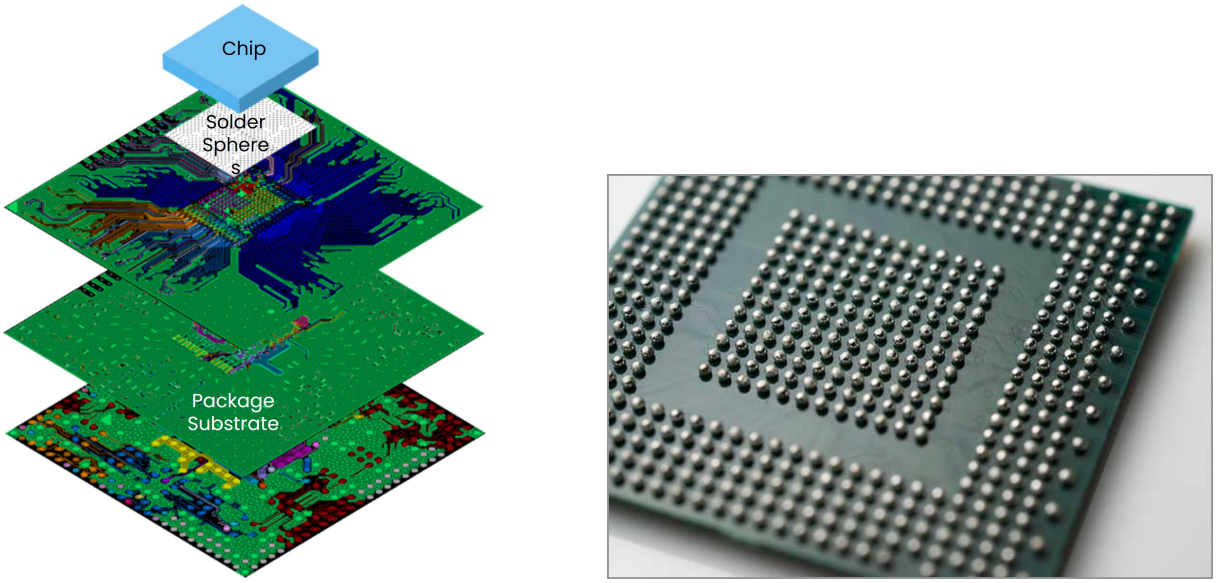

(a) Flip-chip on substrate [39] (b) Solder balls array [41]

Figure 4.1: Packaging structure and component together with ball grid array detail

At the top of the previous image, a cyan-colored chip is visible. Directly beneath it is a set of solder balls, which provide both mechanical support and electrical connection between the chip and the green-colored substrate

To provide a clearer understanding of the studied problem, Figure 4.2 presents a cross-sectional view.

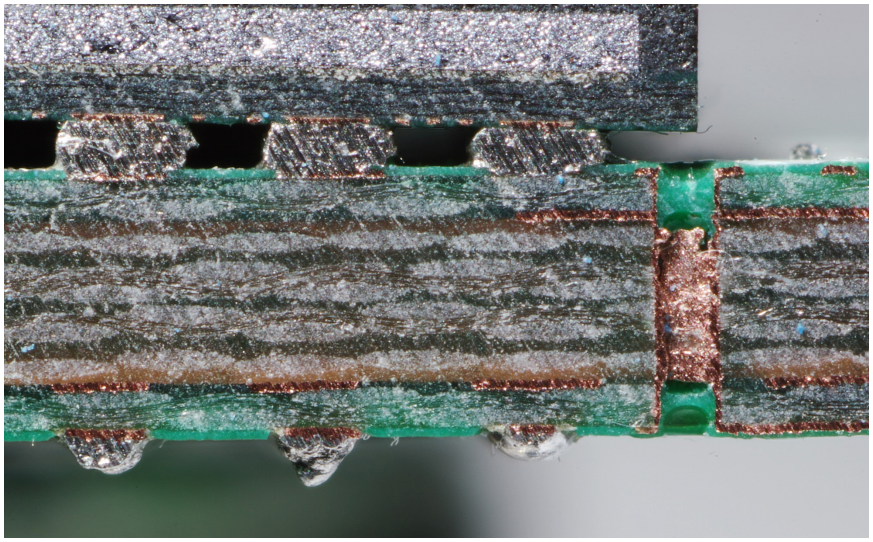

Figure 4.2: Section of a BGA [104]

From top to bottom in Figure 4.2, we can observe the microchip in shades of black and

gray, followed by the deformed solder balls, which serve as the connection points, and finally, the greenish layer representing the PCB at the bottom.

4.2. Thermal modeling of temperature cycling effects on solder balls

During their operational life, BGAs experience temperature cycles. Due to differences in the elastic modulus and thermal expansion coefficients among the BGA components, these cycles impose deformations on the solder joints. As a result, solder joints are subjected to cyclic shearing forces, which degrade their fatigue life and contribute to eventual joint failure.

The resulting cyclic deformation within the joint induces self-stress states that ultimately lead the solder material to fail under fatigue conditions.

In Figure 4.3, an illustration is provided showing how cracks typically develop at the interface.

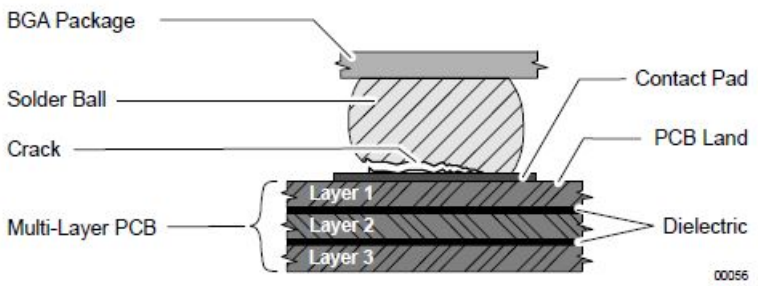

Figure 4.3: Crack development at the solder ball- PCB junction [41]

In [88], microstructural changes that lead to crack initiation in SAC305 solder balls are examined. SAC305 solder tends to fail due to intergranular cracking, which results from thermomechanical fatigue.

Solder balls are systematically arranged on the PCB, forming a structured grid, as depicted in Figure 4.1. This configuration provides a stable connection between the microchip and PCB, distributing electrical and mechanical loads evenly across the array.

The arrangement in the image above reveals that the solder balls are positioned in a square formation, leading to non-uniform stress distribution due to thermal expansion differences between the microchip and PCB. In Figure 4.4, an overhead view is shown with a magnified section on the left. The blue and red lines indicate the boundaries the

chip array reaches under varying temperatures: the blue line represents the contracted dimensions at low temperatures, while the red line marks the expanded dimensions at higher temperatures. This thermal expansion mismatch causes some solder balls to experience greater stress, particularly those located at the corners and edges. Experiments from [35] confirm how solder at the corners are the first to experience failure.

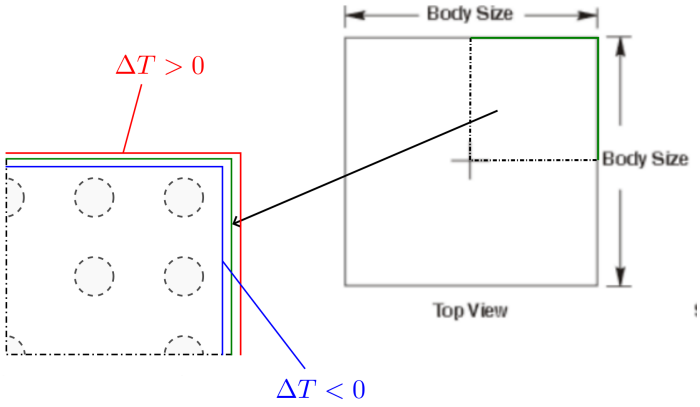

Figure 4.4: PCB structure form above, zoomed in 1/4 of the plate to highlight the expansion and contraction of the chip array

As a consequence, the solder balls positioned at the corners experience the highest stress, as these locations exhibit the greatest induced displacement differences. This causes the corner solder balls to be subjected to alternating shear stress. Specifically, the maximum stress is concentrated along the diagonal of the plate, bisecting the solder ball. Additionally, [88] focused on these "corner joints" in their analysis, as they are the most susceptible to thermomechanical fatigue.

4.3. Finite element simulation of temperature shock test

In this section, from the knowledge of the typical temperature profile for microelectronic components temperature shock testing, the displacements in the global model of a BGA are computed. The displacement fields at the microchip-solder and PCB-solder interfaces are then extracted and, using the finite element software Abaqus, applied on the submodel, cyclic shear loading is simulated.

4.3.1. Global model

In the global model, a 5x5 ball grid array is considered, as represented in Figure 4.5. This model does not represent any existing microchip package, it is used as realistic example.

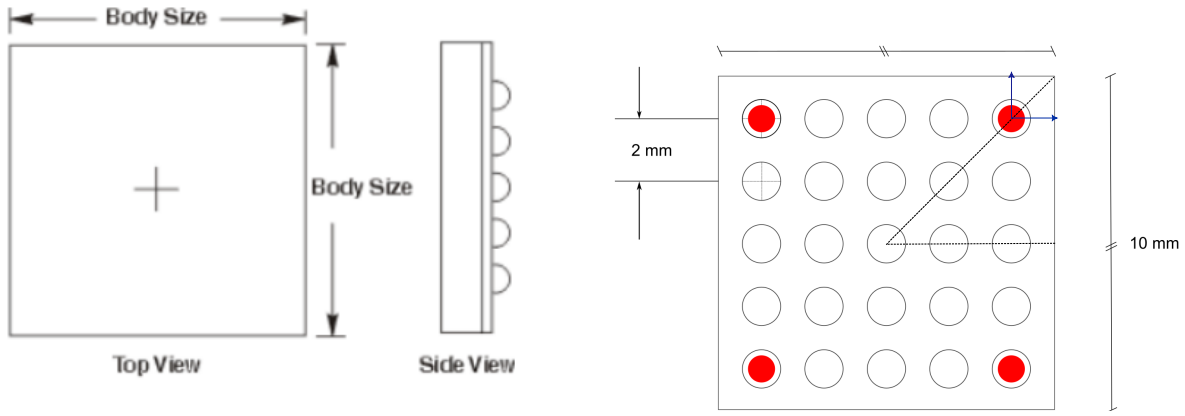

(a) Microchip dimension (b) Ball pitch metric

Figure 4.5: Ball pitch and body size representation for the global model, for (b) critical solder balls in red, one-eight of the board is actually simulated

The red dots indicate the solder balls subjected to the higher level of applied displacement, only these are simulated in the submodel. The black lines highlight one-eight of the board, taking advantage of the geometrical symmetries only this part is simulated in the global model. The two blue arrows indicate the horizontal and vertical thermal displacement field for the solder joint, resulting in a total displacement along the board diagonal. Values for the body size and ball pitch dimensions are provided in Table 4.1.

Body size	Ball pitch
10 mm	2 mm

Table 4.1: Dimensions for the ball pitch and the body size of the microchip

The global model comprises three main components: the solder balls, the PCB, and the chip frame. Their respective properties are listed in Table 4.2.

Material	E [GPa]	ν [-]	α [1/K]
Solder	37.72	0.305	24 $\times 10^{-6}$
PCB	24	0.177	18 $\times 10^{-6}$
Chip frame	130	0.270	3 $\times 10^{-6}$

Table 4.2: Material properties for the solder ball, the PCB and the chip frame

The dimensions for the solder balls are represented in Figure 4.6.

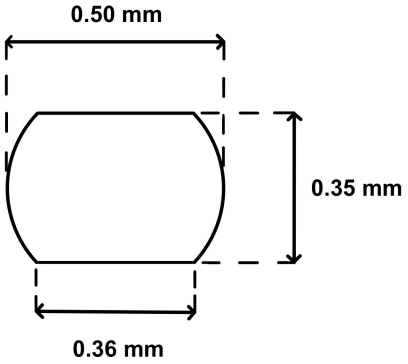

Figure 4.6: Solder ball profile with associated dimensions

An eight of the global model is shown in Figure 4.7 from above together with the global model isometric view. The PCB is depicted in white at the bottom, with solder balls marked in red and the microchip frame highlighted in green.

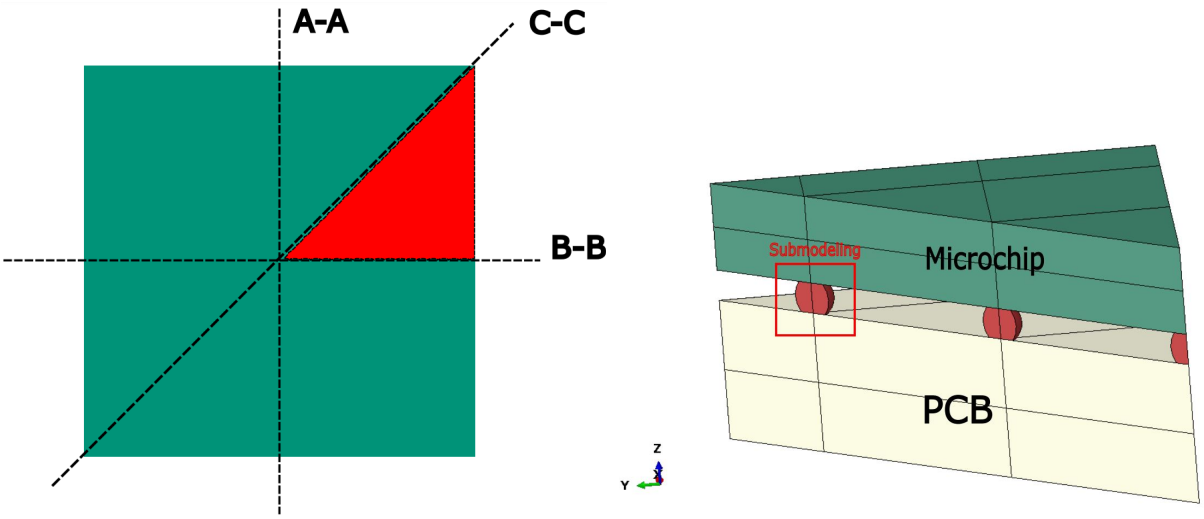

(a) Global model symmetry BC (b) Global model isometric view

Figure 4.7: Global model form above with its symmetry planes (a) and with isometric view (b), submodeling solder ball highlighted

Taking advantages of the packaging symmetries it is possible to reduce the computational effort by simulating only an eight of the global model. In Figure 4.7 a view of the packaging from above is given, the planes of symmetries are A-A, B-B and C-C, displacement orthogonal to the symmetry planes is imposed to be zero. The simulated part of the global model is indicated in red.

Based on the applied temperature profile shown in Figure 4.8, the maximum and minimum temperatures are known, allowing for the simulation of displacement in the global model.

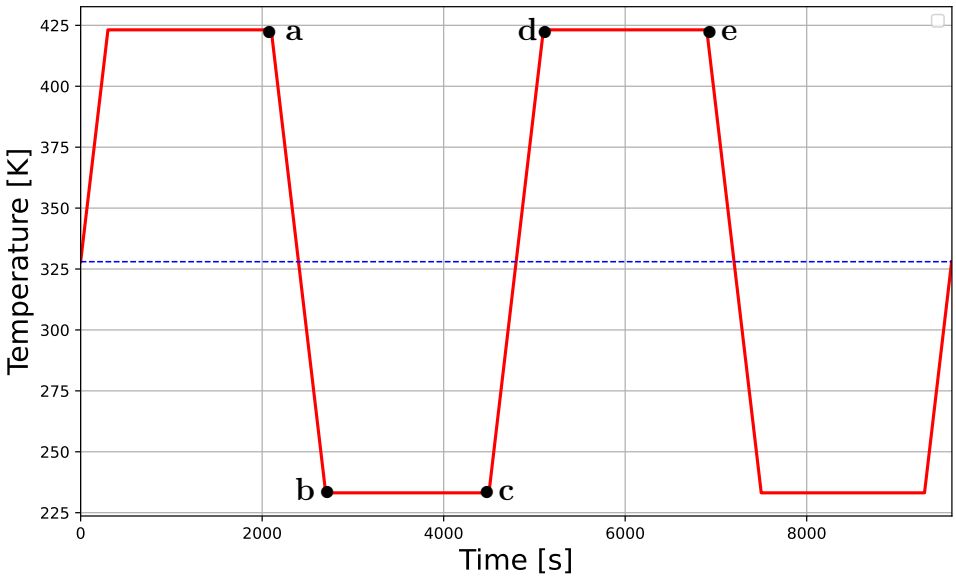

Figure 4.8: Two cycles of applied temperature profile for SAC305

Further information on the regulation of temperature profiles for electronic components is available in [44]. The temperature profile is structured with a maximum temperature of 150°C and a minimum of -40°C. The time required to increase from the minimum to the maximum temperature is 600 seconds, with a holding time of 1800 seconds.

The PCB is fixed at the bottom surface while the microchip is simply joined to the PCB via the solder joints; it is let free to deform as consequence of the applied temperature profile.

For both global model and submodel C3D8 linear elements are used.

4.3.2. Submodeling

The global model is used to compute the displacement fields at the upper and lower face of the solder ball, in Figure 4.9 a graphical representation is given.

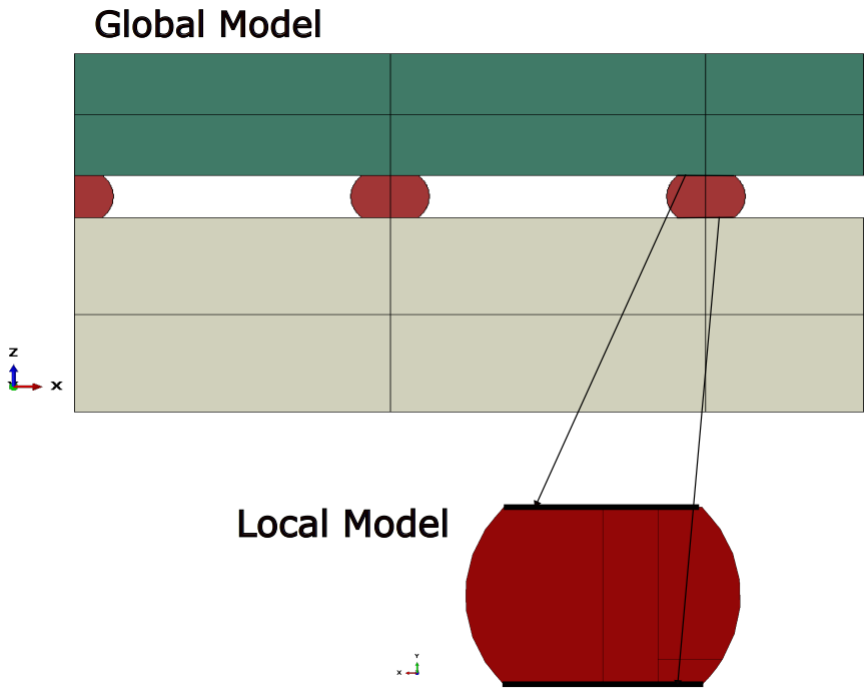

Figure 4.9: Representation of the transfer of the displacement profile from the global model to the submodel

In the submodel, the CREEP and USDFLD user-defined subroutines are also implemented; the same user-defined subroutine previously used is applied. All the experimental data are available at the same temperature, as consequence, the temperature shock test for the submodel cannot be simulated, instead a cycling shear loading is simulated. Taking advantage of the symmetries only half of the solder ball is simulated, as consequence, displacements orthogonal to the plane of symmetry are imposed equal to zero.

The use of a global model and submodel improves computational efficiency by enabling:

- the use of a coarser mesh in the global model, away from critical areas, while still capturing the overall response of the assembly without requiring a refined mesh throughout,
- a finer, localized mesh in the submodel, allowing high-resolution results in the critical solder regions,
- reduced time and memory usage by focusing computational power on the submodel.

At the same time, this approach enhances the accuracy of the simulation in critical areas, leading to better predictions regarding fatigue life and potential microcrack nucleation points. Boundary conditions are applied directly to the global model, while the submodel's

boundary conditions are imported directly from the global model, making then closer to the real scenario.

4.3.3. Solder ball cyclic behavior

The simulation is executed with the intent of identifying the values of stress and strain in the solder ball as well as the damage parameter. All the quantities are averaged considering the volume evidenced in Figure 4.10. This procedure is necessary in order to smooth out numerical errors due to the proximity of the volume with respect to the boundaries, where the displacements are imposed. This procedure takes the name of regularization technique.

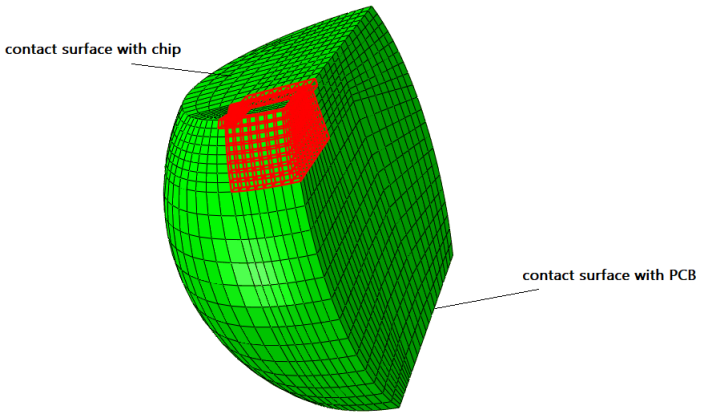

Figure 4.10: Volume of the solder ball where the average of computed quantities is carried out

In Figure 4.11 the result of the finite element simulation are shown, in particular, the stress along the direction 13 is evidenced. The stresses reach the maximum value in upper part of sphere, close to the contact with the microchip frame. On the back side a compression area is visible, over the cycles each of the two area undergo tension and compression. The points A and B represents the solder joint extremities.

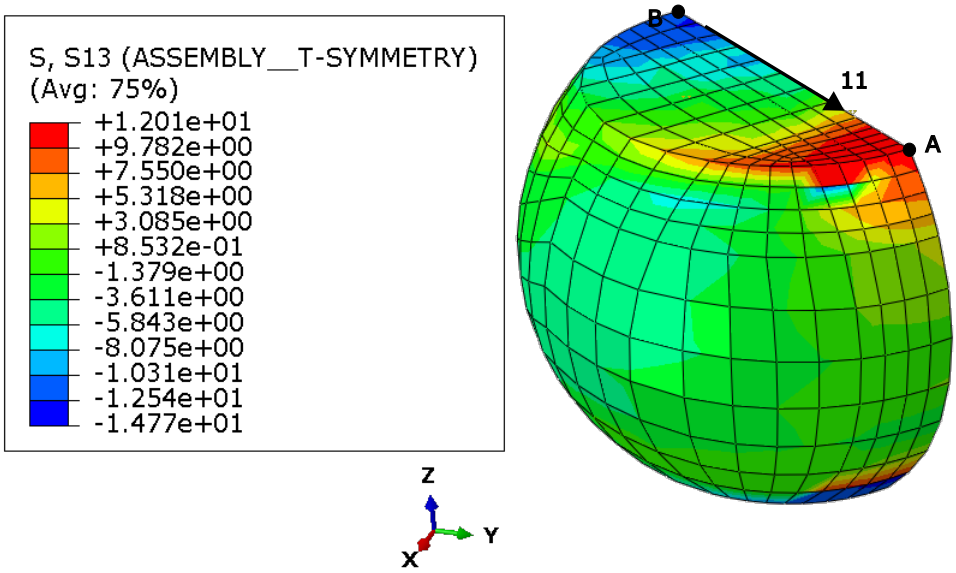

Figure 4.11: Stress map for the S13 stress component along the diagonal direction of the packaging

A total of forty cycles are simulated and results represented in Figure 4.12 and Equation 1.34. The hysteresis loop is characterized by a gradual reduction in maximum and minimum stress as consequence of the damage evolution and degradation of mechanical properties. Little changes in the hysteresis loop can be observed due to the low level of damage accumulation.

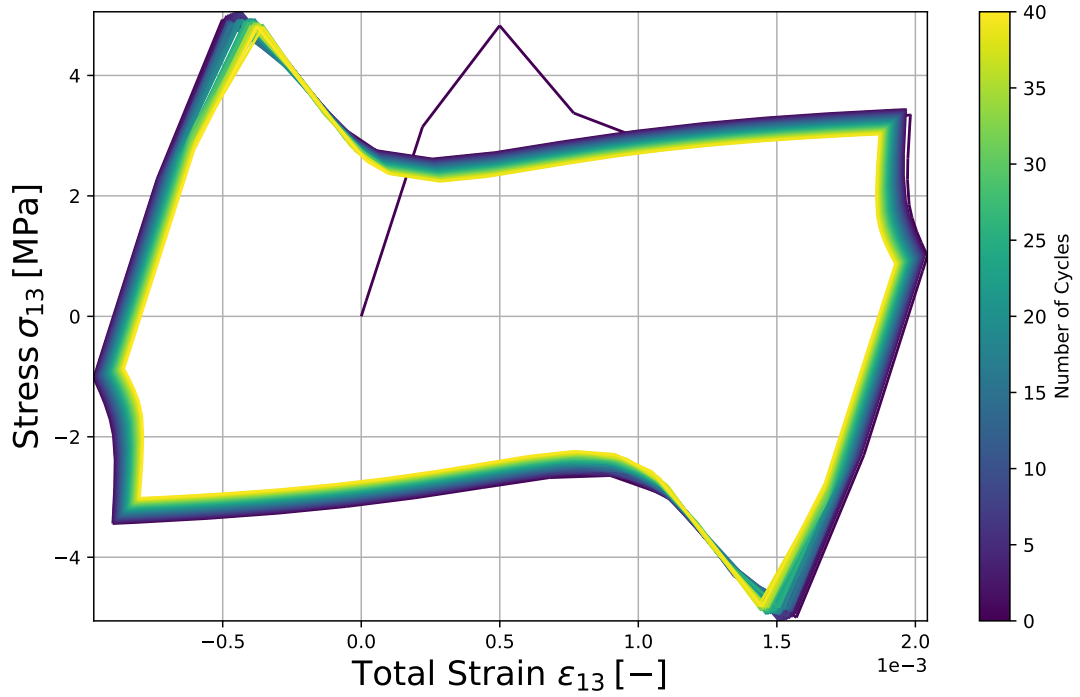

Figure 4.12: Hysteresis loop evolution over forty simulated cycles

The damage evolution is characterize by the known stepwise increase, as represented in Figure 4.13.

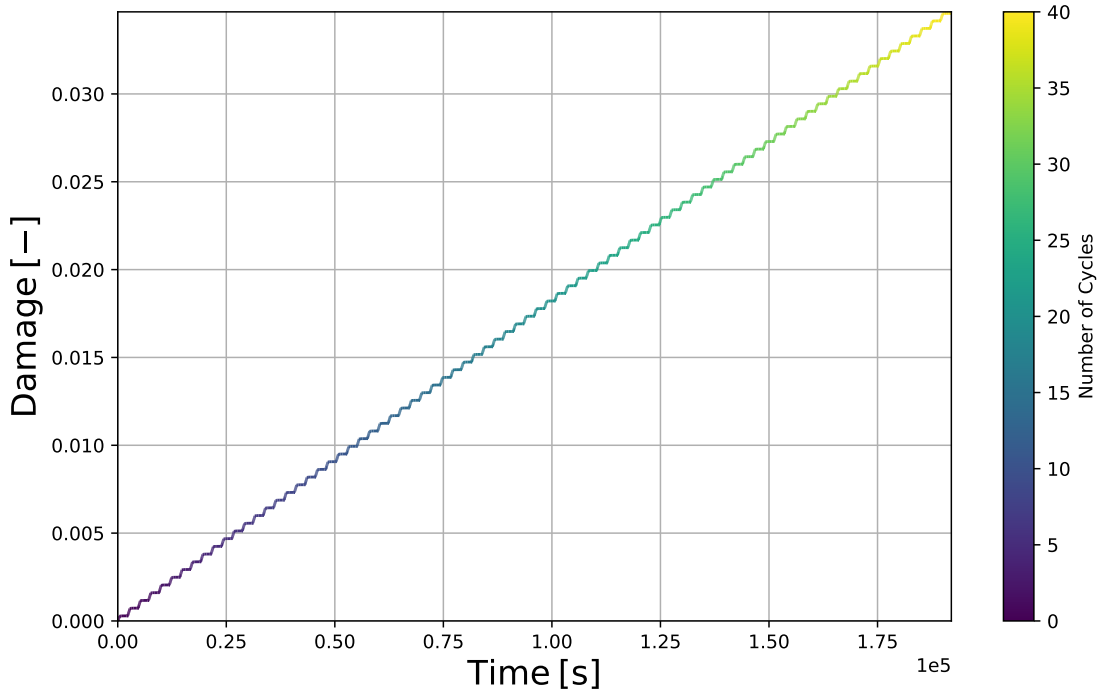

Figure 4.13: Damage evolution over forty simulated cycles

To better understand the different phases characterizing each cycle in Figure 4.14 and Figure 4.15 the first full cycle and the corresponding damage evolution are represented. Four different phases for each cycle can be recognized.

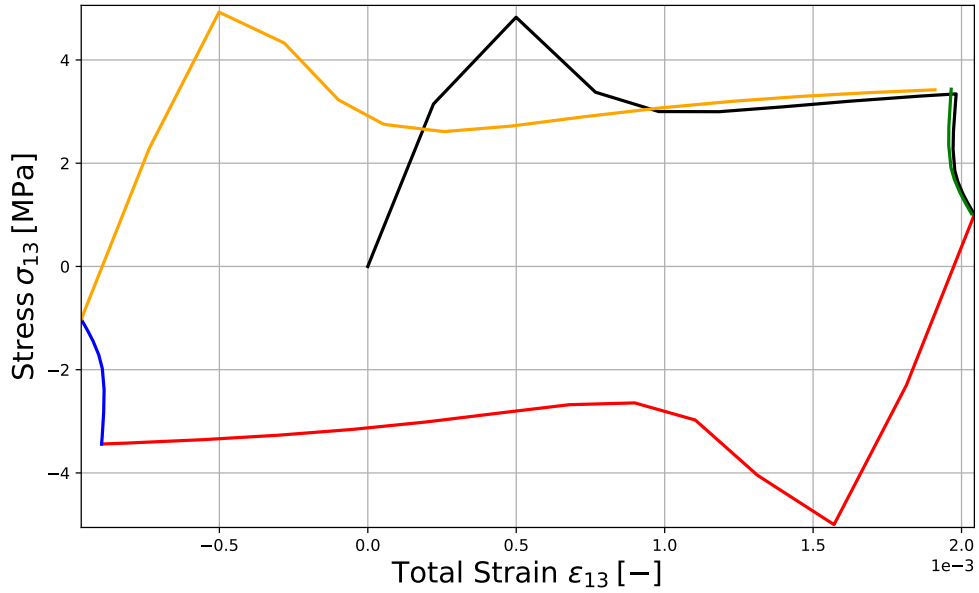

Figure 4.14: Hysteresis loop for the first cycle, different phases of the cycle highlighted

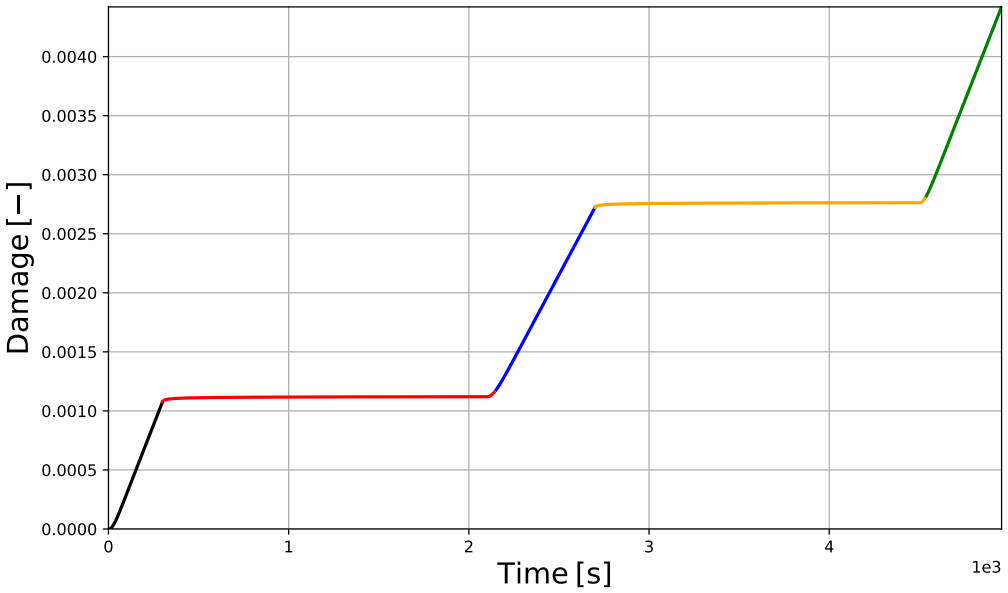

Figure 4.15: Damage for the first cycle, different phases of the cycle highlighted

Observing Figure 4.8, the letters identify the four segments of the temperature profile which correspond to four segments in the imposed displacement. As consequence of the

applied displacement profile, four corresponding segments can be identified in the two pictures above for the hysteresis loop and the damage evolution. The segment a-b is the first full temperature drop which corresponds to the total shearing in one direction, it is above indicated with the color red. The stress, in the region of interest, decreases up to the minimum and then increases to a plateau while the damage almost does not accumulates. In the segment b-c the temperature is constants, zero applied displacement, blue segments above, the stress increases and the damage evolves. Third segment c-d, orange color, shearing action in the opposite direction, stress increase takes place and subsequent saturation, damage remains almost constant. Last segment d-e, zero applied displacement, stress decreases until saturation and damage accumulates. The black lines represent the first two transition steps of the shear profile.

The evolution of the shear stress σ_{13} over the displacement profile is represented in Figure 4.16. The shear stress strongly spikes at the load reversion, when no displacement is applied relaxation is observed.

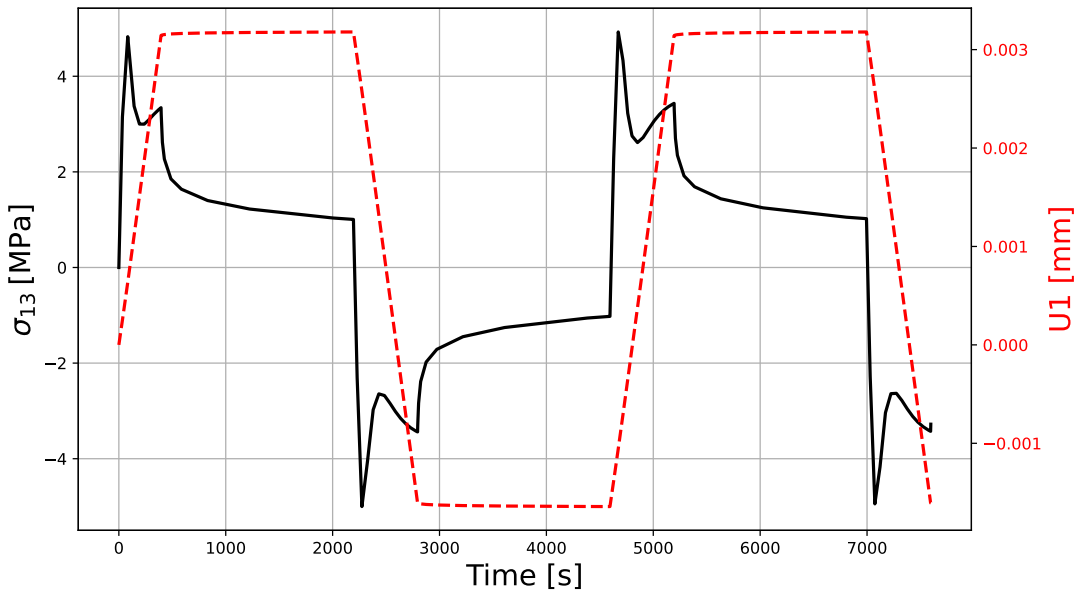

Figure 4.16: Evolution of the shear stress σ_{13} along the applied displacement profile

In the hysteresis loop the most significant components for stress and strain are represented, however it is necessary to asses which region will be the most critical and where a possible crack may start to develop. In Figure 4.17 the damage after forty cycles is displayed. As shown in Figure 4.11 higher stresses generates at the boundary between solder-PCB and solder-microchip, in these regions and along the solder diagonal is the highest level of damage computed. Being the solder the softer material in the packaging, damage is accumulating almost entirely on this component.

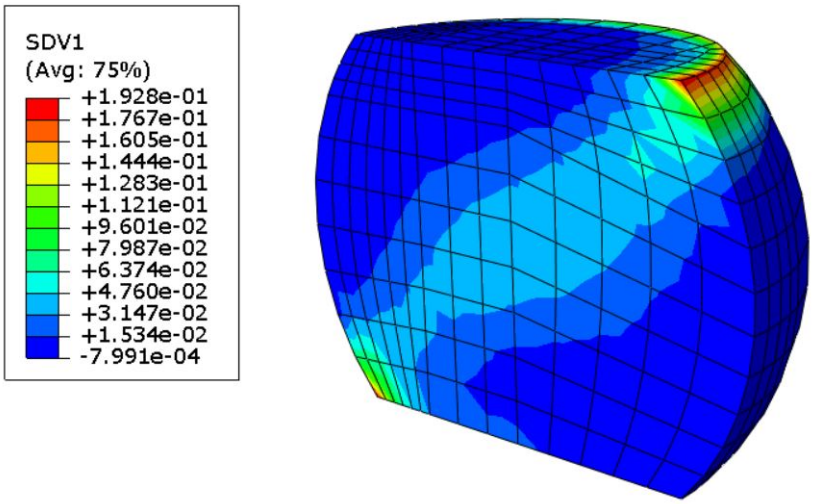

Figure 4.17: Damage level in the solder ball cross section after forty cycles

The computational burden of the simulation with forty cycles should not be underestimated, even with a locally refined mesh in the area of interest. As consequence of the low mesh refinement close to the lower solder face, significant stress discontinuity between different elements arise. More cycles and a more refined mesh could be implemented, but this would come at the cost of significantly increased hardware requirements and computation time.

5 | Conclusion and discussion

Starting from data acquired in previous works, a subset of data was made available. Specifically, the specimens first underwent strain-controlled cycling, followed by a dead-load test at five different stress levels. The specimens were subjected to varying numbers of cycles, forming a "test matrix" comprising four distinct strain ranges, each tested under a combination of mechanical cycling and applied stress. Subsequently specimens are subject to dead load test at five different stress levels. Experimental data for the secondary creep strain rate were subsequently extracted.

Considering both the NORTON and hyperbolic-sine creep laws, data on energy dissipated during mechanical cycling and the secondary creep strain rate were used to fit the creep constitutive models and identify the corresponding material parameters. The dependency of the creep strain rate on pre-cycling energy dissipation and applied stress was investigated. Various optimization algorithms were tested to determine the set of creep material parameters that minimize the residuals between experimental and numerically computed creep strain rates. The objective function exhibited strong nonlinearity and multiple minima. Results were found to be highly sensitive to the boundary conditions and the initial parameter guesses.

In order to improve the results, the statistical distribution of the parameters for each experiment is investigated. Each dataset entry was used to generate a unique set of material parameters, and the distribution of these parameters was analyzed and visualized using boxplots. Data outside of the boxplot whiskers are filtered leading to sensible decrease of the residual valued. The median for each parameter is considered. Hysteresis loop and damage evolution over time in mechanical cycling for five of the selected sets of individuated material parameters have been represented. For this step a simple elastic-creep model is considered. The sets corresponding to the lower residual values display an unrealistic shape of the hysteresis loop, the selected set of material parameters corresponds to the one obtained with a double optimization technique. Creep material constants are first individuated by fitting only undamaged specimen, low residuals are obtained, and subsequently a second optimization is carried out the identify the material parameters

that regulates damage evolution, however, the residuals increase.

The same elastic-creep model is implemented together with the material constants obtained from the double optimization, evolution of creep strain, equivalent creep strain and damage are represented. Three hundred cycles are also simulated this time considering the the change in the elastic modulus over the cycles, hysteresis loop and damage evolution are obtained. Decrease in the hysteresis loop maximum stress and area can be observed as damage is accumulated and mechanical properties degrade.

The model is the numerically verified, with the use of user-defined CREEP and USDFLD subroutines in FORTRAN, the 1D strain controlled test is simulated with the finite element software Abaqus, results are in accordance with the numerical Python model.

Since fitting of creep material parameters respect to the secondary creep strain rate does not allow to realistically reproduce the hysteresis loop and the primary creep, material parameters were identified to capture the primary creep stage based on the experimentally obtained 20th hysteresis loop. A nonlinear isotropic hardening model is implemented, resulting in high accuracy for predicted stress values. The elastic-plastic-creep is limited in its application to the single loading ramp, it cannot be use to simulate the cyclic behavior of the material. Nevertheless, the parameters derived from this hysteresis loop fitting provided poor predictions for secondary creep behavior. Conversely, when parameters were optimized based on secondary creep strain, the model produced unsatisfactory results for the hysteresis loop. This discrepancy highlights the need for a different modeling approach, specifically, a plastic-viscoplastic model that can fit both hysteresis loop points and secondary creep strain rate values effectively. One promising approach is the Chaboche model, which allows for the integration of a plastic-viscoplastic framework with damage. However, implementing this model requires data from multiple hysteresis cycles to accurately calibrate its parameters.

In the final section of this work, the ball grid array (BGA) structure is examined, with a focus on the effects of cyclic shear loading. Due to mismatches in elastic modulus and thermal expansion coefficients among the chip frame, solder balls, and PCB, cyclic stress states are induced in the assembly. Using a similar procedure to the previous FE simulation, the material creep constants remained unchanged. Also in this case, CREEP and USDFLD user-defined subroutines are implemented; a submodeling approach is employed to enhance simulation accuracy. A global model, comprising the chip frame, solder balls, and PCB, is first simulated to capture the overall packaging response. Displacement fields from this global model are then exported and applied as boundary conditions on the submodel, which focuses on a single solder ball. This submodeling approach allows for a

realistic representation of system evolution, as it captures the interactions between different assembly components and applies more accurate boundary conditions to the local model.

The simulation allows to identify the most stressed regions as consequence of the cyclic shear loading and asses in which areas the damage accumulates faster. The identified regions corresponds with what can be found from experimental procedures. Hysteresis loop and damage evolution over the cycles are also represented. The influence of the different phases of the hysteresis loop on the damage accumulation are evidenced.

Future efforts should be made in the direction of implementing a unique model able to model both plastic and creep deformation and at the same take into account the evolution of damage parameter. At the same time elaborate a more realistic model data must be corrected at different temperatures in order to simulate a temperature shock test.

Bibliography

[1] K. Agakhi and D. Georgievskii. Tensor nonlinear constitutive relations of isotropic creep theorywith tensor measure of damage, izv. *Tulsk. Gos. Univ. Estestv. Nauki*, (2):2–9, 2013.

[2] J. Albiez, I. Sprenger, C. Seemüller, D. Weygand, M. Heilmaier, and T. Böhlke. Physically motivated model for creep of directionally solidified eutectics evaluated for the intermetallic nial–9mo. *Acta Materialia*, 110:377–385, 2016.

[3] H. Altenbach, P. Schieße, and A. Zolochevsky. Zum kriechen isotroper werkstoffe mit komplizierten eigenschaften. *Rheologica acta*, 30:388–399, 1991.

[4] E. N. D. C. Andrade. On the viscous flow in metals, and allied phenomena. *Proceedings of the Royal Society of London. Series A, Containing Papers of a Mathematical and Physical Character*, 84(567):1–12, 1910.

[5] E. N. D. C. Andrade. The flow in metals under large constant stresses. *Proceedings of the Royal Society of London. Series A, Containing Papers of a Mathematical and Physical Character*, 90(619):329–342, 1914.

[6] R. Arutyunyan. Fracture criteria under creep conditions. *Strength of Materials*, 14 (9):1205–1209, 1982.

[7] R. Arutyunyan. The problem of strain aging and long-term fracture in mechanics of materials. *St. Petersburg: Publishing House of St. Petersburg State University*, 2004.

[8] R. Bailey. The utilization of creep test data in engineering design. *Proceedings of the Institution of Mechanical Engineers*, 131(1):131–349, 1935.

[9] M. M. Basit, M. Motalab, J. C. Suhling, and P. Lall. The effects of aging on the anand viscoplastic constitutive model for sac305 solder. In *14th IEEE Intersociety Conference on Thermal and Thermomechanical Phenomena in Electronic Systems (ITherm)*, pages 112–119, Orlando, FL, 2014. IEEE. doi: 10.1109/ITHERM.2014.6892288.

[10] Z. Bažant and Y. Zhu. Why did the world trade center collapse?—simple analysis. *Journal of Engineering Mechanics*, Jan. 2002.

[11] P. Becker, H. Friedrich, K. Fujii, W. Giardini, G. Mana, A. Picard, H.-J. Pohl, H. Riemann, and S. Valkiers. The avogadro constant determination via enriched silicon-28. *Meas. Sci. Technol*, 20:92002–20, 09 2009. doi: 10.1088/0957-0233/20/9/092002.

[12] V. Betekhtin, A. Kadomtsev, and A. Petrov. Microfracture of metals during high-temperature creep. *Metal Science and Heat Treatment*, 22(12):879–881, 1980.

[13] B. Cane. Deformation-induced intergranular creep cavitation in alpha-iron. *Metal Science*, 12(2):102–108, 1978.

[14] I.-W. Chen. Mechanisms of cavity growth in creep. *Scr. Metall.;(United States)*, 17 (1), 1983.

[15] I.-W. Chen and A. Argon. Creep cavitation in 304 stainless steel. *Acta Metallurgica*, 29(7):1321–1333, 1981.

[16] Y. Chen, T. Hauck, A. Fahim, M. A. Haq, M. A. Hoque, and J. C. Suhling. Damage evolution in sac solder alloys. In *2022 23rd International Conference on Thermal, Mechanical and Multi-Physics Simulation and Experiments in Microelectronics and Microsystems (EuroSimE)*, pages 1–9. IEEE, 2022.

[17] P. Delobelle, F. Trivaudey, and C. Oytana. High temperature creep damage under biaxial loading: Inco 718 and 316 (17-12 sph) steels. *Nuclear engineering and design*, 114(3):365–377, 1989.

[18] N. Dowling. *Mechanical Behavior of Materials*. Pearson, 4th edition, 2013. ISBN 9780131395060.

[19] D. Dunand, B. Han, and A. M. Jansen. Monkman-grant analysis of creep fracture in dispersion-strengthened and particulate-reinforced aluminum. *Metallurgical and Materials Transactions A*, 30:829–838, 1999.

[20] P. Duval, M. Montagnat, F. Grennerat, J. Weiss, J. Meyssonnier, and A. Philip. Creep and plasticity of glacier ice: A material science perspective. *Journal of Glaciology*, 56(200):1059–1068, 2010. doi: 10.3189/002214311796406185. URL `https://doi.org/10.3189/002214311796406185`.

[21] B. Dyson. Continuous cavity nucleation and creep fracture. *Scr. Metall.;(United States)*, 17(1), 1983.

[22] B. Dyson and M. Loveday. Creep fracture in nimonic 80a under triaxial tensile stressing. In *Creep in Structures: 3rd Symposium, Leicester, UK, September 8–12, 1980*, pages 406–421. Springer, 1981.

[23] B. Dyson and D. Taplin. Creep damage accumulation. In *Grain Bound. Inst. Met. Spring Resident. Conf*, pages 23–28, 1976.

[24] H. Evans. The mechanism of void growth and factors affecting the onset of intergranular failure during creep of a mg–0· 8% al alloy. *Metal Science Journal*, 3(1): 33–38, 1969.

[25] H. E. Evans. Mechanisms of creep fracture. *(No Title)*, 1984.

[26] A. Fahim, K. Hasan, J. C. Suhling, and P. Lall. Prediction of stress-strain behavior of thermally cycled SAC305 solder joints by finite element modeling and nanoindentation characterization. In *20th IEEE Intersociety Conference on Thermal and Thermomechanical Phenomena in Electronic Systems (iTherm)*, pages 917–923, Orlando, FL, 2021. IEEE. doi: 10.1109/ITHERM51669.2021.9503218. URL `https://ieeexplore.ieee.org/document/9503218`.

[27] J. Feng, D. E. Xu, Y. Tian, and M. Mayer. Sac305 solder reflow: identification of melting and solidification using in-process resistance monitoring. *IEEE Transactions on Components, Packaging and Manufacturing Technology*, 9(8):1623–1631, 2019.

[28] N. N. FR and H. De Villiers. The physics of creep: creep and creep-resistant alloys, 1995.

[29] D. François, A. Pineau, and A. Zaoui. *Mechanical behaviour of materials*, volume 2. Springer, 1998.

[30] H. J. Frost and M. Ashby. Deformation-mechanism maps: The plasticity and creep of metals and ceramics(book). *Oxford, Pergamon Press, 1982, 175 p*, 1982.

[31] N. Fu, S. Ahmed, J. C. Suhling, and P. Lall. Visualization of microstructural evolution in lead free solders during isothermal aging using time-lapse imagery. In *2017 IEEE 67th Electronic Components and Technology Conference (ECTC)*, pages 429–440. IEEE, 2017.

[32] N. Fu, J. C. Suhling, S. Hamasha, and P. Lall. Mechanical fatigue cycling induced evolution of cyclic stress-strain and constitutive behaviors of sac305 lead free solder. In *16th IEEE Intersociety Conference on Thermal and Thermomechanical Phenomena in Electronic Systems (ITHERM)*, pages 1353–1363, Orlando, FL, 2017. IEEE. ISBN 978-1-5090-2994-5. doi: 10.1109/ITHERM.2017.7992543.

[33] F. Furillo, S. Purushothaman, and J. Tien. Understanding the larson-miller parameter. *Scripta Metallurgica*, 11, 1977.

[34] M. Galarnyk. Understanding boxplots, 2019. URL `https://www.codementor.io/@mgalarny/understanding-boxplots-10cbs1cyap`. Accessed: 2024-11-17.

[35] E. George, D. Das, M. Osterman, and M. Pecht. Thermal cycling reliability of lead-free solders (sac305 and sn3.5ag) for high-temperature applications. *IEEE Transactions on Device and Materials Reliability*, 11(2):328–338, 2011.

[36] S. Glane, A. Morozov, W. Müller, T. Hauck, G. Mazumder, M. Haq, and J. Suhling. Analytical and experimental studies on the damage evolution of sac solder alloys. In *2023 24th International Conference on Thermal, Mechanical and Multi-Physics Simulation and Experiments in Microelectronics and Microsystems (EuroSimE)*, pages 1–8. IEEE, 2023.

[37] A. I. Grishchenko and A. S. Semenov. Effective methods of parameter identification for creep models with account of iii stage. In *MATEC Web of Conferences*, volume 53, page 01041. EDP Sciences, 2016. doi: 10.1051/matecconf/20165301041. URL `https://doi.org/10.1051/matecconf/20165301041`.

[38] M. A. Haq, M. A. Hoque, G. R. Mazumder, J. C. Suhling, and P. Lall. Evolution of sac305 mechanical behavior due to damage accumulation during cycling. In *2022 IEEE 72nd Electronic Components and Technology Conference (ECTC)*, pages 1472–1481. IEEE, 2022.

[39] T. Hauck and Y. Chen. Mechanical behavior of lead-free solder joints in microelectronics, 2024. Document presented at the NXP.

[40] W. Hoffelner. Damage assessment in structural metallic materials for advanced nuclear plants. *Journal of materials science*, 45(9):2247–2257, 2010.

[41] J. P. Hofmeister, P. Lall, D. Panchagade, N. N. Roth, T. A. Tracy, J. B. Judkins, and K. L. Harris. Ball grid array (bga) solder joint intermittency detection: Sj bist. In *2008 IEEE Aerospace Conference*, pages 1–11. IEEE, 2008.

[42] M. A. Hoque, M. A. Haq, J. C. Suhling, and P. Lall. Mechanical behavior and microstructure evolution in lead free solders subjected to mechanical cycling at elevated temperatures. In *2021 IEEE 71st Electronic Components and Technology Conference (ECTC)*, pages 2340–2347. IEEE, 2021.

[43] H. Hosokawa, H. Iwasaki, T. Mori, M. Mabuchi, T. Tagata, and K. Higashi. Effects

of si on deformation behavior and cavitation of coarse-grained al–4.5 mg alloys exhibiting large elongation. *Acta materialia*, 47(6):1859–1867, 1999.

[44] JEDEC Solid State Technology Association. Temperature cycling, 2023. URL `https://www.jedec.org`. Revision of JESD22-A104F, April 2023.

[45] Q. Jiang. *Anisotropic Multi-Scale Modeling for Steady-State Creep Behavior of Oligocrystalline SnAgCu (SAC) Solder Joints*. Ph.d. dissertation, University of Maryland, College Park, College Park, MD, 2021. URL `URLifavailable`.

[46] A. E. Johnson and B. Khan. Creep under changing complex-stress systems in copper at 250° c. *International Journal of Mechanical Sciences*, 7(12):791–810, 1965.

[47] S. G. Johnson. The nlopt nonlinear-optimization package, python reference, 2024. URL `https://nlopt.readthedocs.io/en/latest/NLopt_Python_Reference/`. Accessed: 2024-10-05.

[48] L. Kachanov. On creep rupture time. *Izv. Acad. Nauk SSSR, Otd. Techn*, 8:26–31, 1958.

[49] L. Kachanov. *Introduction to continuum damage mechanics*, volume 10. Springer Science & Business Media, 1986.

[50] L. M. Kachanov. Principles of fracture mechanics. *Russian, Moscow, Nauka*, 1974.

[51] M. Kassner and T. Hayes. Creep cavitation in metals. *International journal of plasticity*, 19(10):1715–1748, 2003.

[52] M. Kassner, T. Kennedy, and K. Schrems. The mechanism of ductile fracture in constrained thin silver films. *Acta materialia*, 46(18):6445–6457, 1998.

[53] M. E. Kassner. *Fundamentals of creep in metals and alloys*. Butterworth-Heinemann, 2015.

[54] M. Kawai. Creep and plasticity of austenitic stainless steel under multiaxial nonproportional loadings at elevated temperatures. *Visco-plastic behavior of new materials, ASME, PVP*, 184:85–93, 1989.

[55] E. Krempl. Creep-plasticity interaction. In *Creep and damage in materials and structures*, pages 285–348. Springer, 1999.

[56] J. Lemaître and J.-L. Chaboche. Aspect phénoménologique de la rupture par endommagement. *J Méc Appl*, 2(3), 1978.

[57] J. Lemaitre and J.-P. Sermage. One damage law for different mechanisms. *Computational mechanics*, 20(1):84–88, 1997.

[58] A. Lokoshchenko. Modeling the long-term strength of metals in an unsteady complex stress state. *Mechanics of Solids*, 53:88–100, 2018.

[59] A. M. Lokoshchenko. *Creep and long-term strength of metals*. CRC Press, 2017.

[60] P. Magnusson, J. Chen, and W. Hoffelner. Thermal and irradiation creep behavior of a titanium aluminide in advanced nuclear plant environments. *Metallurgical and Materials Transactions A*, 40:2837–2842, 2009.

[61] M. Mathew, H. Yang, S. Movva, and K. Murty. Creep deformation characteristics of tin and tin-based electronic solder alloys. *Metallurgical and Materials Transactions A*, 36:99–105, 2005.

[62] G. R. Mazumder, M. A. Haq, J. C. Suhling, P. Lall, Y. Chen, T. Hauck, and A. Fahim. A continuum damage mechanics approach for the reliability of lead-free solders subjected to cyclic loading. In *2023 IEEE 73rd Electronic Components and Technology Conference (ECTC)*, pages 713–720. IEEE, 2023.

[63] D. McLean. The physics of high temperature creep in metals. *Reports on Progress in Physics*, 29(1):1, 1966.

[64] M. A. Miner. Cumulative Damage in Fatigue. *Journal of Applied Mechanics*, 12 (3):A159–A164, 03 2021. ISSN 0021-8936. doi: 10.1115/1.4009458. URL `https://doi.org/10.1115/1.4009458`.

[65] R. v. Mises. Mechanik der plastischen formänderung von kristallen. *ZAMM-Journal of Applied Mathematics and Mechanics/Zeitschrift für Angewandte Mathematik und Mechanik*, 8(3):161–185, 1928.

[66] F. C. Monkman. An empirical relationship between rupture life and minimum creep rate in creep-rupture tests. In *Proc of the ASTM*, volume 56, pages 593–620, 1956.

[67] A. Morozov. Introduction to creep modeling, may 2024. Lecture slides presented at Aalto University, 20-21 May 2024.

[68] M. Motalab, Z. Cai, J. C. Suhling, and P. Lall. Determination of anand constants for sac solders using stress-strain or creep data. In *Proceedings of the 13th IEEE Intersociety Conference on Thermal and Thermomechanical Phenomena in Electronic Systems (ITHERM)*, pages 910–920, San Diego, CA, USA, 2012. IEEE. doi: 10.1109/ITHERM.2012.6231535.

[69] S. Murakami and N. Ohno. A continuum theory of creep and creep damage. In *Creep in Structures: 3rd Symposium, Leicester, UK, September 8–12, 1980*, pages 422–444. Springer, 1981.

[70] M. Naeem, R. Singh, and D. Probert. Implications of engine deterioration for creep life. *Applied energy*, 60(4):183–223, 1998.

[71] I. Namestnikov and S. Shesterikov. Vector representation of the damage parameter (in russ.). In *Deformation and Destruction of Solids: Collection of Works of Institute of Mechanics*, pages 43–52. Moscow State University named after M.V. Lomonosov, Moscow, 1985.

[72] K. Naumenko and H. Altenbach. *Modeling of Creep for Structural Analysis*. Springer, 01 2007. ISBN 9783540708391. doi: 10.1007/978-3-540-70839-1_1.

[73] A. Needleman and J. Rice. Plastic creep flow effects in the diffusive cavitation of grain boundaries. In *Perspectives in creep fracture*, pages 107–124. Elsevier, 1983.

[74] T. Nieh and W. Nix. A comparison of the dimple spacing on intergranular creep fracture surfaces with the slip band spacing for copper. *Scripta Metallurgica*, 14(3): 365–368, 1980.

[75] F. Norton. *Creep of Steel at High Temperatures*. McGraw-Hill, New York, 1929.

[76] V. Novozhilov. O plasticheskon razrykhlenii pmm vol. 29, n. 4, 1965, pp. 681-689. *Journal of Applied Mathematics and Mechanics*, 29(4):811–819, 1965.

[77] O. Ochonogor, E. T. Akinlabi, and D. Nyembwe. A review on the effect of creep and microstructural change under elevated temperature of ti6al4v alloy for turbine engine application. *Materials today: proceedings*, 4(2):250–256, 2017.

[78] F. Odqvist and J. Hult. *Kriechfestigkeit metallischer Werkstoffe*. Springer, Berlin u.a., 1962.

[79] F. K. Odqvist. Mathematical theory of creep and creep rupture. *(No Title)*, 1974.

[80] F. K. Odqvist and J. Hult. *Kriechfestigkeit metallischer Werkstoffe*. Springer-Verlag, 2013.

[81] Z. Paska, R. Halama, P. Dymacek, B. Govindaraj, and J. Rojicek. Comparison of tensile and creep properties of sac305 and sacx0807 at room temperature with dic application. *Applied Sciences*, 14:604, 2024. doi: 10.3390/app14020604.

[82] W. Pavinich and R. Raj. Fracture at elevated temperature. *Metallurgical Transactions A*, 8:1917–1933, 1977.

[83] R. Penny, D. Marriott, R. Penny, and D. Marriott. Methods of analysis for constant loading and temperature conditions. *Design for Creep*, pages 44–91, 1995.

[84] I. Rabotnov. *Creep Problems in Structural Members*. Applied mathematics and mechanics. North-Holland Publishing Company, 1969. ISBN 9780720423570. URL `https://books.google.de/books?id=24VlAAAAMAAJ`.

[85] Y. Rabotnov. A mechanism of the long term fracture (in russ.). In *Voprosy Prochnosti Materialov i Konstruktsii*, pages 5–7. Izdatel'stvo AN SSSR, Moscow, 1959.

[86] R. Raj and M. Ashby. Intergranular fracture at elevated temperature. *Acta metallurgica*, 23(6):653–666, 1975.

[87] R. Ratcliffe and G. Greenwood. The mechanism of cavitation in magnesium during creep. *Philosophical Magazine*, 12(115):59–69, 1965.

[88] E. B. Romdhane, P. Roumanille, A. Guédon-Gracia, S. Pin, P. Nguyen, and H. Frémont. From early microstructural evolution to intergranular crack propagation in sac solders under thermomechanical fatigue. *Microelectronics Reliability*, 126:114288, 2021.

[89] J. Rösler, H. Harders, and M. Bäker. *Mechanisches Verhalten der Werkstoffe*. Springer, 2 edition, 2006. ISBN 3-8351-0008-4.

[90] A. Rzhanitsyn. Theory of long-term strength under arbitrary uniaxial and biaxial loading (in russ.). *Stroitel'naya Mekhanika and Calculation of Construction*, (4): 25–29, 1975.

[91] R. Saitova, A. Arutyunyan, and H. Altenbach. High temperature creep and embrittlement in metals and alloys under conditions of the long-term usage. *Acta Mechanica*, 2024. Manuscript Draft.

[92] SciPy Community. *scipy.interpolate.interp1d*. SciPy, 2024. URL `https://docs.scipy.org/doc/scipy/reference/generated/scipy.interpolate.interp1d.html`. Accessed: 2024-08-09.

[93] SciPy Community. *scipy.integrate.solve_ivp*. SciPy, 2024. URL `https://docs.scipy.org/doc/scipy/reference/generated/scipy.integrate.solve_ivp.html`. Accessed: 2024-08-09.

[94] SciPy Developers. *SciPy Optimize: Minimize function*, 2024. URL `https://docs.`

scipy.org/doc/scipy/reference/generated/scipy.optimize.minimize.html. Accessed: 2024-08-06.

[95] J. Skrzypek and R. Hetnarski. Schematizations of the stress-strain curves. *Plasticity and Creep Theory, Examples, and Problems, CRC Press, Inc., Boca Raton, FL*, pages 43–48, 1993.

[96] S. Taira and R. Otani. Theory of high-temperature strength of materials. *Moscow: Metallurgiya*, 1986.

[97] H. Trinkaus and M. Yoo. Nucleation under time-dependent supersaturation. *Philosophical Magazine A*, 55(3):269–289, 1987.

[98] F. Trivaudey and P. Delobelle. High Temperature Creep Damage Under Biaxial Loading—Part II: Model and Simulations. *Journal of Engineering Materials and Technology*, 112(4):450–455, 10 1990. ISSN 0094-4289. doi: 10.1115/1.2903356. URL https://doi.org/10.1115/1.2903356.

[99] M. T. University. Creep experiment, 2024. URL https://www.mtu.edu/materials/k12/experiments/creep/. Accessed: 2024-05-15.

[100] J. Waddington and K. Lofthouse. The effect of irradiation on the high temperature fracture of stainless steel. *Journal of Nuclear Materials*, 22(2):205–213, 1967.

[101] A. Waseda, K. Fujii, and N. Taketoshi. Density measurement of a thin-film by the pressure-of-flotation method. *IEEE Transactions on instrumentation and measurement*, 54(2):882–885, 2005.

[102] T. Watanabe and P. W. Davies. Grain boundary sliding and intergranular fracture behaviour of copper bicrystals. *Philosophical Magazine A*, 37(5):649–681, 1978.

[103] J. Weertman. Zener–stroh crack, zener–hollomon parameter, and other topics. *Journal of applied physics*, 60(6):1877–1887, 1986.

[104] Wikipedia contributors. Datei:bga und via imgp4531 wp.jpg, 2024. URL https://de.m.wikipedia.org/wiki/Datei:Bga_und_via_IMGP4531_wp.jpg. Accessed: 2024-07-03.

[105] J. Xian, S. Belyakov, and C. Gourlay. Time-lapse imaging of ag 3 sn thermal coarsening in sn-3ag-0.5 cu solder joints. *Journal of Electronic Materials*, 50:786–795, 2021.

[106] M. Yoo and H. Trinkaus. Crack and cavity nucleation at interfaces during creep. *Metallurgical Transactions A*, 14:547–561, 1983.

[107] Z. Zhang, Z. Chen, S. Liu, and F. Dong. Parameter identification of anand constitutive models for sac305 using the intelligent optimization algorithm. *21st Electronics Packaging Technology Conference*, 2019.

Appendix A

```
      SUBROUTINE CREEP(DECRA,DESWA, STATEV, SERD, EC, ESW, P, QTILD,
     1 TEMP, DTEMP, PREDEF, DPRED, TIME, DTIME, CMNAME, LEXIMP, LEND,
     2 COORDS, NSTATV, NOEL, NPT, LAYER, KSPT, KSTEP, KINC)
C
      INCLUDE 'ABA_PARAM.INC'
C
      CHARACTER*80 CMNAME,ORNAME
C
      DIMENSION DECRA(5), DESWA(5), STATEV(*), PREDEF(*), DPRED(*),
     1 TIME(2), COORDS(*), EC(2), ESW(2)
      DOUBLE PRECISION A,B,C,D,DAMAGE
C
      A = 2.16948480D-07
      B = 4.90883948D-02
      C = 2.76578556D0
C
      DAMAGE = STATEV(1)
      DECRA(1) = A * (SINH(B * QTILD/(1.0d0-DAMAGE)))**C * DTIME
C
      STATEV(2) = A * (SINH(B * QTILD/(1.0d0-DAMAGE)))**C
C
      RETURN
      END SUBROUTINE CREEP
C
C
      SUBROUTINE USDFLD(FIELD,STATEV,PNEWDT,DIRECT,T,CELENT,
     1 TIME,DTIME,CMNAME,ORNAME,NFIELD,NSTATV,NOEL,NPT,LAYER,
     2 KSPT,KSTEP,KINC,NDI,NSHR,COORD,JMAC,JMATYP,MATLAYO,LACCFLA)
C
      INCLUDE 'ABA_PARAM.INC'
C
      CHARACTER*80 CMNAME,ORNAME
      CHARACTER*3  FLGRAY(15)
C
      DIMENSION FIELD(NFIELD),STATEV(NSTATV),DIRECT(3,3),
```

```
      1 T(3,3),TIME(2)
       DIMENSION ARRAY(15),JARRAY(15),JMAC(*),JMATYP(*),
      1 COORD(*)
       DOUBLE PRECISION W_CR,EPS_CR,SIGMA
C
       CALL GETVRM('CE',ARRAY,JARRAY,FLGRAY,JRCD,JMAC,JMATYP,
      1 MATLAYO,LACCFLA)
       EPS_CR = ARRAY(7)
C
       CALL GETVRM('SINV',ARRAY,JARRAY,FLGRAY,JRCD,JMAC,JMATYP,
      1 MATLAYO,LACCFLA)
       SIGMA = ARRAY(1)
C
       W_CR = 1208.14291894D0
C
       FIELD(1) = STATEV(1) + 1.d0/W_CR * SIGMA * STATEV(2) * DTIME
       STATEV(1) = FIELD(1)
C
       RETURN
       END SUBROUTINE USDFLD
```

Listing 5.1: Implementation of CREEP and USDFLD ABAQUS subroutines for 1D strain controlled test

Managing numerical overflow in hyperbolic sine computations

The correct formulation of the objective function in the optimization process is crucial to avoid potential overflow issues and ensure numerical stability, especially when handling large values in hyperbolic sine calculations and related expressions. The code used for this purpose is shown in Listing 5.2; it is designed to maintain stability regardless of the input values by carefully managing potential sources of overflow.

The command `np.clip` is used to ensure results remain within specified limits, thus avoiding excessively large or small numbers. Due to the rapid growth of the hyperbolic sine function, a small change in its argument can lead to extremely large values. Here, too, the `np.clip` command helps to control these values. In cases where values are too large to be safely raised to a power, a logarithmic approach is applied instead. By taking the logarithm first, this method provides better control over the calculation and reduces the risk of overflow.

```
def objective_sine(params):
```

```
    C1_tilde, C2, C3, C5 = params

    # Prevent overflow by clamping large values of sigma/denominator
    denominator = 1.0 - (delta_W / (C5))
    denominator = np.clip(denominator, 1e-12, np.inf)  # Avoid division
by zero or negative values

    # Handle potential large values in sinh argument by clamping them
    sinh_argument = np.clip(C2 * sigma / denominator, -700, 700)  #
Clamp to avoid overflow in sinh
    sinh_term = np.sinh(sinh_argument)

    # If sinh_term is very large, take the logarithm approach
    sinh_term = np.where(sinh_term > 1e100, np.exp(C3 * np.log(sinh_term
)), sinh_term ** C3)

    # Predicted strain rates
    predicted = C1_tilde * sinh_term

    # Compute the difference and avoid overflow in squaring large values
    diff = creep_strain_rate - predicted
    diff = np.clip(diff, -1e12, 1e12)  # Prevent overflow in diff ** 2

    # Compute the error (normalized MSE)
    error_sine = norm_factor * np.sqrt(np.mean(diff ** 2))

    return error_sine
```

Listing 5.2: Objective function implementation with overflow control for hyperbolic sine salculations

List of Figures

1 Time-lapse BSE images of a SAC305/Cu joint during aging at 125°C. (a) is the as-solidified microstructure. Aging times are indicated in (b–i). Boxes show particles undergoing coarsening (green) and coalescence (orange) [105] 2
2 Crack initiation site at 360 cycles [88] 3
3 Evolution of SAC305 Microstructure with mechanical cycling at T = 25 °C [42] 4

1.1 Schematic representation of a creep testing machine [18] 7
1.2 Strain versus time behavior during creep under constant load and the three stages of creep [18] 8
1.3 Influence of stress and temperature on the creep behavior. **a** Stress dependence, **b** temperature dependence [72] 9
1.4 Strain rate dependence of the stress-strain behavior [72] 9
1.5 Effect of initial plastic strain on creep behavior [72], for details [54] 10
1.6 Three different levels of observation of the material [67] 11
1.7 Climb of an edge dislocation, allowing continued glide past an obstacle and enabling deformation process [18] 12
1.8 Cavity growth as effect of sliding boundaries [14] 13
1.9 Grain boundary cavitation and cracking as consequence of creep in a tantalum alloy (T-111),test carried out in creep–fatigue interaction with temperature variation between 200 and 1150°C, [18] 14
1.10 (a) Wedge (or w-type) crack formed at the triple junctions as consequence of grain boundary sliding; (b) illustrates a wedge crack as an accumulation of spherical cavities [51] 15
1.11 Cavitation (r-type) or voids at transverse grain boundary. The angle ψ is assumed around 70° [51] 16

1.12 Cavity nucleation mechanism: (a) sliding leading to cavitation from ledges (and triple points); (b) cavity nucleation from vacancy condensation at a high stress region; (c) cavity nucleation from a Zener–Stroh mechanism; (d) the formation of a cavity from a particle-obstacle in conjunction with the mechanisms described in (a–c) [51] 17
1.13 Cavity growth from diffusion across the cavity surface and through the grain boundaries as effect of the stress gradient [51] 19
1.14 Deformation-mechanism map for creep (L.T.Creep - low temperature creep, H.T. Creep - high temperature creep) [72] 25
1.15 Cavity formation in the rupture section [99] 28
1.16 Apparatus for hydrostatic weighting developed at NMIJ [101], [11] 29

2.1 Micro-tester equipped with thermal chamber [62] 35
2.2 Typical hysteresis loop and area calculation [32] 36
2.3 20th hysteresis loops for SAC305 subjected to mechanical cycling with different strain ranges [38] 37
2.4 Initial plastic work vs. total strain range (SAC305, cycling at 25 °C) [62] . 38
2.5 Evolution of the steady state secondary creep rate ($\dot{\varepsilon}$) with the total energy dissipated in the material for various applied stress levels [62] 39
2.6 Fully reversed triangle wave strain profile applied on the specimens, strain rate equal to $0.002\,\mathrm{s}^{-1}$ 43
2.7 Comparison between experimental datapoints and interpolated surface using the hyperbolic-sine law with the free-nlopt parameter set 49
2.8 Comparison between experimental datapoints and interpolated surface using the NORTON law 50
2.9 Comparison between experimental datapoints and interpolated lines using the hyperbolic-sine law with the free-nlopt parameter set 51
2.10 Comparison between experimental datapoints and interpolated lines using the NORTON law 52
2.11 Comparison between experimental datapoints and interpolated curve using the hyperbolic-sine law for undamaged specimens 53
2.12 Boxplot reporting the results for the optimization problem of the entire set of specimen with pre-damage (red dots) and from the optimization of the single lines (purple dots) 55
2.13 Scheme representing the structure of the used box plot [34] 56
2.14 Boxplot representing the filtered and normalized set of data 57

2.15 Distribution of material parameters based on the number of cycles the corresponding specimen underwent . . . 58
2.16 Evolution of creep strain and creep strain rate over one cycle for each one of the four types of cycled applied (black dashed lines), no damage is considered 60
2.17 Evolution of creep strain and creep strain rate over the first cycle for each one of the four types of strain range (black dashed lines), damage is considered 62
2.18 Comparison in the evolution of damage and applied strain profile over the first cycle for 0.02 strain range . . . 63
2.19 Evolution creep induced damage in the first cycle for the four different strain ranges applied . . . 64
2.20 Comparison of the hysteresis loop for different sets of identified material parameters . . . 65
2.21 Comparison of the damage evolution for different sets of identified material parameters . . . 65
2.22 Evolution creep strain cycles for the four strain ranges considered and for three cycles . . . 66
2.23 Evolution of the equivalent creep strain for the four strain ranges considered and for three cycles . . . 67
2.24 Hysteresis loop for the four strain ranges considered and for three cycles . . 68
2.25 Evolution of the effective elastic modulus over the strain controlled cycles . 69
2.26 Hysteresis loop evolution due to damage, only one cycle every twenty is represented for a total of 300, strain range 0.02 . . . 70
2.27 Evolution of damage over 300 cycles, strain range 0.02 . . . 70
2.28 Logic flowchart displaying the interaction between CREEP and USDFLD used-defined subroutines and Abaqus solver . . . 72
2.29 Comparison between Python numerical model and FE simulation with subroutines for the hysteresis loop . . . 73
2.30 Comparison between Python numerical model and FE simulation with subroutines for the damage . . . 74

3.1 Manual selection of stress-strain points on the 20th hysteresis loop, points in red . . . 76
3.2 Linear fit for the identification of the elastic modulus . . . 78
3.3 Comparison between acquired datapoints, elastic-creep model fitted respect to secondary creep strain rate and elastic-plastic-creep model fitted respect to datapoints . . . 79

4.1 Packaging structure and component together with ball grid array detail . . 82

4.2 Section of a BGA [104] 82
4.3 Crack development at the solder ball- PCB junction [41] 83
4.4 PCB structure form above, zoomed in 1/4 of the plate to highlight the expansion and contraction of the chip array 84
4.5 Ball pitch and body size representation for the global model, for (b) critical solder balls in red, one-eight of the board is actually simulated 85
4.6 Solder ball profile with associated dimensions 86
4.7 Global model form above with its symmetry planes (a) and with isometric view (b), submodeling solder ball highlighted 87
4.8 Two cycles of applied temperature profile for SAC305 88
4.9 Representation of the transfer of the displacement profile from the global model to the submodel 89
4.10 Volume of the solder ball where the average of computed quantities is carried out 90
4.11 Stress map for the S13 stress component along the diagonal direction of the packaging 91
4.12 Hysteresis loop evolution over forty simulated cycles 92
4.13 Damage evolution over forty simulated cycles 92
4.14 Hysteresis loop for the first cycle, different phases of the cycle highlighted . 93
4.15 Damage for the first cycle, different phases of the cycle highlighted 93
4.16 Evolution of the shear stress σ_{13} along the applied displacement profile . . 94
4.17 Damage level in the solder ball cross section after forty cycles 95

List of Tables

2.1 Bounds used for the optimization procedure of the parameters of the hyperbolic-sine creep law . . . 45
2.2 Bounds used for the optimization procedure of the parameters of the NORTON creep law . . . 45
2.3 Values of the initial guesses for hyperbolic-sine creep law . . . 46
2.4 Values of the initial guesses for NORTON law . . . 46
2.5 Results for the material constants for the hyperbolic-sine laws, data are computed with the use of Python and different libraries . . . 47
2.6 Results for the material constants for NORTON creep law, data computed with the use of `nlopt` library . . . 48
2.7 Results for the material constants for hyperbolic-sine creep law, double optimization is executed starting from undamaged specimens . . . 53
2.8 Values of the initial guesses for hyperbolic-sine creep law used in the line by line optimization for the boxplot . . . 54
2.9 Results for the material constants for the hyperbolic-sine laws, comparison of results between the original median and the filtered median . . . 57
2.10 Initial values of the elastic modulus [42] . . . 59
2.11 Values of the elastic modulus of SAC305 after a certain number of pre-damage cycles [42] . . . 68
2.12 Fitted parameter for the double exponential damage law . . . 69

3.1 Identified values of elastic modulus and yield stress from linear fit . . . 78
3.2 Results form the primary creep curve fit . . . 79

4.1 Dimensions for the ball pitch and the body size of the microchip . . . 85
4.2 Material properties for the solder ball, the PCB and the chip frame . . . 86

Listings

5.1 Implementation of CREEP and USDFLD Abaqus subroutines for 1D strain controlled test 111
5.2 Objective function implementation with overflow control for hyperbolic sine salculations 112

List of Symbols

Variable	Description	SI unit
T_{hom}	homologous temperature	-
$\boldsymbol{\sigma}$	stress tensor	MPa
$\boldsymbol{\varepsilon}$	strain tensor	-
$\boldsymbol{\varepsilon}_{\text{el}}$	elastic strain tensor	-
$\boldsymbol{\varepsilon}_{\text{pl}}$	plastic strain tensor	-
$\boldsymbol{\varepsilon}_{\text{cr}}$	creep strain tensor	-
$\boldsymbol{\varepsilon}_{\text{th}}$	thermal strain tensor	-
$\boldsymbol{C}$	stiffness tensor	MPa
α	thermal expansion coefficient	1/K
T	temperature	K
D	damage parameter	-
$\dot{\boldsymbol{\varepsilon}}_{\text{cr}}$	creep strain rate tensor	1/s
σ_{vM}	von Mieses equivalent stress	MPa
$\mathbf{S}$	deviatoric stress tensor	MPa
$\dot{\varepsilon}_{\text{cr}}^{\text{eq}}$	equivalent creep strain rate	1/s
$\mathbf{N}$	deviatoric tensor coaxial to stress deviator	-
R	universal gas constant	J/(K mol)
Q	activation energy	J/mol
ΔW_{tot}	energy density dissipated in mechanical cycle	MPa
ΔW	energy density dissipated at each cycle	MPa
T_m	melting temperature	K
r	normalized root mean square error	-
E	elastic modulus	MPa
E_0	initial elastic modulus	MPa
ε_{tot}	total strain	-
σ_{y}	yielding stress	MPa
H	hardening modulus	MPa
n	strain hardening exponent	-

Acknowledgements

I would like to express my sincere gratitude to the Technische Universität Berlin, where I had the privilege of completing this work as part of my Erasmus exchange. I am thankful for the resources, support, and welcoming environment provided by TU Berlin, which played a significative role in the successful completion of my research.

I am deeply grateful to my supervisors, Prof. Wolfgang H. Müller and Prof. Mauro Filippini, whose collaboration and support made all of this possible. I would also like to express my sincere gratitude to Dr. Aleksandr Morozov for his invaluable guidance and mentorship throughout this project.

A special thanks to all my friends, with whom I spent the past two years, both at university and beyond. You made this journey much lighter, and perhaps one day, we'll look back with nostalgia on those days spent studying together.

I am profoundly grateful to my family for their unwavering support, encouragement, and understanding throughout this journey. Your belief in me has been a constant source of strength, enabling me to reach accomplishments I might not have achieved otherwise. Thank you for always being there for me.